Theses and Dissertations   Theses and Dissertations

1-1-2015

Multichannel Analysis of Surface Waves Using Distributed Fiber Optic Sensors

Gustavo Galanomas

Follow this and additional works at: https://scholarsjunction.msstate.edu/td

Multichannel analysis of surface waves using distributed fiber optic sensors

By

Gustavo Galan-Comas

A Thesis
Submitted to the Faculty of
Mississippi State University
in Partial Fulfillment of the Requirements
for the Degree of Master of Science
in Civil Engineering
in the Department of Civil and Environmental Engineering

Mississippi State, Mississippi

December 2015

Multichannel analysis of surface waves using distributed fiber optic sensors

By

Gustavo Galan-Comas

Approved:

_____
Thomas D. White
(Major Professor)

_____
Richard Daniel Costley, Jr.
(Committee Member)

_____
Philip M. Gullet
(Committee Member)

_____
James L. Martin
(Graduate Coordinator)

_____
Jason Keith
Dean
Bagley College of Engineering

Name: Gustavo Galan-Comas

Date of Degree: December 11, 2015

Institution: Mississippi State University

Major Field: Civil Engineering

Major Professor: Thomas D. White

Title of Study: Multichannel analysis of surface waves using distributed fiber optic sensors

Pages in Study: 164

Candidate for Degree of Master of Science

The Multichannel Analysis of Surface Waves (MASW) method traditionally uses an array of collinear vertical geophones to measure seismic wave propagation velocity at discrete points along the ground surface. Distributed fiber optic sensors (FOS) measure the average longitudinal strain over discrete lengths (i.e., zones) of a buried fiber optic cable. Such strain measurements can be used to assess ground motion and thus analyzed with the MASW method. To evaluate the feasibility of using FOS strain measurements in the MASW method, field experiments were conducted with both FOS and surface vertical geophones. Synthetic seismograms were also used to compare FOS to vertical and horizontal geophones and investigate the effect of installation depth and sensor type. Through the MASW method, shear wave (V_s) profiles from the FOS showed comparable results to those obtained with the geophones and achieved the same degree of uncertainty from the non-uniqueness of the MASW inversion process.

DEDICATION

This thesis could not have been completed without the support and exemplary lifelong guidance of my family.

I am very fortunate to have my dear wife, Marian. Her endless patience and unconditional support allowed me to stay motivated and complete this thesis.

I am forever grateful for my parents, Benjamin and Sonia. Their continuous support and lifelong example led me to who I am today.

I also wanted to give a special dedication to my grandfather, Benny, who passed away this year. I will forever remember him as a loving, humorous, kind, and energetic person. Thanks for being one of my greatest role models and showing me that you can do anything you set your mind to.

ACKNOWLEDGEMENTS

I would like to thank Dr. Richard D. Costley for introducing me to distributed fiber optic sensing and helping me through some of the tough technical aspects of this research. I am also thankful for the help of Dr. Thomas D. White for his great feedback and help guiding this work into a thesis, Mr. Isaac Stephens for his help with the Seismic Cone Penetrometer Test (SCPT) for ground truth verification, and Mr. Eric Smith for his assistance in the MASW field data collection. I am also grateful for the advice received from colleagues and friends that helped me to stay motivated throughout this research.

TABLE OF CONTENTS

LIST OF TABLES

LIST OF FIGURES

CHAPTER I

INTRODUCTION

The direct relationship between shear wave velocity (V_S) and the soil's shear
modulus can be used for characterization of stress-strain soil behavior in the linear elastic
regime. Determining the V_S variation with depth, referred to as a shear wave velocity
profile, could then be used to investigate changing stiffness conditions with depth. Shear
wave velocity profiling can be applied for earthquake ground response analysis,
estimating potential of liquefaction, advanced three dimensional characterization of a site,
construction quality control, and detection of subsurface anomalies (Nazarian, 2012). In
addition to these applications, the interest for V_S profiling has expanded in recent years
since the requirement of the average V_S of the upper 30 meters (V_{S30}) for use in seismic
site classification adopted by the National Earthquake Hazards Reduction Program
(Building Seismic Safety Council, 2003) and the ASCE/SEI 41-06 (Nazarian, 2012; Wair
et al., 2012).

Over the past two decades, application of Multichannel Analysis of Surface
Waves (MASW) has emerged as a reliable, flexible, and affordable tool for estimating V_S
profiles for use in geotechnical site characterization (Penumadu & Park, 2005; Williams
& Pnemadu, 2011). When MASW analysis is used over multiple in-line seismic surveys,
a 2-D V_S profile can be estimated to detect the existence of subsurface anomalies by
means of V_S variations with depth (Xia et al., 2000; Miller et al., 2004). Performing this

1

analysis over time to monitor changes in V_S can be used to find developing detrimental subsurface conditions (Miller & Ivanov, 2005). Prospective applications include monitoring seasonal seepage conditions in levees and earthen dams, internal erosion on hydraulic structures, and construction and maintenance of roadbeds and levees. Evaluating these particular applications go beyond the scope and intent of the current research, but illustrate the need of using a robust cost effective permanent sensor that can be easily installed over large distances (i.e., more than 10 km).

1.1   Problem Statement

Traditional MASW seismic surveys make use of an array of twelve or more collinear vertical geophones to measure seismic wave propagation velocity at the surface. Geophones are highly adaptable temporary receivers for MASW surveys; however, due to the extensive setup and equipment required, they are costly and maintenance intensive when employed in permanent long distance arrays.

By using buried fiber optic cable, distributed fiber optic sensor (FOS) systems offer desirable qualities to create permanent linear sensors over distances that can reach tens of kilometers in distance. These sensors measure the average longitudinal strain over discrete lengths (i.e., zones) of the buried fiber optic cable, which can be used to assess ground motion. In addition to its sensing capabilities, the optical fiber comprising the FOS serves as a transmission medium. As a result, strain locations can be determined along the cable length. Due to its simplified setup, the FOS requires less equipment; and therefore, less maintenance, making the installation more cost efficient to implement over long distances.

Employing MASW in conjunction with permanently installed fiber optic sensors offers the potential to monitor areas susceptible to change without the added expense of: (1) deploying geophones each time a test is performed or (2) involving complicating test layouts and setups. The use of FOS is a promising technology. However, results of MASW analysis using data from both FOS and geophones need to be compared due to the differences in measurements, sensitivity, and installation of the two technologies.

1.2   Objective

The objective of this study is to evaluate the feasibility of using a buried FOS with the MASW method to obtain a 1-D V_S profile.

1.3   Approach

Data from distributed FOS and geophones was obtained using field experiments and synthetic (modeled) seismograms and then analyzed with MASW method. This allowed comparison of FOS to conventional geophones typically employed in MASW seismic surveys.

Field experiments were conducted to simultaneously record data from both buried FOS at depths of 0.5 m and 1.0 m and vertical geophones at the surface. Data collected was analyzed with the MASW method, and 1-D V_S profiles were obtained for the different sensors. In addition, a Seismic Cone Penetrometer Test (SCPT) was performed. The SCPT provided a direct 1-D V_S profiles that served for ground truth verification of the data.

Synthetic seismograms from a 2-D axisymmetric finite element (FE) analysis were used to further explore the effects of installation depth and sensor orientation. The

FE model simulated a MASW seismic survey of an idealized multi-layer soil model of the test site used in the field experiments. Synthetic seismograms were obtained for simulated FOS, vertical geophones, and horizontal geophones. Each of these sensors was investigated at depths of 0.0 m (i.e., at the ground surface), 0.5 m, and 1.0 m. These seismograms were processed and analyzed in the same manner as the field experiments seismograms. Results were verified against the FE input V_S profile.

Comparisons were made between the MASW V_S profile results (i.e., using FOS and geophones) and the expected V_S profiles (i.e., SCPT V_S profile for the field experiments and FE input V_S profile for synthetic seismograms). The root mean square error (RMSE) of the V_S for the different sensors was used to evaluate the adequacy of using FOS for MASW surveys.

4

CHAPTER II

LITERATURE REVIEW

2.1   Surface (Rayleigh) Waves

This section presents a review of seismic surface waves that form the basis of development of the MASW analysis method. Given the purpose of this study, some of the fundamental characteristics are worth discussing in order to understand its effect on buried distributed fiber optic sensors.

2.1.1   Wave Propagation in an Infinite Medium

When a seismic disturbance acts on a solid medium it generates a stress wave field, whose energy propagates away from the disturbance location (Stokoe & Santamarina, 2000). The stress waves get transferred from one portion of the solid medium to another in a distinguishable propagation velocity pattern (Foti et al., 2015), referred to as wave propagation. In geologic materials, wave propagation is described by treating geologic media as continuous (Kramer, 1996). This is achieved by using the general small strain assumption that is approximated with linear elastic relationships (Foti et al., 2015).

Equations of motion of waves traveling through an infinite, homogeneous, isotropic, linear elastic medium form the basis of wave propagation (Richart et al., 1970; Kramer, 1996). These equations are manipulated to reveal two solutions describing waves propagating through the mass or body of an infinite medium, referred to as body

5

waves. The first type of body wave is known as the P-wave or primary wave (also referred to as compressional or longitudinal wave), since they are the first to arrive in seismic records (i.e., seismograms). The P-wave wave describes particle motion occurring parallel to the direction of wave propagation through compression and dilation causing changes in volume without shear or rotation, as shown in Figure 2.1.
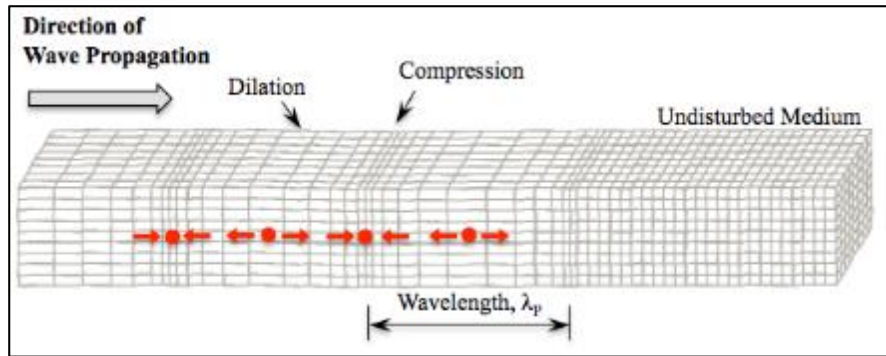
Figure 2.1   P-wave particle motions generated from body waves in an infinite, homogeneous, isotropic, linear elastic medium.

(Modified from Kramer, 1996)

The P-wave's propagation through a medium can be described through its velocity, V_P, using the linear elastic relationship:

$$V_P = \sqrt{\frac{\lambda + 2G}{\rho}} = \sqrt{\frac{M}{\rho}},$$

(2.1)

where λ and G are Lamé's constants and ρ is the material mass density. Linear elastic relationships can be used to simplify the Lamé's constants into the longitudinal modulus, or P-wave modulus, M.

A second type of body wave occurs referred to as the S-wave or secondary wave (also known as shear or distortional waves). These are the second wave to arrive on a seismogram. The particle motion occurs on a perpendicular plane to the wave propagation direction. Since S-waves act on a perpendicular plane these are often divided into two perpendicular components. Particle motion moving in a horizontal plane referred to as SH-waves and particle motion acting on a vertical plane referred to as SV-waves. A vector sum of its SH and SV components can be used to represent an arbitrary particle motion of an S-wave. Figure 2.2 shows idealization of an SV-wave moving in a vertical plane.
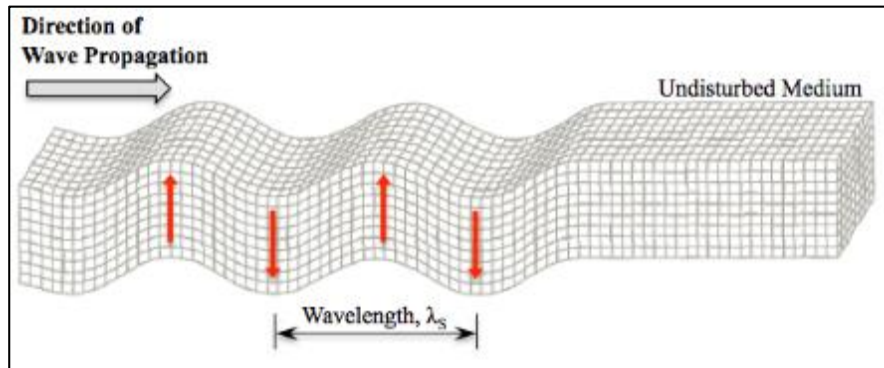
Figure 2.2   SV component of an S-wave particle motion generated from body waves in an infinite, homogeneous, isotropic, linear elastic medium.

(Modified from Kramer, 1996)

The S-wave can be described with the shear wave velocity, V_S, using the linear elastic relationship:

$$V_S = \sqrt{\frac{G}{\rho}} \, .$$

(2.2)

7

For a homogeneous, isotropic, elastic medium, the P-wave and S-wave velocities are

related through the Poisson's ratio, v, by:

$$\frac{V_P}{V_S} = \sqrt{\frac{1-v}{0.5-v}}.$$

(2.3)

The body wave propagation velocities are directly related to the medium's

stiffness though its relationships to longitudinal modulus and shear modulus as observed

in Equations (2.1) and (2.2). If body wave velocities are determined experimentally, these

relationships show that linear elastic constants can be determined for use in material

characterization (Foti et al., 2015).

2.1.2   Idealized Plane Waves in Semi-Infinite Media

The idealization of an infinite medium (discussed in section 2.1) is not

appropriate for near surface geotechnical characterization since the geologic medium

consists of an upper stress-free surface affecting the stress wave propagation. A semi-

infinite body, also referred to as a half-space, is frequently used to model wave

propagation near the surface as concerned in this study. It is possible for P- and S-waves

to propagate in a semi-infinite medium, however, other types of waves develop due to the

stress free boundary on the half-space surface. These waves are referred to as surface

waves. Although different types of surface waves develop under specific conditions, for

the purpose of this study only Rayleigh waves will be considered.

2.1.2.1   Rayleigh Waves in a Homogeneous Half-Space

The existence of Rayleigh waves was first introduced by Lord Rayleigh (1885)

and later explained in greater detail by Lamb (1904). A plane-wave traveling through a

homogeneous half-space, as shown in Figure 2.3, was used to describe the Rayleigh wave propagation.
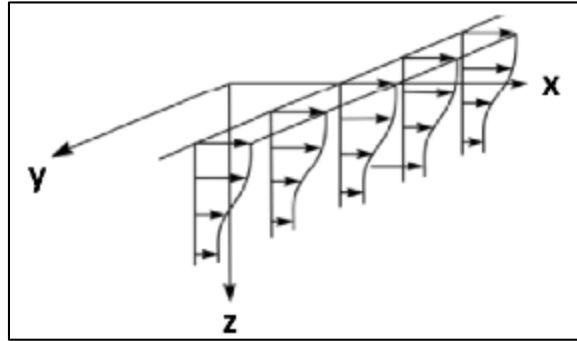
Figure 2.3   Plane-wave propagating in the x-direction.
(From Kramer, 1996)

The idealization of a plane-wave with an imposed zero stress boundary condition at the surface constrained particle motion to one plane. This allowed particle motion to be resolved into horizontal and vertical displacement components with varying amplitude with depth. The generalized variation of the displacement components as a function of depth is shown in Figure 2.4. This generalization is achieved normalizing the displacement components amplitudes by their respective amplitudes at the surface (i.e., at $z = 0$) and normalizing depths by the R-wave wavelength.
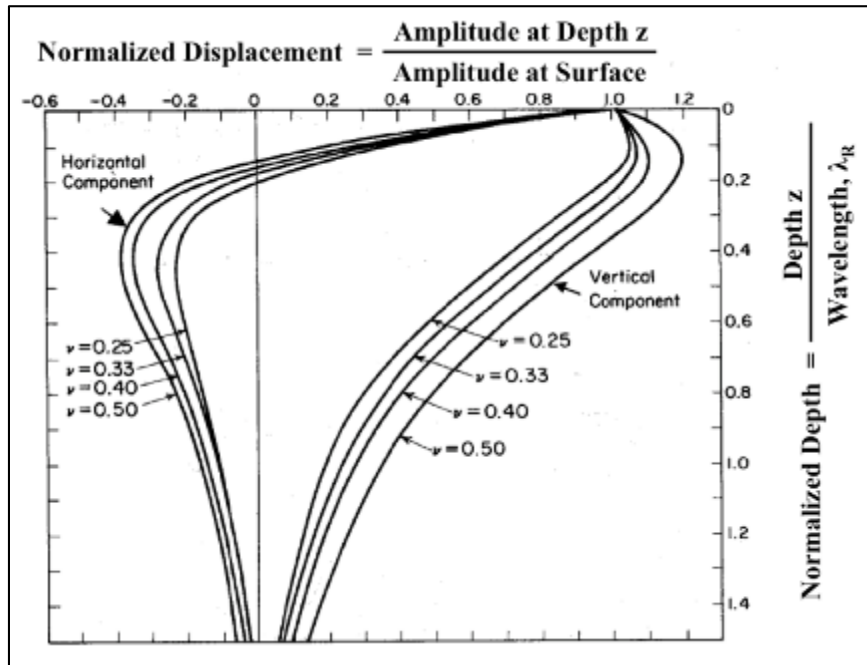
Figure 2.4   Generalized variation of Rayleigh wave displacement components with
depth.

Showing normalized displacement as a function of normalized depth. (After Richart
et al., 1970)

In a homogeneous elastic half-space, the particle motion decays exponentially

with depth as observed in Figure 2.4. The respective decay on the displacement

component amplitudes is projected into the particle motion trajectory. The ratio of

vertical to horizontal surface amplitudes for different Poisson's ratio is shown in

Figure 2.5. Since the ratio is always greater than one, it shows that, at the surface, the

vertical component is always greater than the horizontal component. This characterizes

the elliptical motion behavior that combines the vertical and horizontal displacement

results at the surface of the half-space.
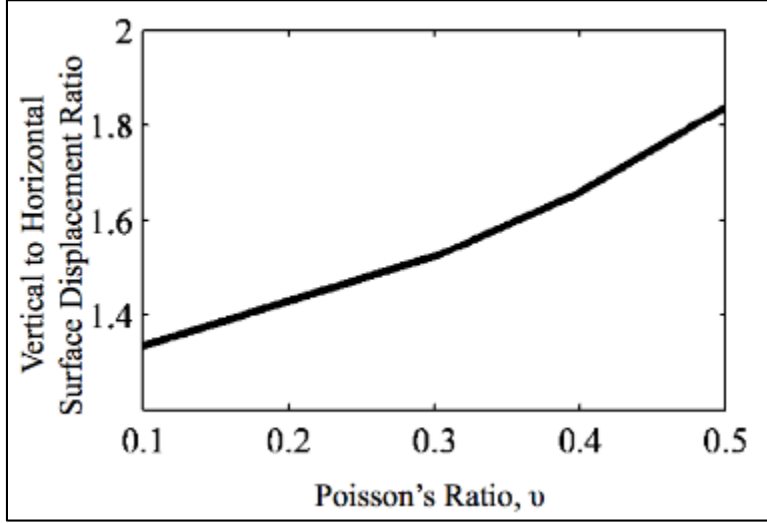
Figure 2.5   Vertical to horizontal surface displacement ratio as a function of Poisson's ratio.

(From Lin, 2014)

As previously shown in Figure 2.4, the displacement components change with depth. Near the surface, both the vertical and horizontal components are positive, and these combine to create a retrograde motion trajectory (describing a particle moving counter-clockwise to a wave propagating in the right hand direction). At a critical depth, $Z_{critical}$, the horizontal displacement goes to zero and becomes negative. This is often approximated to occur at a normalized 20% of the Rayleigh wavelength, i.e., 0.2λ (Lin, 2014). However, the critical depth can also be defined by (Foti et al., 2015):

$$Z_{critical} = \frac{\left(\ln\left(1 - \frac{V_R^2}{2V_S^2}\right)\right)}{\omega_R\left(\sqrt{\frac{1}{V_R^2} - \frac{1}{V_S^2}} - \sqrt{\frac{1}{V_R^2} - \frac{1}{V_P^2}}\right)}, \tag{2.4}$$

where ω_R is the R-wave cyclic frequency (i.e., $2\pi f_R$) and V_P, V_S, and V_R are the P-, S-, and R-wave velocities, respectively. At this depth, the motion becomes purely vertical. At greater depths, the motion turns into a prograde motion trajectory (describing a particle

11

moving clockwise to wave propagation in the right hand direction). The trajectories of these motions are shown in Figure 2.6.
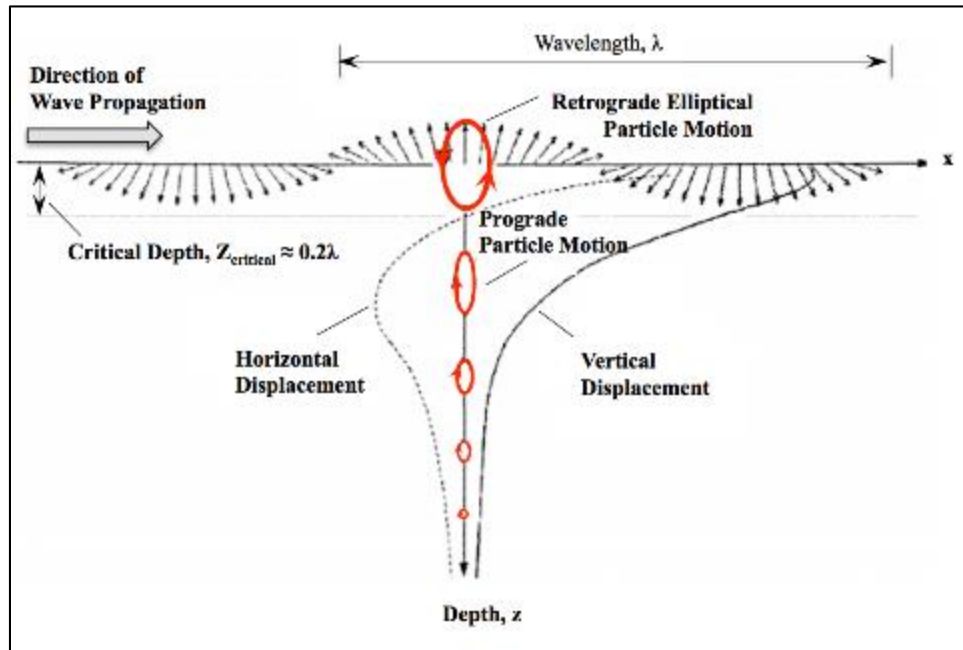
Figure 2.6   Particle motion trajectories with depth of a Rayleigh wave in a homogeneous elastic half-space.

(Modified from Foti et al., 2015)

Generally, seismic disturbances propagating along a ground surface contain contributions from both Rayleigh waves and body waves. Lamb (1904) obtained the solution for the displacement field produced by a transient point load on a homogeneous half-space. Corresponding motions were recorded as a time history, shown in Figure 2.7. The particle motion associated with different wave types arrive at a given location based on their propagation velocities.
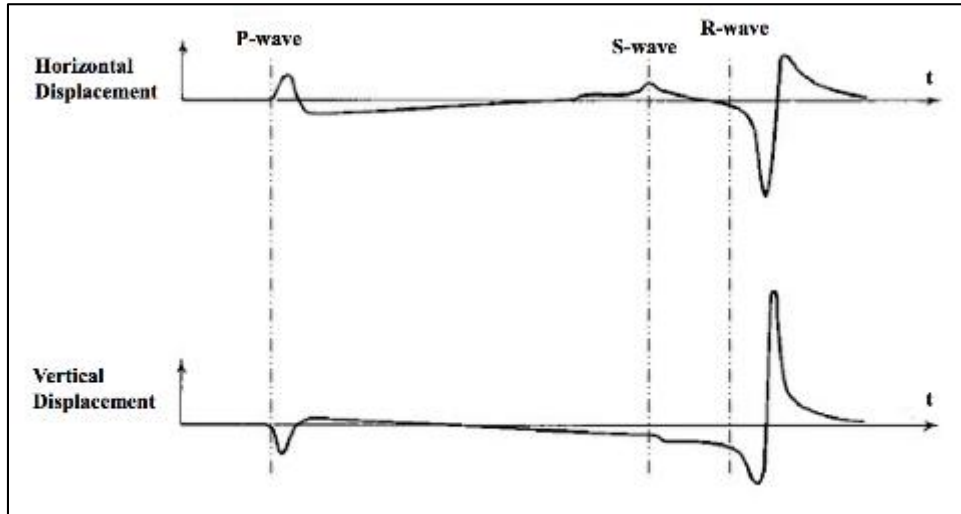
Figure 2.7   Time history of particle motion at a distant surface location from a point
              source acting on an elastic half-space.

(After Lamb, 1904)

Differences in relative displacements amplitudes are accounted by the partition of

the total energy of a seismic disturbance into the different wave types. For the case of a

vertical oscillating circular foundation, the partition of energy between different wave

types is displayed in Figure 2.8. Rayleigh waves (R-waves) account for two thirds of the

total transmitted seismic energy and attenuate slower than body waves for a seismic

source at the surface (Richart et al., 1970). For that reason, the arrival of R-wave particle

motion results in larger displacements, as observed in Figure 2.7.
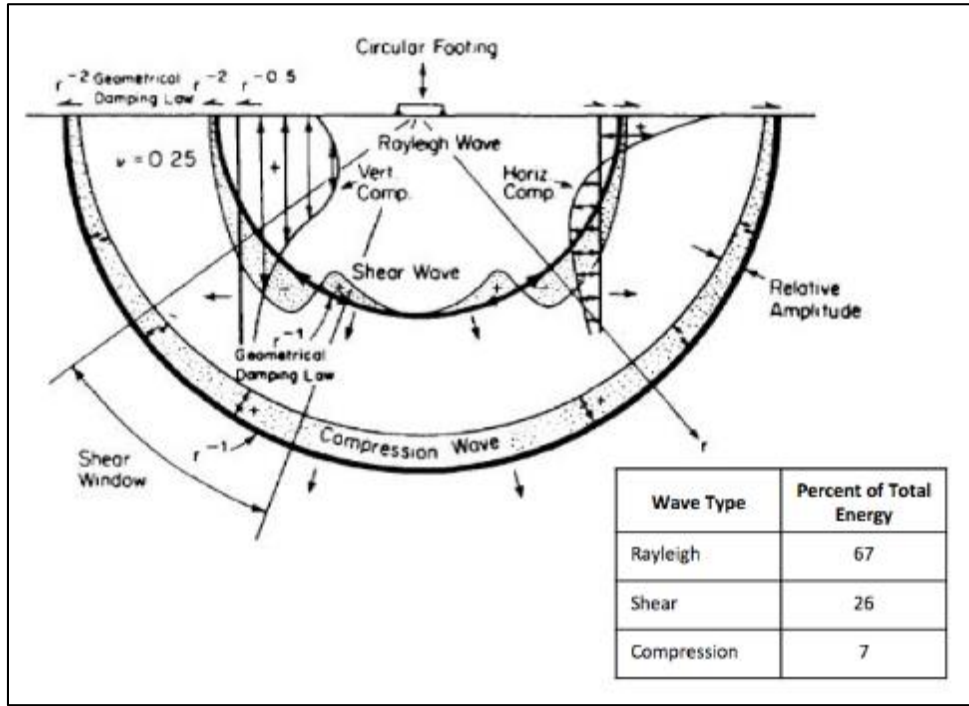
Figure 2.8   Wave motion on a homogeneous, isotropic, linear elastic half-space caused by vertical oscillations of a circular footing.

(From Richart et al., 1970)

2.1.2.2   Rayleigh Wave Velocity in a Homogeneous Half-Space

The R-wave velocity, V_R, can be determined through relationship interactions of P-wave and S-wave. The ratios between R-wave and P- and S-wave velocities can be used to show how these velocities are interrelated for varying Poisson's ratio. Figure 2.9 shows the generalized variation of wave velocities as a function of Poisson's Ratio. This generalization is achieved normalizing the corresponding wave velocities by the shear wave velocity.
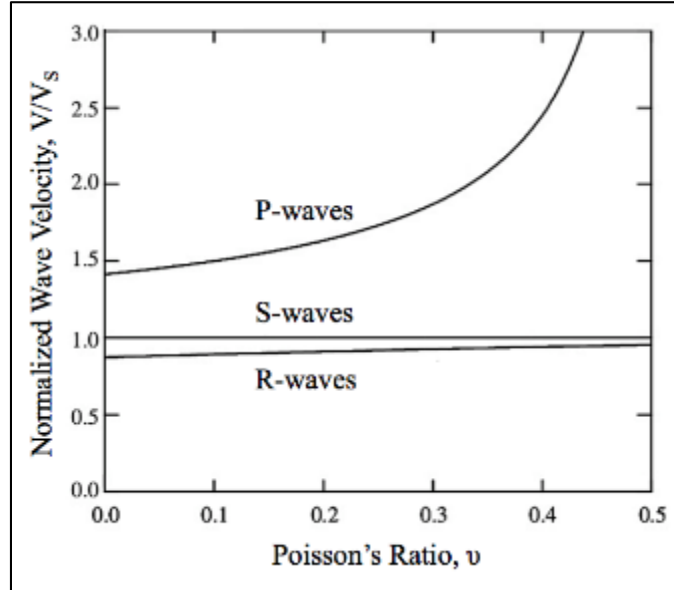
Figure 2.9   Generalized relationship between wave velocities and Poisson's ratio on a
uniform elastic half-space.

 (After Richart et al., 1970)

Using the normalized wave velocities, the variation of V_R in terms of V_S and

Poisson's Ratio can be approximated as (Stokoe & Santamarina, 2000):

$$V_R = \frac{0.874+1.117\upsilon}{1+\upsilon}V_S .$$ (2.5)

This approximation reflects the range of V_R/V_S being between 0.874 and 0.955 for

Poisson's ratio values ranging from 0.0 to 0.5, as shown in Figure 2.9. In a homogeneous

half-space, body wave velocities are constant with depth and V_R are related to these

velocities by only Poisson's ratio, thus resulting in a constant V_R value with depth

(Richart et al., 1970).

2.1.2.3   Rayleigh Waves Dispersive Nature in Vertical Heterogeneous Half-Space

The fundamental behavior of Rayleigh waves propagating in a homogeneous half-

space was described in the previous section. Using this assumption, Rayleigh waves are

15

related to body waves only by Poisson's ratio and have no dependency on frequency (Richart et al., 1970). As previously mentioned, R-wave velocity will thus be constant with depth, as shown in Figure 2.10(a). Due to its independence with frequency, R-waves in a homogeneous body are referred to as non-dispersive (Richart et al., 1970).
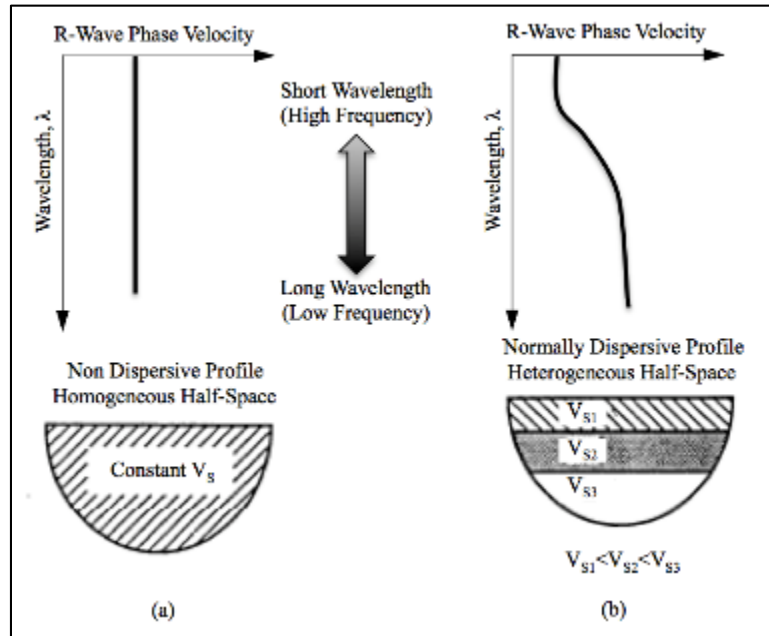
Figure 2.10   Dispersion phenomenon of Rayleigh wave velocity due to material
               heterogeneity.

(After Rix et al., 1991)

Dispersion describes the phenomenon in which the propagation of wave velocities is frequency (and wavelength) dependent. In many near-surface applications and as studied herein, material is heterogeneous and stiffness usually increases with depth (Foti et al., 2015). Since the depth of Rayleigh wave motion depends on the wavelength, as shown in Figure 2.4, varying material stiffness with depth generates Rayleigh waves of different wavelengths. Faster R-wave velocities are observed for waves of lower

frequencies, while slower R-wave velocities are seen for higher frequency waves; this effect is called geometrical dispersion (Foti et al., 2015). These wavelengths then alter the propagation velocity observed at or near the surface. The geometrical dispersive behavior for increasing stiffness profiles, shown in Figure 2.10(b), is referred to as a normally dispersive. Sites with stiffness decreasing with depth also exist, referred to as inversely dispersive, however, these will not be discussed.

Figure 2.11 shows two layers overlying a half-space (which can be inferred to be bedrock extending to infinity). High frequency (i.e., short wavelength) particle motion is mostly controlled by the material properties of Layer 1, since the wavelength does not penetrate further than the depth of Layer 1. Low frequency (i.e., long wavelength) motion reaches greater depth and particle motion is significantly concentrated in the upper two layers. Therefore, the low-frequency Rayleigh wave velocity will be controlled by a proportional combination of the two layer's material properties individually affecting the particle motion. Velocities in the lower frequency range (i.e., longer wavelength) penetrate into deeper, stiffer layers resulting in higher phase velocities. Since higher phase velocities exist for lower frequencies, low frequency Rayleigh waves will arrive before high frequency R-waves.
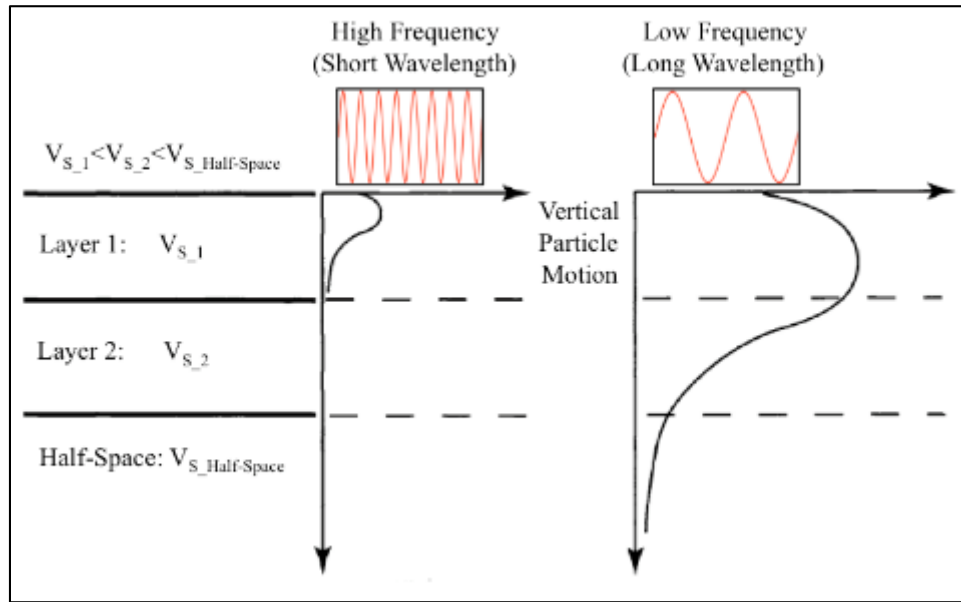
Figure 2.11 Geometrical dispersion of Rayleigh in heterogeneous materials. (After Foti et al., 2015)

Rayleigh wave dispersion caused by changes in material stiffness in vertically heterogeneous media could consequently be used to assess the subsurface material stiffness properties (e.g., estimating shear wave velocity). Data needs to be collected over a broad range of frequencies to obtain a corresponding change of velocities, resulting in a characteristic dispersion curve for a site.

The fundamental mode (M0) is associated with the displacement pattern of R-waves propagating in a homogeneous half-space, as shown in Figures 2.4 and 2.6. However, R-waves can propagate with different modes in vertically heterogeneous media. Each mode is associated with its respective displacement pattern. Different modes can occur simultaneously, and such effect is shown in the solid curves on Figure 2.12. As a result, multiple wavelengths, and consequently different phase velocities can coexist at given frequencies (Strobbia, 2003).

18
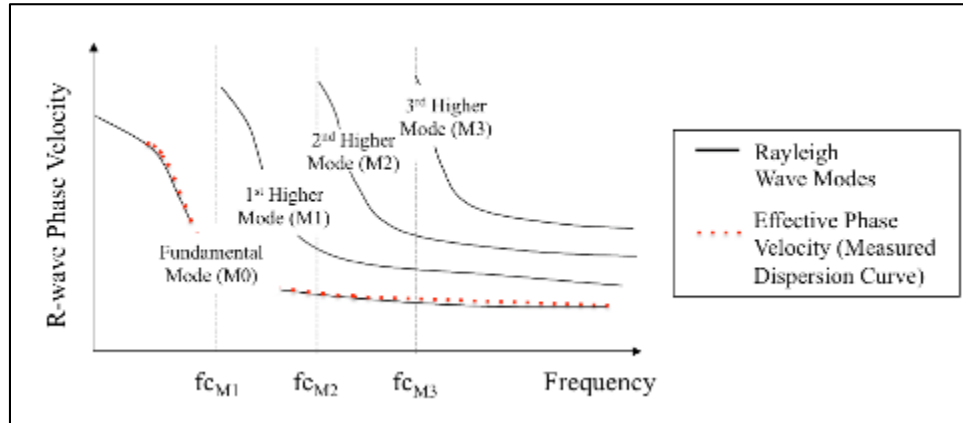
Figure 2.12   Multiple Rayleigh wave modes and cut-off frequencies for higher modes.
Also shown are the acquired (effective) phase velocities coinciding with the phase
velocities of the fundamental mode M0. (Adapted from Strobbia, 2003)

The associated energy for each mode depends on the subsurface properties and

the type of seismic source (Strobbia, 2003). Lower frequency limits, also known as cut-

off frequencies, specify where each respective higher mode can exist. The frequencies

fc_{M1}, fc_{M2}, and fc_{M3} in Figure 2.12 show the cut-off frequencies associated with the first

three higher modes respectively. Below the cut-off frequency of the first higher mode

(M1), only the fundamental mode (M0) is present. The fundamental mode does not have

a cut off frequency. Fundamental modes predominate wide frequency ranges when the V_S

profile increases gradually with depth, as commonly found in geotechnical field

investigations (Foti et al., 2015). An example of a fundamental mode (M0) dispersion

curve for a site with vertically increasing material stiffness is shown in the dotted curve

on Figure 2.12. The M0 dispersion curve can then be related to geotechnical subsurface

properties, through the solution of the inversion problem (as discussed in the next

section), to estimate a shear wave velocity profile.

19

2.2   Shear Wave Velocity (V$_S$) Profiling and Surface Wave Methods

Due to the direct relationship between S-wave propagation velocity and the soil's shear modulus (shown in Equation (2.2)), V$_S$ is typically used for characterization of stress-strain soil behavior. The V$_S$ variation with depth is referred to as a shear wave velocity profile.

Shear wave velocity profiling can be used for earthquake ground response analysis, estimating potential of liquefaction, advanced three dimensional characterization of a site, construction quality control, and detection of subsurface anomalies (Nazarian, 2012). In addition to these applications, the interest for V$_S$ profiling has expanded in recent years since the requirement of the average V$_S$ of the upper 30 m (V$_{S30}$) for use in seismic site classification adopted by the National Earthquake Hazards Reduction Program (Building Seismic Safety Council, 2003) and the ASCE/SEI 41-06 (Nazarian, 2012; Wair et al., 2012). Due to these uses and necessary characterization of soils, V$_S$ profiling is essential in geotechnical engineering.

There are different in situ techniques that can be used to estimate the profile of shear wave velocities with depth. These are categorized as invasive and non-invasive tests.

2.2.1   Invasive In Situ Techniques for V$_S$ Profiling

Invasive tests involve conventional borehole techniques, such as the Standard Penetration Test (SPT) and the Cone Penetration Test (CPT), which are typically used in standard geotechnical field investigations. These methods are mainly intended to measure the resistance to penetration of geologic material with depth; however, a significant number of published dataset regression correlations are available to estimate the shear

wave velocity with penetration resistance values (Wair et al., 2012). Other invasive

techniques include geophysical methods such as cross-hole logging, suspension logging,

and down-hole logging. The Seismic Cone Penetration Test (SCPT), which is a CPT used

in conjunction with down-hole measurements, has become more commonly used for V_S

profiling due to the method's cost effectiveness and relatively fast ability to acquire data

compared to other invasive methods (Wair et al., 2012). For this reason the SCPT was

used for ground truth comparison during the field experiments in this study. A schematic

representation of these methods is shown on Figure 2.13. Although invasive tests are

considered to be reliable for this V_S estimation, they tend to be relatively expensive (e.g.,

due to required equipment, personnel, logistics, access, etc.) and time-consuming (e.g.,

drilling, backfilling, etc.).
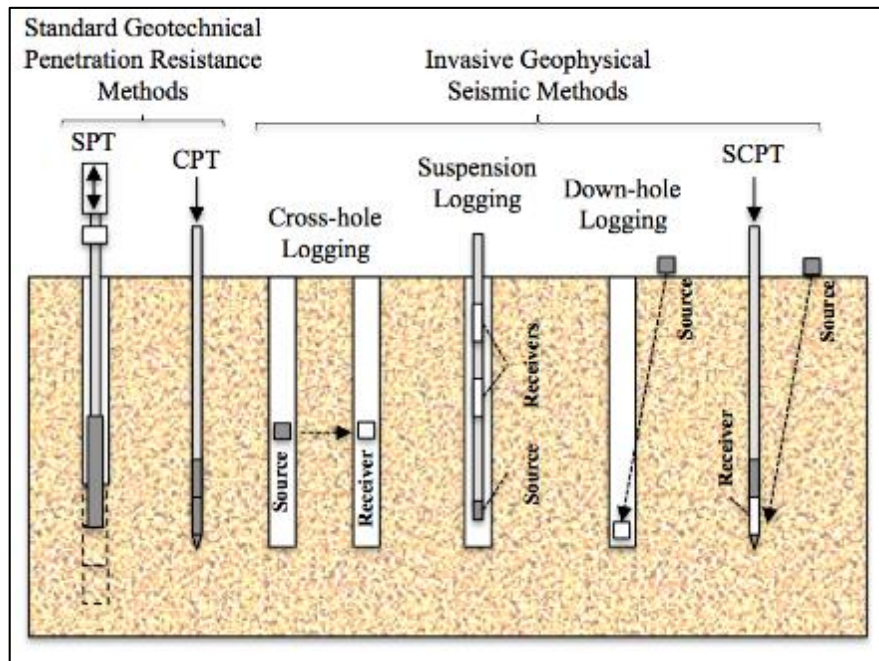
Figure 2.13   Invasive test methods.

(Adapted from Mayne, 2012)

2.2.2   Non-Invasive In Situ Techniques for V_S Profiling

Tests conducted at the ground surface are known as non-invasive tests, since they do not "invade" the soil generating significant soil disturbance. Since no direct physical measurements are made, these methods have a greater degree of uncertainty than invasive tests (Foti et al., 2015). These methods, however, are generally more affordable (e.g., less equipment), more adaptable (e.g., making it very convenient to implement in highly urban settings), more practical to cover areas of large extent, and cause less environmental impact (e.g., equipment is placed temporarily).

Non-invasive tests include: seismic reflection, seismic refraction, and surface wave methods. In general, these methods are performed by recording the response from an active known seismic source acting on the surface with discretely placed surface receivers (also referred to as a channels). In most common applications, these methods use multiple receivers placed in a linear array. The response captured at such receivers with time is known as a seismogram or seismic record. The seismic record consists of the time history response of each receiver location. A representation of the target seismic paths of such methods is shown in Figure 2.14. Representation of target response paths can be observed on a seismogram, as shown on Figure 2.15.
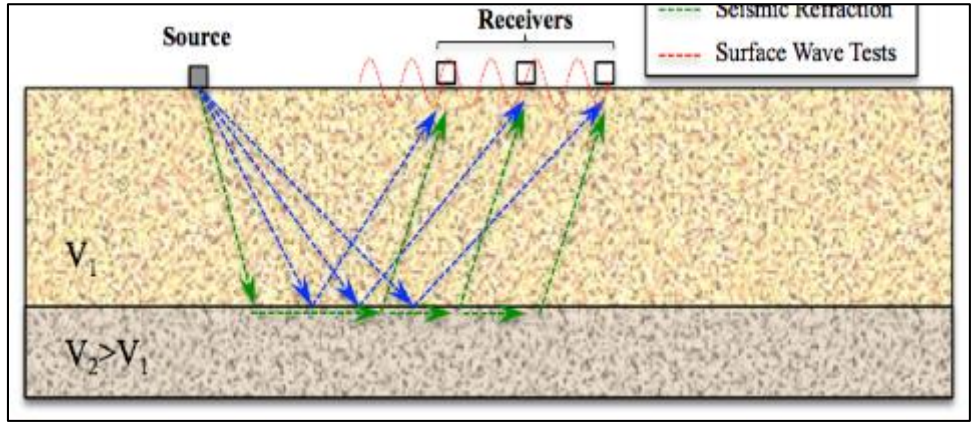
Figure 2.14   Target seismic paths to be measured in non-invasive geophysical seismic
                    methods.

(Adapted from Nazarian and Stokoe, 1983)
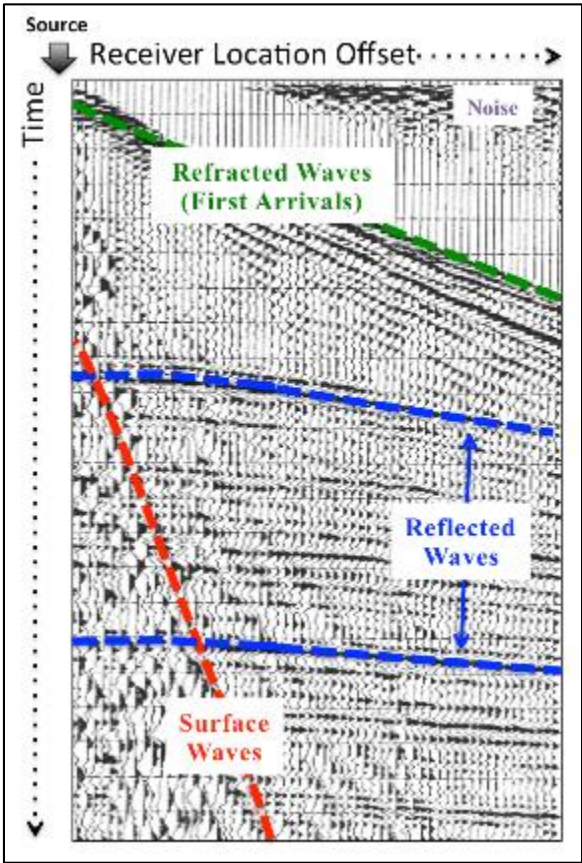
Figure 2.15   Representative target wave responses observed on a seismogram.

(Adapted from Park, 2005)

Seismic reflection and seismic refraction methods have been mostly dedicated to deep investigations providing a coarse global average of soil conditions. P-waves served as the basis for the early development of the seismic reflection and seismic refraction methods, however, S-waves are currently considered as well. Estimation of S-wave velocity with these methods, however, can be challenging since the amount of energy that is transmitted as a horizontally polarized shear waves makes it difficult to estimate the S-wave time of arrivals (Foti et al., 2015). The need to adequately estimate S-wave velocities and ensure high signal-to noise ratio for the FOS proposed in this study led to disregard these methods.

Surface wave methods exploit surface waves generated by a seismic source, which were regarded as noise in seismic reflection and seismic refraction methods (Park et al., 1999). This is justified by the fact that Rayleigh waves (R-waves) account for two thirds of the total transmitted seismic energy for a seismic source at the surface, as shown in Figure 2.8. The higher energy carried by the R-waves compared to the body waves, results in higher amplitudes, making it easier to detect these waves at the ground surface receivers.

The basis of these methods relies on the dispersion of Rayleigh waves in vertically heterogeneous materials, as discussed in section 2.1.2.3, which is characterized by the dependence of the R-wave velocity with frequency. This dependent relationship is shown as a dispersion curve, which is obtained from the field data using a variety of signal processing techniques. Through the solution of the inversion problem, the dispersion curve is then used to relate to geotechnical subsurface properties and determine a shear wave velocity profile. The surface wave method procedure is

summarized in Figure 2.16. Different surface wave methods have been developed over the years. An overview of these methods is presented in the following subsections.
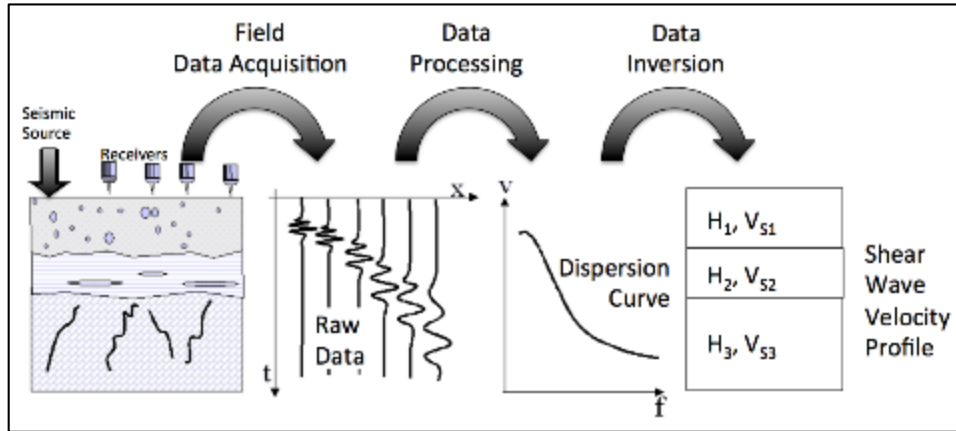
Figure 2.16   Typical procedure for surface wave methods.
(From Strobbia, 2003)

2.2.2.1   Steady-State Rayleigh Method (SSRM)

The first surface wave applications to engineering go back to the 1950s (Foti et al., 2015) and is known as the Steady-State Rayleigh Method (SSRM). The SSRM was proposed by Jones (1958, 1962) in the United Kingdom and was later adopted in the United States by (Ballard, 1964) at the Waterway Experiment Station, Vicksburg, MS. The SSRM was initially performed to determine the thickness and deformation of concrete slabs. It was later adapted to soil exploration when it was noted that velocity was a function of frequency for vertically heterogeneous sites (Foti et al., 2015).

This method involves using a steady-state vertical mechanical vibrator to generate a continuous Rayleigh wave of specified frequency, f. Dispersion is obtained by moving a vertical receiver collinearly away from the source. Receiver to source distances are

25

recorded where receiver response is in-phase with the mechanical vibrator. Distances

between in-phase locations represent a wavelength, λ_R. Figure 2.17 shows a schematic of

the SSRM procedure.
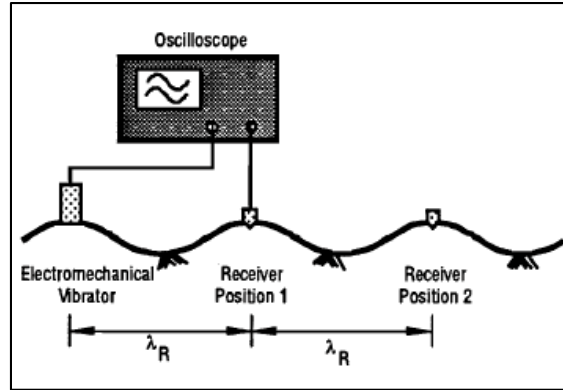
Figure 2.17   Experimental setup and procedure of the Steady-State Rayleigh Method.
(After Richart et al., 1970)

Since frequency input is known, the phase velocity (assumed to be equal to the

Rayleigh wave velocity, V_R) can be determined as:

$$V_{phase} = V_R = f * \lambda_R. \tag{2.6}$$

The procedure is repeated for different frequency inputs to generate a complete

dispersion curve. This is a very time consuming procedure due to the large number of

points required to define a dispersion curve and the time it takes to test each frequency

(Rix et al., 1991). Several in-phase source offsets can be used to obtain an average

wavelength, and thus a better estimate of phase velocity, as shown in Figure 2.18(a).

Changing the frequency and repeating these steps, it is possible to obtain the

characteristic dispersion curve (i.e., V_R vs. f) of the site, as shown in Figure 2.18(b).

26
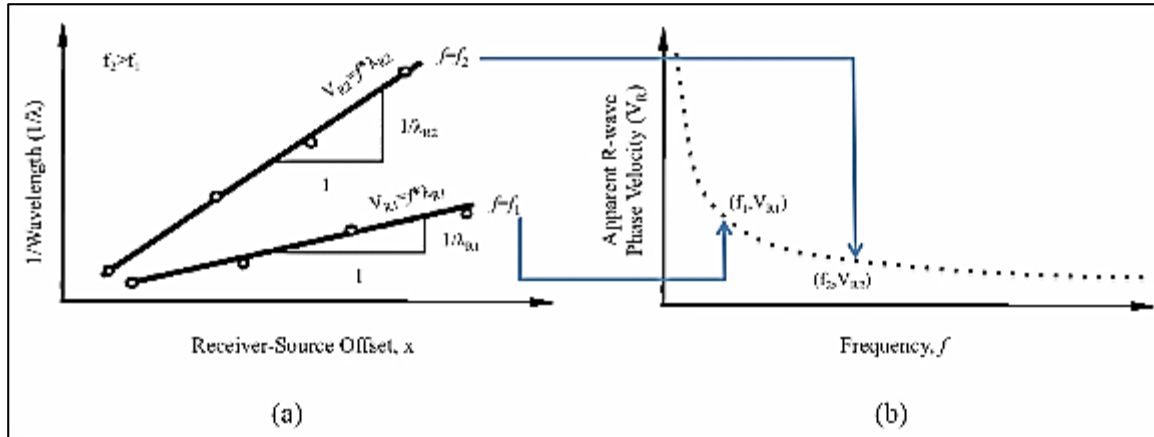
Figure 2.18   Steady-State Rayleigh Method dispersion curve procedure.

Showing (a) Average wavelength determination, and (b) resulting dispersion curve determination from tested frequencies. (Modified after Rix et al., 1991)

A straightforward empirically based inversion procedure was designed due the limited computational ability when the SSRM method was proposed during the 1950s and 1960s (Rix et al., 1991; Foti, 2000). The shear wave velocity is directly related to the Rayleigh wave phase velocity as shown in Equation (2.5). This relationship is dependent on Poisson's ratio; and since Poisson's ratio for typical soils ranges from 0 to 0.5, it can be averaged to a Poisson's ratio value of 0.25 and further simplified as (Foti, 2000):

$$V_S \approx 1.1 \, V_R \tag{2.7}$$

To relate the inverted V_S values to a characteristic depth, the procedure uses the assumption that most the energy of the surface wave concentrates in the top half to third of the wavelength depth (Gazetas & Yegian, 1979). This behavior can be observed through the concentrated magnitude of the displacement amplitudes in the shallow regions shown in Figure 2.4. Mapping the measured phase velocities to a characteristic

27

depth, Z, representative of the inverted shear wave velocities is performed by scaling the

Rayleigh wavelength, λ_R. Such relationship can be estimated as:

$$Z = \frac{\lambda_R}{3} \text{ to } \frac{\lambda_R}{2}$$ (2.8)

With the inverted shear wave velocities determined from the approximation in

Equation (2.7) and the estimated depths computed from Equation (2.8), a shear wave

velocity profile is constructed, as shown in Figure 2.19.
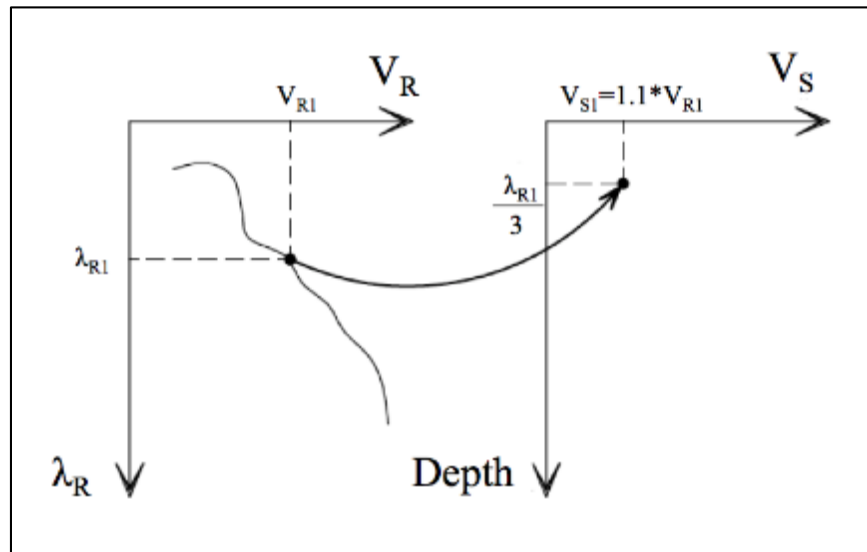
Figure 2.19   SSRM simplified inversion procedure.
(Adapted from Foti, 2000)

The SSRM method focused primarily on research applications and never gained

acceptance by the practicing community due to the time required to perform testing and

skepticism toward the use of empirically based inversion algorithms (Rix et al., 1991).

This method, however, provided significant contributions to the theoretical framework

for the surface wave methods to follow.

2.2.2.2   Spectral Analysis of Surface Waves (SASW)

Nazarian and Stokoe (1983) of the University of Texas at Austin introduced the Spectral Analysis of Surface Waves (SASW) method during the early 1980s. This method involved generating a wide frequency range of Rayleigh waves using a transient seismic source (e.g., sledgehammer), instead of a single testing frequency steady-state source. This simplified the surface wave testing of frequencies previously established by the SSRM. This idea was made possible by taking advantage of the development of the Fast Fourier Transform (FFT) algorithm developed by Cooley and Tukey (1965) and technological improvements in data acquisition equipment and computational tools (Foti, 2000; Lin, 2014). This led to a faster field test methodology and a more accurate inversion process than the SSRM (Foti, 2000).

The signals generated by the transient seismic source are recorded with two receivers. The recorded signals are processed with the FFT routine to estimate the difference in phase response, $\Delta\phi(f)$, between the two receivers for the range of frequencies generated by the seismic source. The time delay for each frequency, $\Delta t(f)$, can be calculated as:

$$\Delta t(f) = \frac{\Delta\phi(f)}{360*f}\ .\qquad\qquad(2.9)$$

Since the distance, ΔX, between the two receivers is known; the Rayleigh wave phase velocity can be calculated as:

$$V_R(f) = \frac{\Delta X}{\Delta t(f)}\ ,\qquad\qquad(2.10)$$

and the R-wave wavelength, λ_R, can be calculated as:

$$\lambda_R(f) = \frac{V_R(f)}{f}.$$
(2.11)

By following this procedure for each frequency, the dispersion curve can be determined.

Since using two-receivers imposes a frequency range limitation, different receiver spacing configurations are used to acquire a broader range of frequencies (and thus a broader range of wavelengths). For practicality, the receiver spacing is often doubled in every new test. Different receiver configuration strategies can be used to achieve this. The typical receiver array configurations are Common Mid-Point (CMP) and Common Source (CS); these are shown in Figure 2.20. The CMP is often preferred since it uses the source in a mirror configuration that can be used to verify tests reliability and check for any site inhomogeneity affecting the results (Foti, 2000).

(a)   (b)
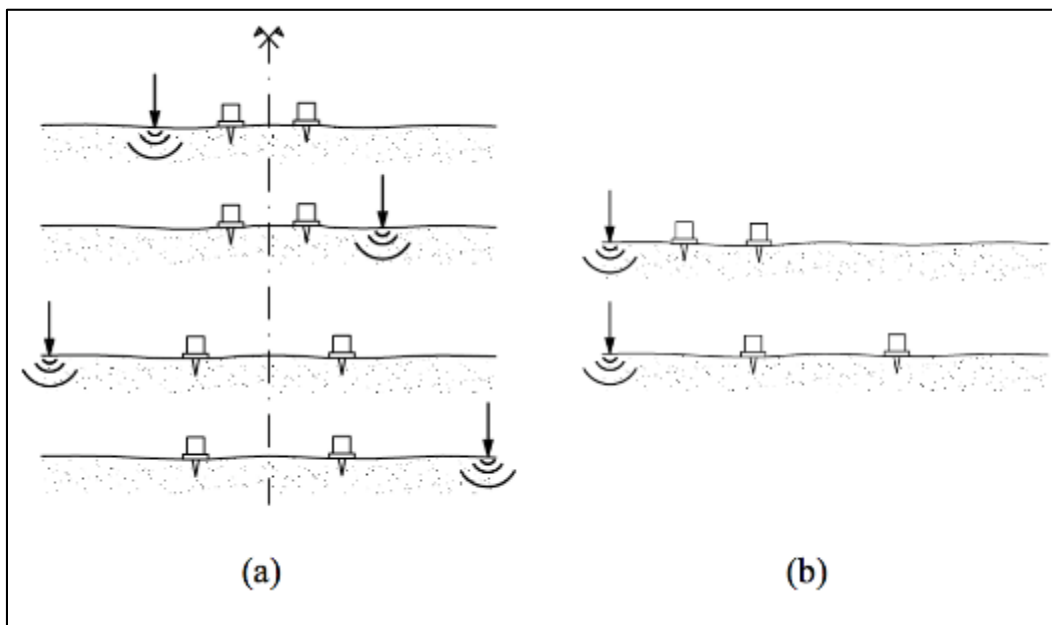
Figure 2.20   Acquisition strategies used in SASW.

Showing (a) Common Midpoint (CMP), and (b) Common Source (CS) configurations. (From Foti, 2000)

Regardless of the acquisition strategy used, the resulting dispersion curves from each receiver spacing and source offset experiment are combined into one single, composite curve to be used for inversion (Foti et al., 2015). Inversion can then be performed empirically as suggested by the SSRM method or more typically using least-squares techniques (Nazarian & Stokoe, 1983) such as presented later in this section.

The use of only a pair of receivers leads to the necessity of performing the test using several testing configurations and results in quite a time consuming procedure to collect all necessary data. Reconfiguration of receivers also leads to challenges when extracting noise from the signal due to possible misinterpretation of coherent and incoherent noise (Foti et al., 2015). In spite of its limitations, the SASW has been successfully implemented in several geotechnical projects and is still in widespread use (Foti et al., 2015).

2.2.2.3   Multichannel Analysis of Surface Waves (MASW)

A group at the Kansas Geological Survey (KGS) of the University of Kansas developed the Multichannel Analysis of Surface Waves (MASW, Park et al., 1999) method. The proposed MASW method employed the use of a multiple receiver approach (typically twelve or more) collinearly placed at the ground surface at an equidistant spacing, ΔX. This overcame some of the limitations of using the two-receiver approach established by the SASW and simplified the testing procedure by eliminating the need for different field receiver configurations. The most common acquisition configuration is the CMP, shown in Figure 2.20(a). A schematic of the typical data acquisition setup for MASW is shown in Figure 2.21.
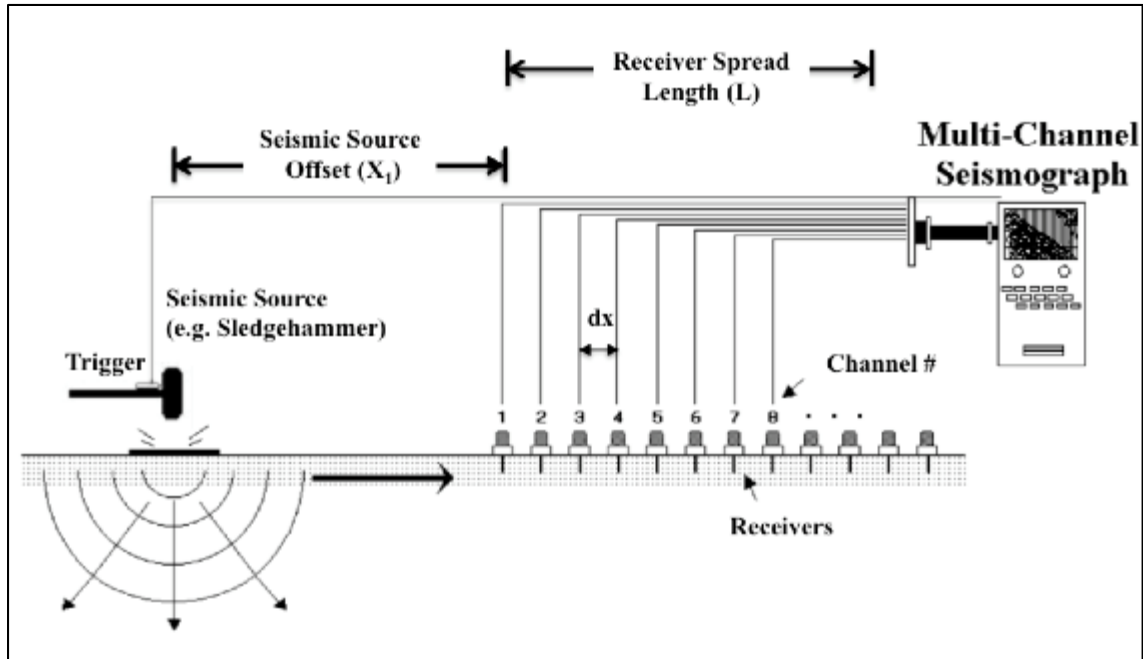
Figure 2.21   Typical MASW data acquisition setup.

(From Pnemadu and Park, 2005)

In the past two decades the application of the Multichannel Analysis of Surface

Waves (MASW) has emerged as a reliable, flexible, and affordable tool for estimating

shear wave velocity (V_S) profiles for use in geotechnical characterization of a site

(Penumadu & Park, 2005; Williams & Pnemadu, 2011). In addition, MASW results have

been reported to be in good agreement to other methods based on site stratigraphy and

shear wave estimates (Xia et al., 2000; Anderson & Thitimakorn, 2004; Penumadu &

Park, 2005) and thus has increasingly gained acceptance in the geotechnical community.

In a typical application, it is environmentally non-intrusive, affordable (e.g., less

equipment and labor intensive) and practical for covering areas of large extent.

The use of multiple receivers essentially filters out much of the incoherent noise

(Park et al., 1999). This allows for an improvement in quality control over the SASW

32

method since measurements from using only two stations may have introduced coherent and incoherent noise that would have been difficult to extract as previously mentioned in section 2.2.2.2.

With the introduction of a multi-receiver approach, a high-resolution dispersion image can be achieved to show the relation between phase velocity and frequency, discussed in section 2.2.2.3.1. A simplified inversion technique, discussed in section 2.2.2.3.2, was also introduced to construct a shear wave velocity using the dispersion characteristics. Algorithms using these techniques are implemented in KGS's SurfSeis® software, which was used for data processing and analysis under this study.

2.2.2.3.1   MASW Dispersive Energy Imaging Procedure

The transient source generates a seismic wave containing a broad range of frequencies, which are recorded by the receivers. Data obtained is recorded in the offset-time (x-t) domain, where offset, x, is the relative distance between the seismic source and a receiver, as shown in Figure 2.22(a). A multichannel data processing technique can be used to objectively determine dispersive trends of phase velocity for different frequencies. This is referred to as dispersive imaging. Three transformation methods are commonly used to achieve this: the f-k transform (Nolet & Panza, 1976), the τ-p transform (McMehan & Yedlin, 1981), and the *phase-shift* method (Park et al., 1998). For conciseness, only the phase-shift method is discussed since it is the one pertinent to this study. This method has been considered as a robust, cost-effective solution able to provide accurate phase velocities for detection of fundamental mode and isolate (or ignore) high frequency modes (Xia et al., 2007).

The phase-shift method consists of first applying a Fourier transform to decompose a multichannel record, $r(x,t)$, into its frequency components $R(x,\omega)$ as:

$$R(x,\omega) = \int r(x,t)e^{i\omega t}dt \ . \tag{2.12}$$

The frequency domain transform $R(x,\omega)$ can be written as a product of the amplitude, $A(x,\omega)$, and phase, $P(x,\omega)$, spectrums as:

$$R(x,\omega) = A(x,\omega)P(x,\omega) \ . \tag{2.13}$$

The amplitude spectrum term, $A(x,\omega)$, contains properties such as attenuation, spherical divergence, and source spectrum, which change with both seismic source offset and frequency (Ryden et al., 2004). The phase spectrum term, $P(x,\omega)$, contains information of time of arrival which reveals the dispersion properties, and thus phase velocity for each frequency (Park et al., 1998). Therefore, $R(x,\omega)$, can be expressed as

$$R(x,\omega) = A(x,\omega)e^{-i\Phi x} \ . \tag{2.14}$$

where $\Phi = \omega/c_\omega$ is the phase angle, ω ($=2\pi f$) is the angular frequency in radians, and c_ω is the phase velocity for a given frequency. Using the following integral transformation (Park et al., 1998):

$$V(\omega,\phi) = \int e^{i\phi x}\left[\frac{R(x,\omega)}{|R(x,\omega)|}\right]dx = \int e^{-i(\Phi-)x}\left[\frac{A(x,\omega)}{|A(x,\omega)|}\right]dx \ , \tag{2.15}$$

$R(x,\omega)$ is converted into frequency-phase-shift (ω-ϕ) domain. In essence, the integral transform $V(\omega,\phi)$ applies an offset-dependent phase-shift ($\phi=\omega/c_\omega$) and then performs a summation over the different trace offsets in $R(x,\omega)$. This is performed over an assumed frequency ω and phase velocity c_ω. $R(x,\omega)$ is normalized to compensate for the effects of attenuation and spherical divergence and insure equal weighting during the analysis of

the different trace offsets (Park et al., 1998). This results in maximum values of $V(\omega,\phi)$ for any given frequency ω, such that $\phi = \Phi = \omega/c_\omega$, because the amplitude spectrum $A(x,\omega)$ is both real and positive when normalized (Park et al., 1998). By changing the variables from phase, ϕ, to phase velocity, c_ω ($=\omega/\phi$), the phase-shift integral transform $V(\omega,\phi)$ is converted into frequency-phase velocity domain, $I(\omega,c_\omega)$ that defines a dispersive image.

This procedure is performed in practice by scanning through a specified range of phase velocities (e.g., 0-500 m/sec) by small increments (e.g., 1 m/sec) over a selected range of frequencies (e.g., 5-50 Hz) (Ryden et al., 2004). Figure 2.22(b) shows an example of the data for an individual frequency component of 20 Hz and how the scanning of different phase velocities compare to the normalized transform of $R(x,\omega)$ for that frequency. Note that at each given phase velocity, the phase was calculated to account for the offset-dependent phase shift. The resulting integral transforms for this frequency can be shown as a 2-D curve representation of $V(\omega,\phi)$ versus phase velocity, as shown in Figure 2.22(c). The procedure is repeated over a specified frequency range to obtain a dispersive image as shown in Figures 2.22(d and e). It can be observed that the 2-D representation is projected vertically in the dispersive image at a frequency of 20 Hz. If the fundamental mode (M0) is only present, single peak values of $I(\omega,c_\omega)$ will be observed for given frequency ω, shown in Figure 2.22(d). In the presence of significant amount of energy in higher modes, more than one peak will exist for given ω, as shown in Figure 2.22(e).
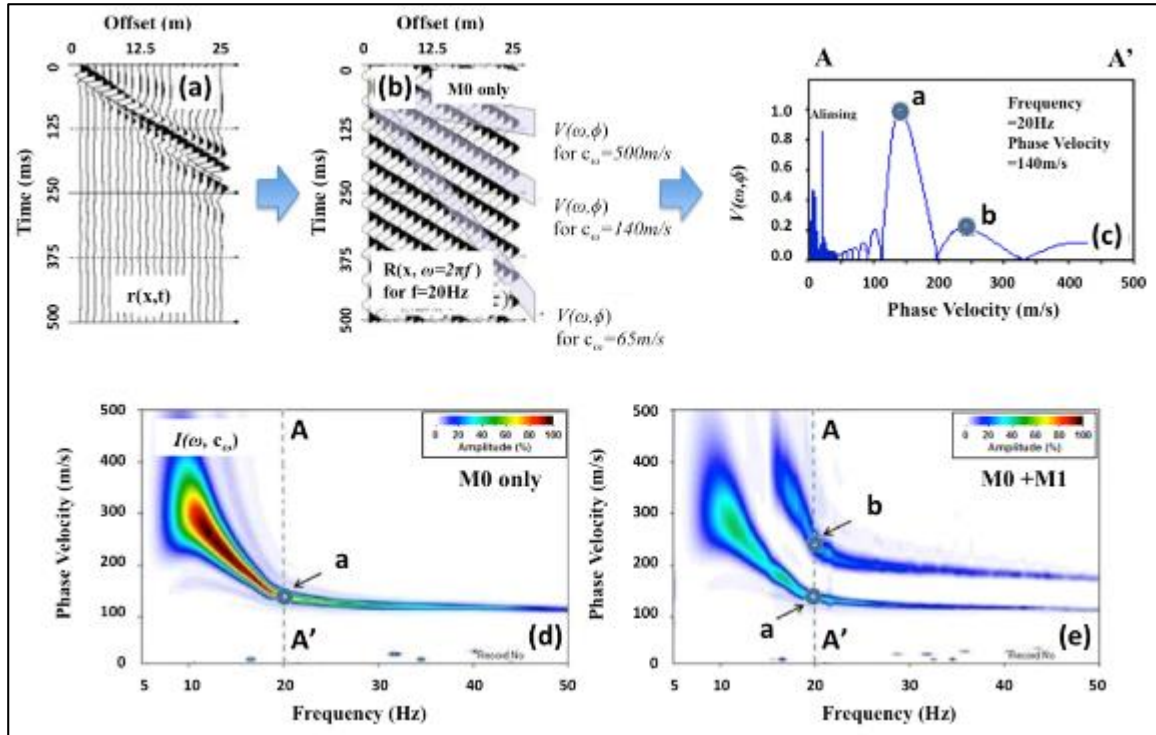
Figure 2.22   Dispersive image phase-shift method scheme.

Showing: (a) multichannel record in offset-time domain, (b) frequency transform for frequency of 20 Hz, (c) 2-D representation of normalization using integral transform, (d) dispersive image showing dominant fundamental mode, and (e) dispersive image showing fundamental mode and existence of higher mode. (Adapted from Park 2011)

The use of dispersive energy imaging permits: objective determination of dispersion curve nature (insensitive to data processing), multi-modal delineation in the presence of higher modes, and selection of parameters of interest to constrain the analysis.

Although isolation of different modes (if present) is achieved, only the fundamental mode (M0) is of interest to this study as discussed in section 2.1. Subjective interpretation is used to follow trends of interpreted peak amplitude fundamental mode in the dispersive energy image. Points of peak amplitude are selected to define the fundamental mode dispersion curve, as shown in the dotted line in Figure 2.23. The

dispersion curve is then used in an inversion process to obtain the V_S profile

representative to the center (or midstation) of the receiver spread.
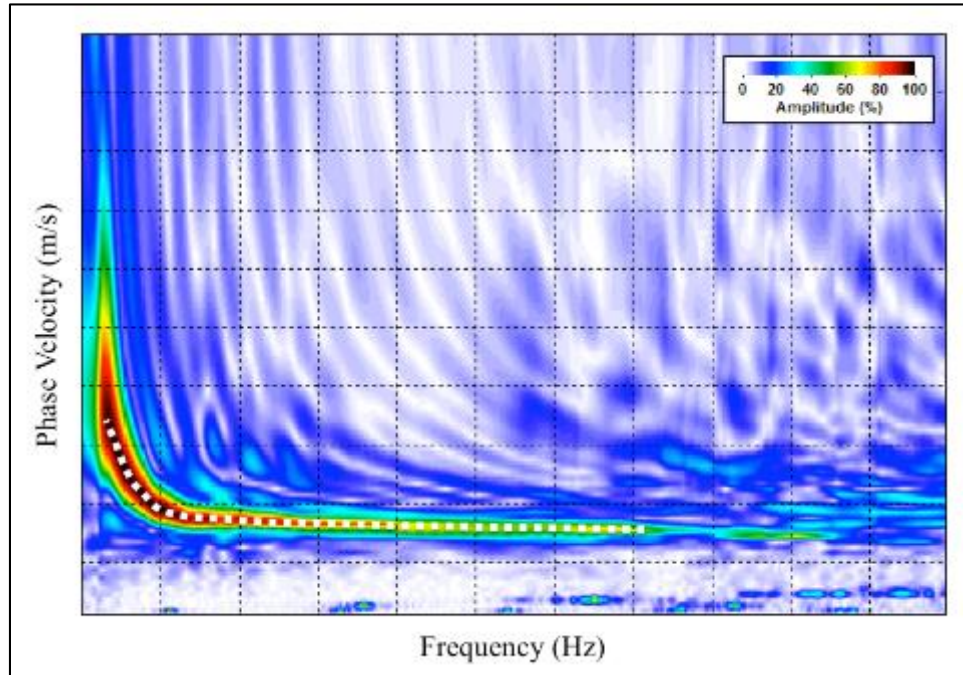
Figure 2.23   Dispersion curve selection from points of peak amplitude in dispersive
              energy image.

2.2.2.3.2   MASW Inversion Procedure

As stated before, the V_S profile can be determined through the solution of the

inversion problem, by relating the dispersion curve to the geotechnical subsurface

properties. A procedure is commonly performed to compare experimentally obtained

dispersion curves to a theoretically calculated dispersion curve found using assumed

subsurface properties (in some cases using a priori information from other geotechnical

tests). The theoretical dispersion curve is calculated from a forward model of Rayleigh

wave propagation that contains the four unknowns in the inversion problem, which are:

37

layer thickness (h), density (ρ), S-wave velocity (V_S; or interchangeably shear modulus (G) as shown in Equation (2.2) with known or estimated density and V_s) and Poisson's ratio (υ; or interchangeably V_P as shown in Equation (2.3)). Each of these parameters has different contributions to the dispersion curve calculations, however, the influence of Poisson's ratio and density are considered negligible. These can be estimated based on past experience without affecting the final results of the inversion (Foti, 2000). Thickness has a higher contribution than Poisson's ratio and density; however, the number of layers can be subdivided to account for any changes. Shear-wave velocity, V_S, has the most influence on the fundamental mode dispersion curve (Xia et al., 1999). This is taken into advantage by reducing the inverse problem from four unknowns to one unknown. This permits updating of only V_S, and leaving υ, ρ, and h unchanged through the inversion process (Park et al., 1999). V_S profile is iteratively updated until an acceptable match between the theoretical and experimental dispersion curves is obtained. Judgment regarding the effectiveness of the new iteration is performed by visual inspection or a least-square acceptance criterion (Foti, 2000).

The inversion procedure pertinent to this study is a simplified least squares approach established by Xia et al. (1999), using an iterative solution with the Levenberg–Marquardt and singular-value decomposition techniques. Details on the inversion will not be covered, as these require introduction to topics outside the scope of this study. Figure 2.24 shows the iterative procedure. An initial V_S profile is assumed and its respective theoretical forward dispersion curve is calculated. Fitting of the theoretical dispersion curve is compared against the experimentally measured dispersion curve points. It can be noted that the first iteration does not provide a good fit. The V_S profile is updated

iteratively until an acceptable fit of the theoretical dispersion curve to the measured

points is achieved. The final V_S profile iteration is assumed to be the shear wave profile

of the site.
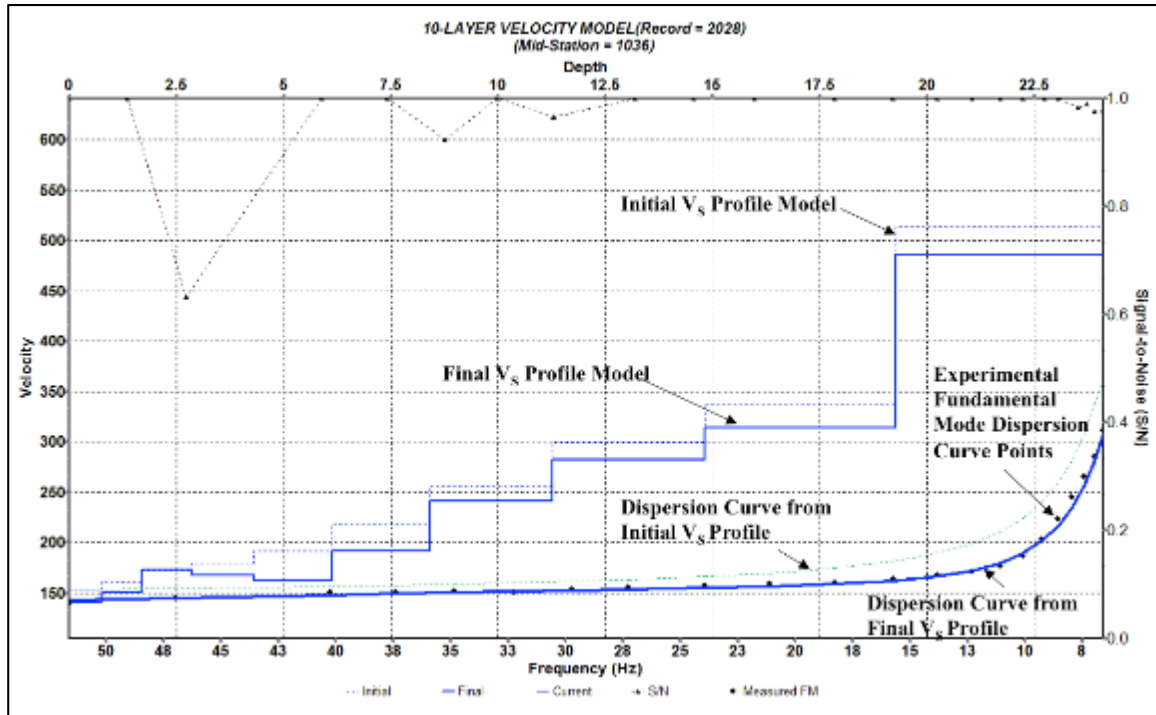
Figure 2.24   Iterative least-squares procedure used in the inversion process.
Shown are only the initial and final iterations.

As mentioned when discussing the SSRM method, estimating the dispersion

curve from the measured phase velocities needs to be performed by scaling the Rayleigh

wavelength, λ_R, to a characteristic depth, Z. Such relationship can be estimated as:

$$Z(f) = \alpha\,\lambda_R(f)\,, \tag{2.16}$$

where α is a coefficient that changes with frequency as shown in Figure 2.25. With this

relationship and relating the measured phase velocity, V_R, at Z(f) to V_S using

39

Equation (2.5) with an assumed Poisson's ratio, a V_S profile can be constructed. The

vertical V_S profile construction is performed, in essence, in the same way as the SSRM

method shown in Figure 2.19.
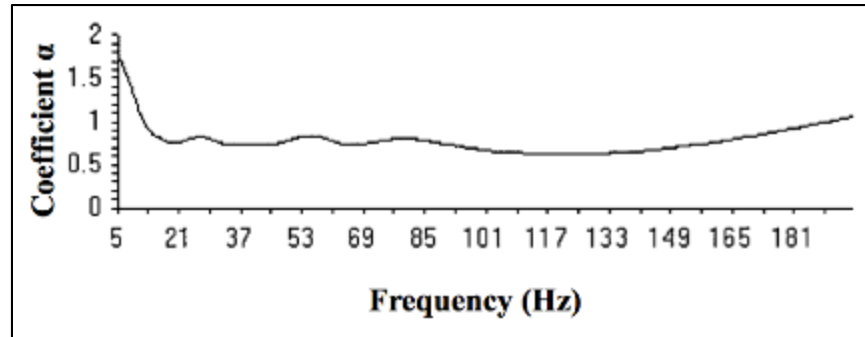
Figure 2.25   Coefficient α used to relate wavelengths to depths as function of frequency.
(From Park et al., 1999)

In general, inversion is not a trivial task since the solution is non-unique (Foti,

2000). Multiple possibilities of material parameters can yield a similar dispersion curve,

thus multiple stiffness profiles can exist. This results in a certain degree of uncertainty in

the final V_S profile. For the purpose of this research, non-uniqueness will not be

investigated; however, MASW analysis will be compared against a SCPT ground truth

verification test and an idealized FE model for differences in results.

2.3   Data Acquisition Receivers

To this point, the type of receiver used has not been specified, allowing for this

section to introduce geophones (which are typically employed in MASW surveys) and

distributed fiber optic sensors (FOS).

2.3.1 Geophones

Velocity transducers, commonly known as geophones, have a long success history and are the most commonly employed sensors in MASW data acquisition and seismic surveys (Hons, 2008). Geophones measure instantaneous velocity, which is proportional to an electric voltage generated by the movement of a spring-mounted magnetic mass inside a wire coil. When used in the ground, the measured velocity is proportional to the ground particle velocity at the discrete installed location. A schematic representation of a typical geophone and its parts is shown in Figure 2.26.
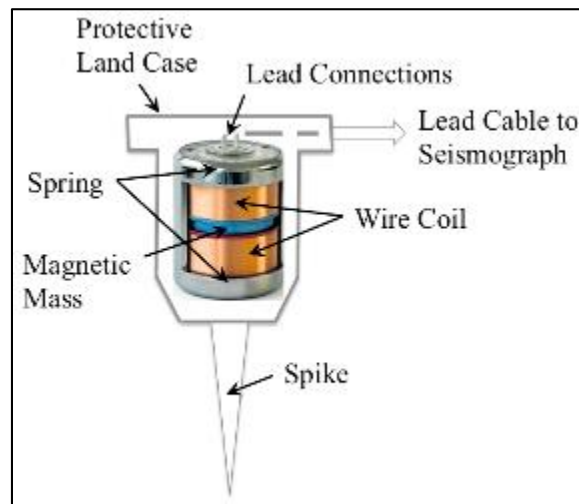
Figure 2.26   Schematic representation of the parts of a moving coil geophone.

MASW surveys typically make use of an array of twelve or more collinear vertical geophones to measure seismic wave propagation velocity. Low frequency geophones (i.e., 4.5 Hz) are typically recommended for MASW data acquisition (Miller et al., 2000). These are coupled to the ground by pushing the geophone-attached spike (1 to 3 in. in length) into the ground surface at a desired spacing. Each geophone, referred

to as a channel, responds to the ground vertical motion, such as that resulting from an active seismic source (e.g., sledgehammer). Vertical motion response is recorded with time as a seismogram. The typical setup requires: seismographs capable of connecting all geophone channels, batteries, spread cables to connect geophones, sync cable to interconnect seismographs, trigger cables for the active source, and communication cables for computer connection. This setup makes geophones highly adaptable temporary receivers for MASW surveys, but costly and maintenance intensive to employ in permanent long distance arrays. Figure 2.27 shows the complexity long arrays add with the amount of geophones and equipment required.

Figure 2.27   Equipment required for a long MASW survey.

(EPI Group, 2015)

2.3.2   Fiber Optic Sensing

An optical fiber consists of three components: a core, a cladding, and a protective coating, as shown in Figure 2.28. The fiber's core operates as a cylindrical optical waveguide and is composed of fused silica glass with an outer diameter (OD) that can

range from 5 to 10 μm for a single-mode fiber, to 50 μm for a multi-mode optical fiber

(Glisic, 2013). Single-mode fibers (i.e., smaller diameter core) are preferred because

higher data rates are achieved over long distances (Mitschke, 2010). A cladding, typically

with an OD of 125 μm, surrounds the core and it is composed of silica glass with a

slightly lower index of refraction. The outer layer consists of a protective coating for

environmental protection and physical robustness of the fiber (Glisic, 2013). The

protective coating has an OD of 250 μm but it can vary depending on the material and

design purpose. Multiple optical fibers can be bundled together into a fiber optic cable, as

shown in Figure 2.29, which can be used for multiple measurements (or multiple

transmissions as used in the telecommunications industry) and as spare fibers in case of

malfunction in one of the fibers being used as a sensor. Regardless of the number of

fibers in the fiber optic cable, the fiber optic sensor makes use of only one optical fiber.
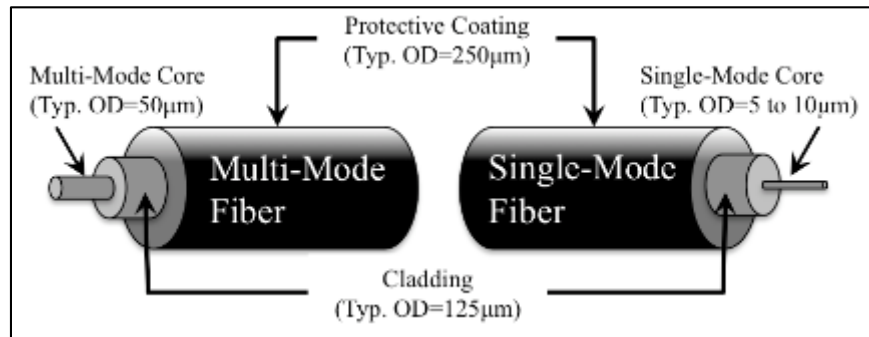
Figure 2.28   Components and typical outer diameters (OD) of a multi-mode and single-
mode optical fiber.
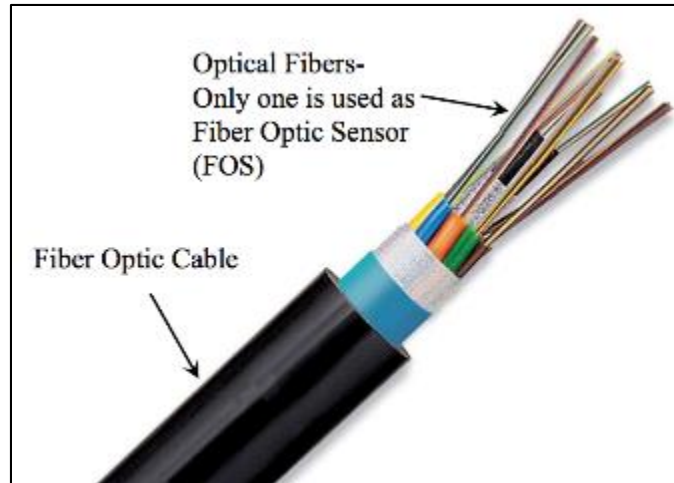
Figure 2.29   Example of a fiber optic cable.

(Adapted from EFON, 2015)

Single-mode optical fibers are ideal to carry optical signals over long distances; however, attenuation (i.e., losses) plays an important role in how far such signals can travel and be adequately measured. This is accounted by losses in the silica glass resulting from absorption, radiation, and Rayleigh scattering (Hui & O'Sullivan, 2009). The spectral contributions of absorption and Rayleigh scattering losses are shown in Figure 2.30. Absorption losses are caused by absorption of ultraviolet and infrared wavelength bands by pure silica molecules (Hui & O'Sullivan, 2009). Radiation losses are caused by fiber bending in the manufacturing process (Hui & O'Sullivan, 2009). Rayleigh scattering losses are caused by the statistical microscopic defects in the silica glass, which produce localized variations in density (Mitschke, 2010; Bao & Chen, 2012). The Rayleigh scattering phenomenon occurs in the optical fibers because the particles causing scattering are much smaller than the wavelength of the optical signal (Hui & O'Sullivan, 2009). As seen in Figure 2.30, Rayleigh scattering dominates the total

44

loss of the fiber, at the wavelengths typically used in FOS, 1310 nm and 1550 nm (Hui & O'Sullivan, 2009).
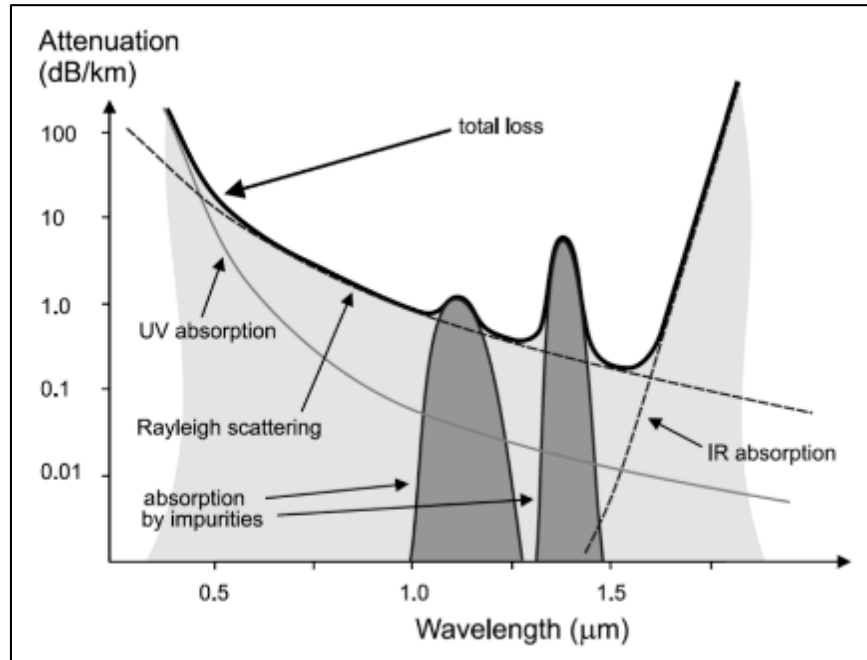
Figure 2.30   Losses in a single mode optical fiber.

(From Mitschke, 2010)

Rayleigh scattering creates a backward propagating wave at the same frequency that is known to be proportional to the power of the incident light (Bao & Chen, 2012). The backward propagating wave (Rayleigh backscatter) is used in the FOS measurement system, as discussed in the next subsection. A schematic representation of the Rayleigh scattering process is shown in Figure 2.31. In Rayleigh scattering, no energy is transferred to the silica glass and no changes in frequency occur from the incident to the scattered light, hence it is referred to as linear scattering (Bao & Chen, 2012).
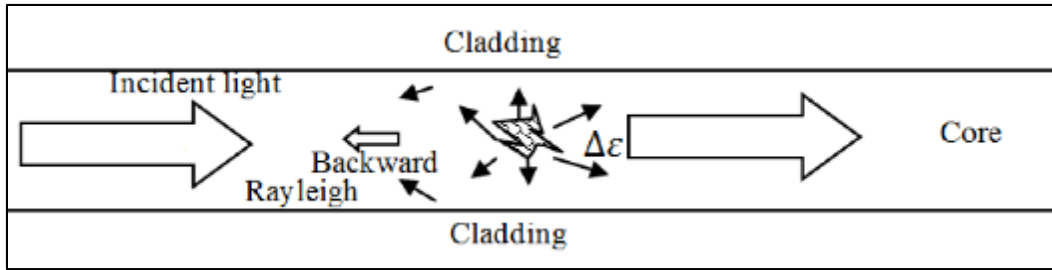
Figure 2.31   Representation of spontaneous Rayleigh scattering process.
(From Bao and Chen, 2012)

2.3.2.1   Optical Time Domain Reflectometry (OTDR)

By introducing a laser pulse into the fiber, a forward propagating incident light is guided through the optical fiber. Some of the Rayleigh backscattered light travels in a direction 180° to the incident light and is returned to the source (Udd, 1990). The variation of the returned backscatter intensity can be monitored and attenuation as well as spatial variation can be obtained as a function of time. The optical time domain reflectometry (OTDR) was introduced using this idea for diagnostics and determining location of faults along an optical telecommunications fiber (Udd, 1990; Bao & Chen, 2012). OTDRs later evolved into sensing applications, where any local perturbation (e.g., strains, vibrations) affecting the optical fiber was observed to modulate the backscattered signal (Bao & Chen, 2012), as shown in Figure 2.32. In doing so, optical fibers can be used to sense physical measurements throughout its length, thus achieving distributed fiber optic sensors (FOS).
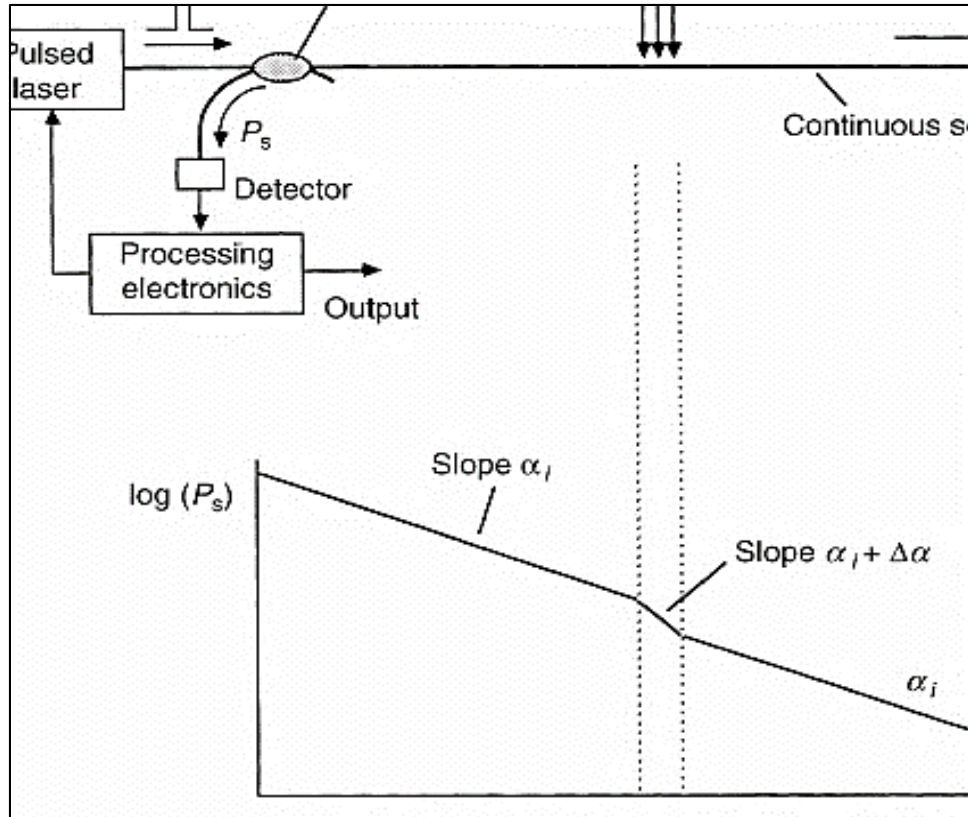
Figure 2.32   Operation of an optical time domain reflectometer.

(From Udd, 1990)

2.3.2.2   Fiber Optic Strain Sensing

For the current application, FOS reveals strain information within sections of the

fiber, referred to as zones. An interrogation light pulse of specified duration is injected

into a fiber optic cable from a narrow line-width, coherent laser. As the light pulse

propagates through the fiber, backscattered light travels to the OTDR interrogator where

the laser pulse was emitted (Bao & Chen, 2012). At the interrogator the backscatter signal

from both ends of a fiber zone are combined. The mixed signal is demodulated to

determine the change in phase, $\Delta\phi$, which is the output of the interrogator.

An acoustic or seismic disturbance will produce strains within a fiber zone, which in turn, will cause the optical path length within that zone to change. The change in phase, $\Delta\phi$, is caused by the changes in optical length over a zone length of fiber, L. The change in optical length is proportional to the longitudinal strains, $\mathcal{E}_x$, exhibited in the fiber (modified from Udd, 1990):

$$\frac{\Delta\phi}{L} = k\xi n\mathcal{E}_x = k\xi n\frac{dL}{L},$$ (2.17)

where: k is the optical wavenumber in a vacuum ($\frac{2\pi}{\lambda}$, where λ is the wavelength of the interrogation light pulse); ξ is the strain optic correction factor (typically having a value of 0.78); n is the index of refraction of the silica glass core in the fiber (typically about 1.46); and dL is the change in length of the fiber. The length L can be canceled on both sides of Equation (2.17). For a typical pulse wavelength of 1550 nm, this results in a proportional relationship of optical phase shift with the elongation of the fiber:

$$\Delta\phi \approx 4.43E6 * dL .$$ (2.18)

In the case of this study, strains are generated from seismic disturbances occurring in the ground and transferred to the buried fiber. The measured phase difference is proportional to longitudinal strains over lengths of fiber along the entire FOS length. Longitudinal strain obtained with the FOS is averaged over each zone length of fiber. The fiber zone sensing lengths (typically 5 to 10 m) are based on the averaging of multiple spatial resolutions to achieve better signal to noise ratio (Udd, 1990). A schematic of the averaging of strain when compared to the strains at the fiber is shown in Figure 2.33.
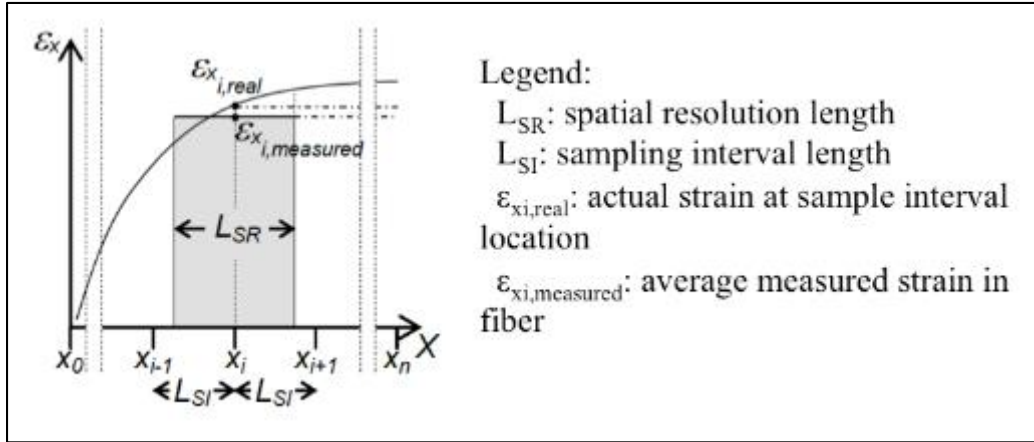
Figure 2.33   Strain measurement averaging in a fiber zone using a distributed fiber optic sensor.

(From Glisic, 2013)

The strain proportional change in phase is obtained as a function of time by repeating the light pulse with time. After the pulse travels the whole length of fiber and back, the pulse is repeated. The pulse repetition rate determines the actual sampling rate the data is recorded.

In addition to its sensing capabilities, the FOS serves as a transmission medium simplifying the installation setup into a cleaner layout for easier bookkeeping of channel locations. Because of the simplified setup, it requires less equipment and therefore less maintenance, thus making FOS installation more cost efficient to implement over long distances. Distributed fiber optic sensor (FOS) systems offer the potential of using buried fiber optic cable over distances that can reach up to 100 km (Bao & Chen, 2012).

2.3.3   Seismic Surveying using Distributed Fiber Optic Strain Sensing

The use of seismic surveying using distributed fiber optic strain sensing systems have been mostly dedicated to the oil and gas industry for monitoring well applications to

detect leakage and monitor contaminants through the use of vertical seismic profiling (Cox et al., 2012; Webster et al., 2013). These applications have showed very reasonable agreement between measurements with distributed FOS and conventional geophones, but have been mostly in borehole configurations and attached to pipelines.

The Engineer Research and Development Center (ERDC), Vicksburg, MS has investigated the use of FOS in SASW analysis and compared to horizontal and vertical geophones (Costley et al., 2015). The primary objective of the investigation was to compare the coherence of the signals measured with FOS and geophone sensors and to evaluate the use of array processing techniques for processing FOS signals. The dispersion curves from different FOS zones showed decent agreement with the dispersion curves obtained from geophones. No inversion was performed to find the resulting V_S profile.

Daley et al. (2013) showed early indications of using buried distributed FOS for surface wave analysis. They observed a high content of Rayleigh waves in FOS measurements as part of a CO_2 monitoring pilot program on a site located in Victoria, Australia. Only initial results were shown and details on installation protocols and depths were not mentioned. Results showed only dispersive imaging performed with the *f-k* transform method; results from shear wave inversion or comparison to geophone results were not presented. It was also noted that Daley et al. (2013) used a specialized FOS cable. Glisic (2013) presented costs of different specialized fiber optic sensor configurations and showed that specialized fibers may cost 15-30 US$/m when compared to standard telecommunication fiber optic cables which range from 2-5 US$/m. Although the specialized FOS may provide better signal to noise ratio, it will be more expensive

over long runs when compared to standard telecommunication optical fiber cable as considered herein. This further justified exploring standard telecommunication fiber optic cables as proposed in this study. This study intends to verify the feasibility of using FOS for MASW analysis and cover further details to expand its application.

CHAPTER III

FIELD EXPERIMENTS METHODOLOGY

3.1   **Introduction**

    Field experiments were conducted at a site referred to as the Test Track located on

the Engineer Research and Development Center (ERDC, previously known as the

Waterways Experiment Station, WES), Vicksburg, MS. The site was selected due to an

existing installation of standard telecommunication optical fiber cable. The fiber optic

cable had been installed along the shoulder of an unsurfaced road at depths of 0.5 m and

1.0 m along the same alignment, as shown in Figure 3.1. A linear 120 m section of cable

was chosen for this study. A linear array of vertical geophones was installed on the

ground surface over the location where the fiber cable was buried. Data was collected

from the two types of sensors and subsequently compared.

Figure 3.1   Test site overview showing approximate location of buried FOS.

3.2   Site Description

No site-specific geotechnical information was available at the time the tests were

performed. Geologic information from the 680 acres ERDC facility describes

6 distinguishable geologic units determined from a selection of 92 logs boring logs

(Murphy & Albertson, 1996). The reported geologic units, from oldest to youngest, were:

"(1) the Eocene Yazoo Clay, (2) the Oligocene Forest Hill Formation, (3) the Oligocene

Mint Spring Marl, (4) the Oligocene Glendon Limestone, (5) an undifferentiated

uppermost Tertiary unit consisting of the Miocene Catahoula Formation and Oligocene

Formations, presumably the Bucatunna Clay and Byram Marl, and (6) the Pleistocene

Vicksburg loess". Four deep borings, shown in Figure 3.2, were selected by Murphy &

53

Albertson (1996) to show the variation of these geologic units within ERDC. A vertical

profile constructed from these borings, in conjunction with electrical resistivity

measurements (E-logs), is shown in Figure 3.3.
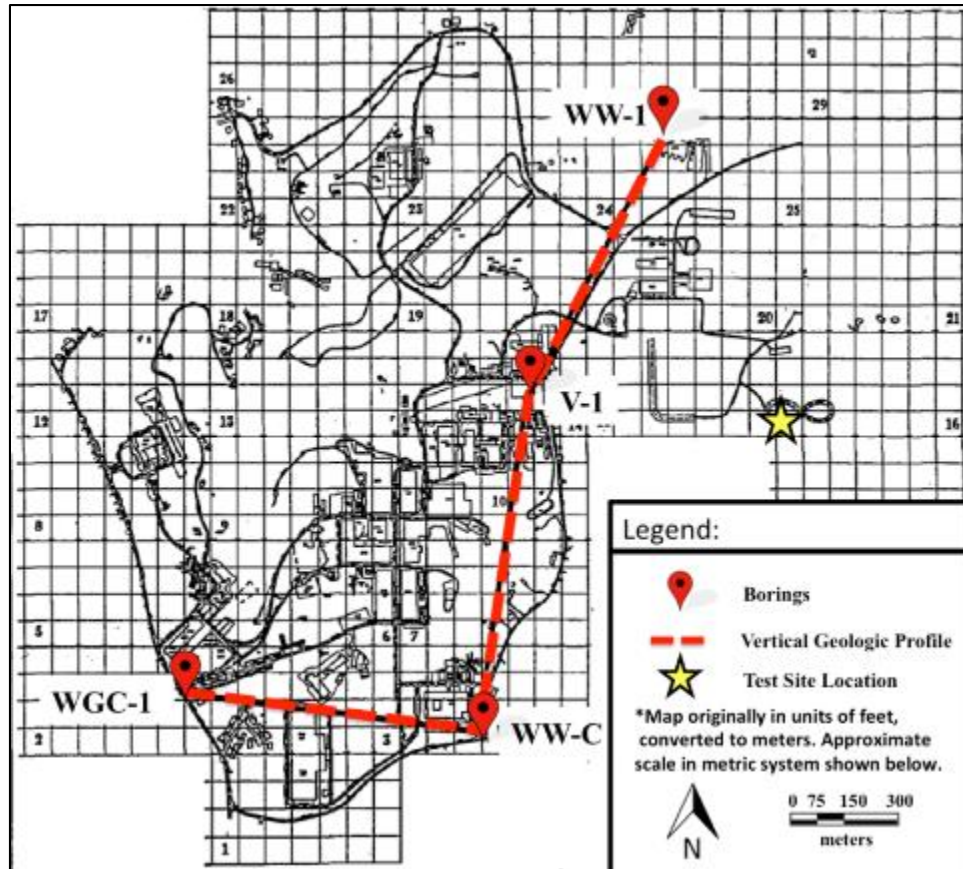
Figure 3.2   General plan of ERDC facility.

Showing location of geologic profile and location of four deep borings relative to the test
site. (Adapted from Murphy & Albertson, 1996)

From these geologic units, the Glendon Limestone is considered to be the first

"rock" encountered in borings in the ERDC area (Murphy & Albertson, 1996). It is

assumed that the depth of investigation from the MASW analysis will be controlled by

this geologic formation. At this depth, shear wave velocities drastically increase

compared to the overlying geology. Seismic signals traveling to the underlying geology

will be attenuated by the Glendon Limestone and will not be captured in the acquired

seismic signals for MASW analysis. For that reason underlying geologic units are not

discussed.
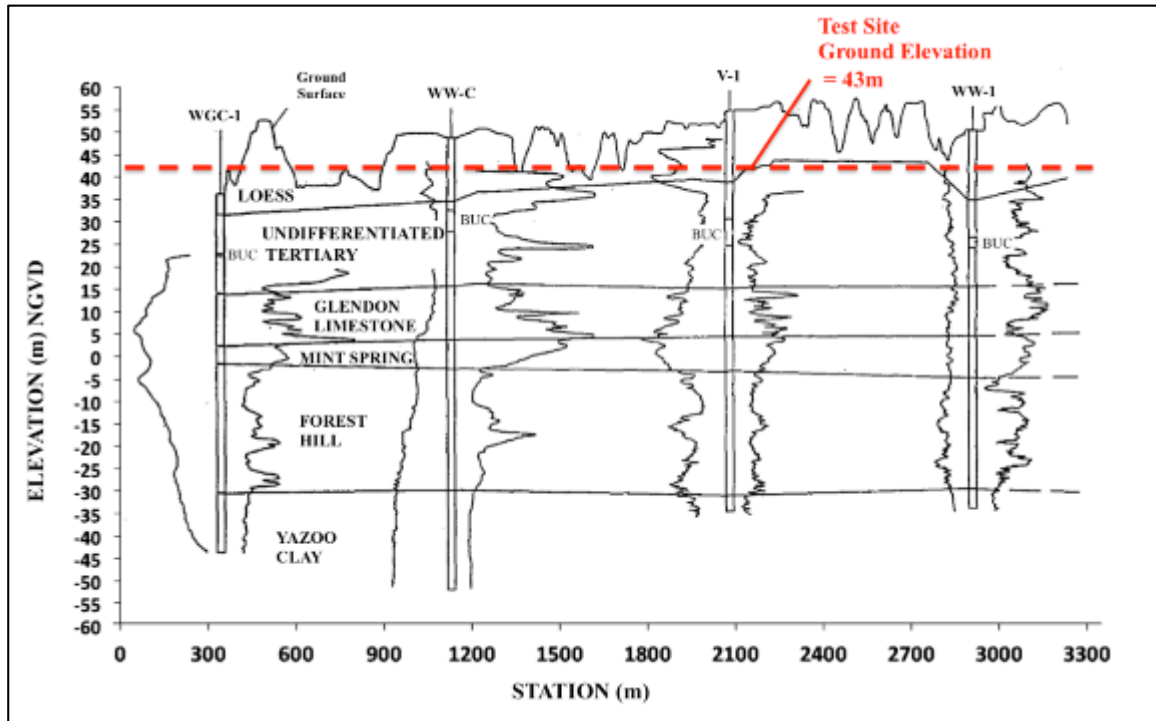
Figure 3.3   Vertical profile for four borings at ERDC.

Showing geologic units, E-logs, and corresponding ground surface elevation at the test
site. (Adapted from Murphy & Albertson, 1996)

The ground surface elevation at the test site location is approximately 43 m, as

shown in Figure 3.3. Contours of top elevation of the Glendon Limestone are shown in

Figure 3.4. According to these contours, the top elevation of the Glendon Limestone at

the test site is expected to be between the 60- to 80-ft (approx. 18- to 24-m) contours.

This results in an expected depth to the Glendon Limestone at the test site between 19 to

25 m. This range in depth were considered to be the depths of investigation that would be achieved through the MASW analysis. Water contents for the Glendon Limestone had been reported between 26.1 to 33.3% (Murphy & Albertson, 1996). No strength characteristics or other geotechnical information was found.
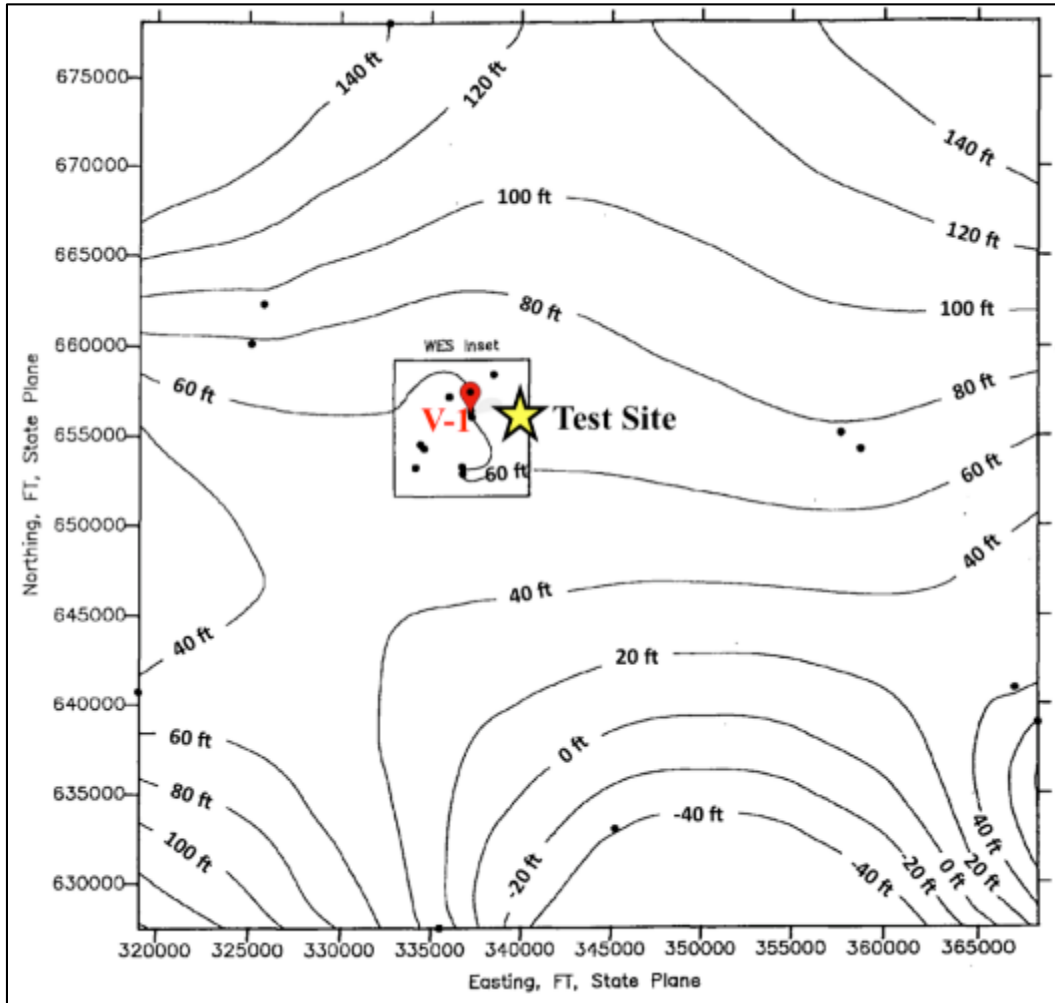
Figure 3.4   Top elevations of Glendon Limestone surface in central Warren County, MS.

Test site location shown with yellow star and location of closest boring V-1 shown with red balloon symbol. (Adapted from Murphy & Albertson, 1996)

The two upper geologic units, i.e., the Undifferentiated Tertiary and the Vicksburg Loess, are the primary geologic units assumed to be captured in the site under investigation. The top elevations of these two geologic units vary considerably by location, as shown in Figure 3.3. Since no other borings were found in the proximity of the test site, it was assumed that the geologic profile would resemble the vertical profile for boring V-1. The location of this boring was approximately 800 m west of the test site. Based on the site ground elevation projected onto this vertical profile, the Undifferentiated Tertiary unit will extend from the Glendon Limestone (at around 19 to 25 m in depth) up to an approximated depth of 3 to 8 m from the top surface. As previously mentioned the Undifferentiated Tertiary consists of three different formations (from oldest to youngest): the Byram Marl, Bucatunna Clay, and the Catahoula.

The Byram Marl Formation consists of a mix of clayey marl and limy clay. Water contents have been reported to range from 22.1 to 54.8%, with mean values of 30.2% (Murphy & Albertson, 1996). Relative strengths of 12 to 46 blows per foot with a mean of 28 blows per foot have also been reported (Murphy & Albertson, 1996). A variety of empirical correlations relating SPT-N values to shear wave velocity are available (Brandenberg et al., 2010). For simplicity in calculations, the correlation from Seed & Idriss (1981), $V_S = 61.4 * N^{0.5}$, was chosen to get an estimated V_S range. Using this correlation, V_S results in a range of about 210 to 425 m/sec and a mean of 325 m/sec.

The Bucatunna Formation is identified as a dark gray to brown fat clay (CH). The thickness of this formation varies across ERDC and may or may not be present (Murphy & Albertson, 1996). No strength characteristics or other geotechnical characteristics were found regarding this formation.

57

The Catahoula Formation consists of gray to white sands, silts and silty clays. Green & Bograd (1973) mentioned that some of the Catahoula sands are hardened in sandstone layers. They also suggested a range from 22 to 90 blows per foot for sandy Catahoula. Based on the SPT-N V_S empirical correlation by Seed & Idriss (1981), this results in a range of about 290 to 580 m/sec. Green & Bograd (1973) also indicated a range of undrained shear strengths (S_u) for weathered to unweathered clayey Catahoula of 800 to 4000 psf, which is about 38.3 kPa to 191.5 kPa. Using the empirical correlation of S_u values to shear wave velocity from Dickenson (1994), $V_S = 23 * S_u^{0.475}$, results in V_S values in the range of about 130 to 279 m/sec. To cover the different ranges of the Catahoula formation, values can be summarized to range from 130 to 580 m/sec.

Above the Undifferentiated Tertiary lies the Vicksburg Loess which is expected to cover the top 3 to 8 meters below the ground surface. Loess consists of a windblown deposit with mainly silt-sized particles. Available information on Vicksburg Loess includes liquid limits (LL) between 21 and 43, plastic limits (PL) between 19 and 29, and plasticity index (PI) between 2 and 16 (Murphy & Albertson, 1996). Reported densities were 79.4 to 104.2 lb/ft^3, which is about 1.27 to 1.67 g/cm^3. Specific gravity was described to range from 2.69 to 2.74. Water contents were reported between 18 and 33%. Undrained shear strengths (S_u) of 0.06 to 1.04 tsf have been reported, which is about 5.75 to 99.59 kPa. Using the empirical correlation of S_u values to shear wave velocity from Dickenson (1994) results in V_S values in the range of about 52 to 204 m/sec.

The site used in this study had been previously used for assessing the effects of tire pressures on different road surfaces. The primary interest of these previous studies was in the proximity of the surface for pavements and for soils to be used as a base or

subbase material. Reports indicated the test site consisted of a "lean clay (loess) deposit" (Grau, 1993), which confirms this upper layer. No information regarding other geologic units was mentioned.

A summary of ranges of depths and V_S of the expected geologic formation are shown in Figure 3.5.
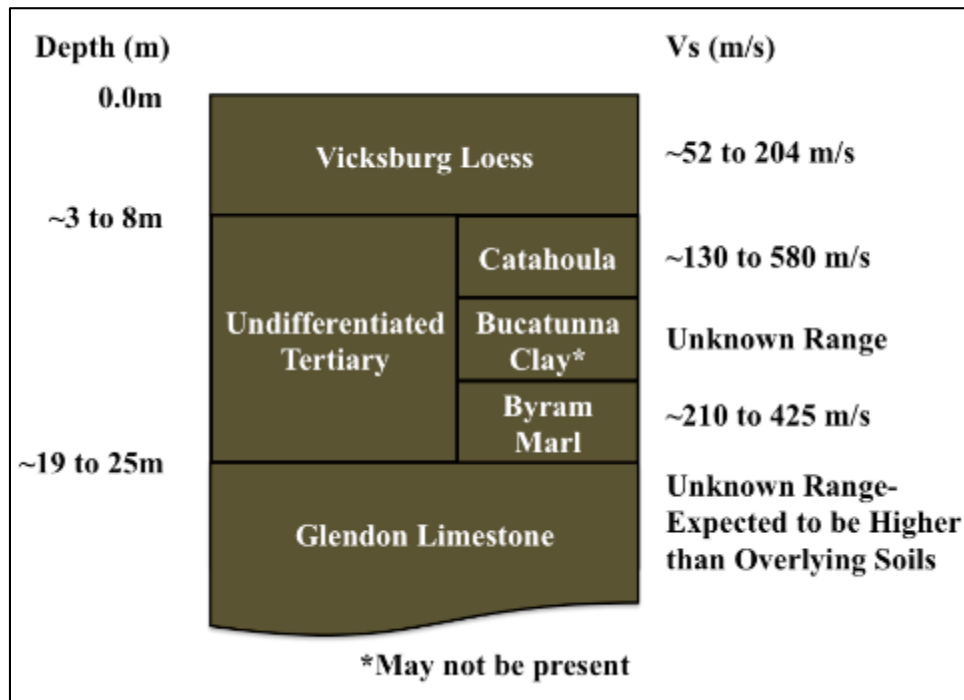
Figure 3.5   Summary of ranges of depth and shear wave velocities based on the expected geologic formations at the test site.

To provide ground truth verification, a Seismic Cone Penetration Test (SCPT) will be conducted at the test site location to verify the shear wave velocity profiles determined using MASW.

3.3   Equipment

3.3.1   Geophone Data Acquisition

Seventy-two 4.5 Hz vertical geophones manufactured by Geospace

Technologies® were used, shown in Figure 3.6(a). Geophones were connected thru a

spread cable to 24-channel Geometrics Geode® seismographs, shown in Figure 3.6(b).

Since 72 channels were used, three seismographs were required and a sync cable was

used to interconnect these. The seismographs were powered using 12V batteries. A

trigger switch connected to the seismographs was attached to a sledgehammer, as shown

Figure 3.6(c). The trigger switch initiated recording during the active seismic surveys. A

striker plate coupled the energy imparted by the sledgehammer into the ground. A digital

cable connected seismographs to a PC. A PC software called Geometrics Seismodule

Controller® enabled setup configuration and data acquisition parameters and saved the

survey records. Data was sampled at 1000 Hz (i.e., sampling interval of 0.001 sec) for a

total recording time of one second.
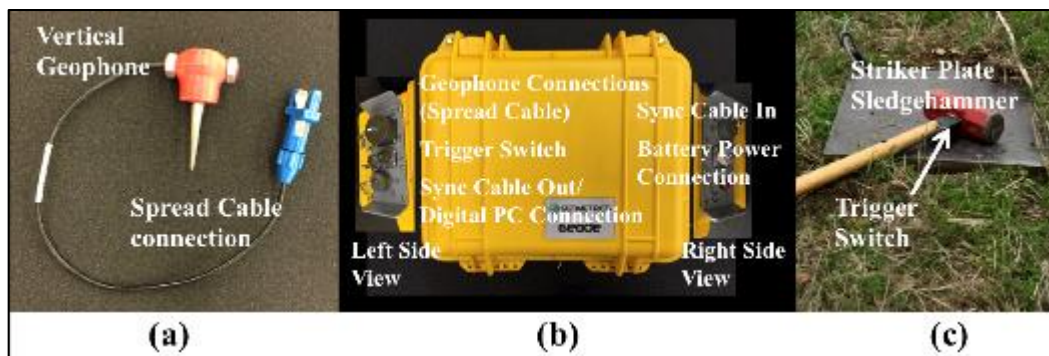
Figure 3.6   Geophone data acquisition system.

(a) Low frequency (4.5-Hz) vertical geophone. (b) Seismograph and connections.
(c) 4.5-kg (10-lb) Sledgehammer with attached trigger switch, and striker plate for
ground coupling.

3.3.2   FOS Data Acquisition Equipment

The fiber optic system data acquisition system consisted of a standard fiber optic telecommunications cable and a coherent OTDR interrogator.

The fiber optic telecommunications cable contained 24 single-mode Corning® SMF-28e+® fibers as shown in Figure 3.7(a, b). The fibers are arranged in a ribbon configuration inside a protective armor and coatings, as shown Figure 3.7(b). Only one of the fibers was used as a sensor, as shown in Figure 3.7(c).
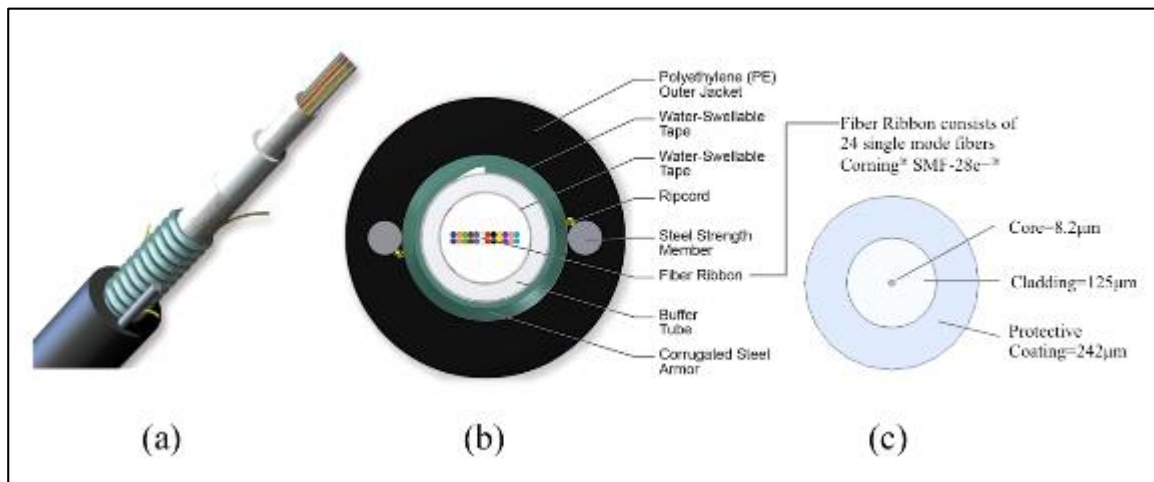
Figure 3.7   FOS data acquisition system.

(a) SST-Ribbon™ Single-Tube, Gel-Free, Armored Cable, 24 F, Single-mode (OS2).
(b) Cross section representation. (c) Schematic of single mode SMF-28e+® fiber used as FOS. (From Corning 2015)

The fiber was connected to a Coherent OTDR interrogator manufactured by Optiphase® referred to as the CR3 Prototype System (Optiphase, Inc., 2012). This system contains the laser and receives and demodulates the coherent Rayleigh backscatter from laser pulses. According to the manufacturer's specifications, this system is capable of interrogating 25 km of fiber optic cable and measures the change in optical phase, or

optical path length, over 5-m sections of fiber optic cable, referred to as zones. The zones

are distributed every 2.041 m, and thus overlapped. After the laser light pulse is emitted,

the subsequent digitizer records the Rayleigh backscatter of the light pulse to define each

respective zone along the fiber optic cable. The light pulse is repeated to control the

recording sampling rate. During these experiments the light pulse was repeated at a rate

of 5000 Hz, which gave a sample interval of 0.0002 sec. Data was retrieved for a total

recording time of one second, similar to the geophone data. Data was recorded

simultaneously with both the geophone seismographs and FOS. The sledgehammer

connected to the geophone seismographs generated the seismic excitation.

3.4   Test Setup and Procedure

MASW field experiments were performed over a 120-m section, as shown in

Figure 3.1. Within this section, 72 geophones were placed at 1-m spacing along the

ground surface. The 1-m receiver spacing is typically sufficient for most sites to provide

adequate spatial resolution for the soil layers to be resolved under the MASW analysis

(Park et al., 2002). Furthermore, since the spacing between the FOS zones is about two

meters (i.e., 2.041 m), the 1-m spacing provided additional spatial resolution in the event

spatial aliasing was observed on the FOS data. In this manner FOS data quality control on

the FOS data could have been accounted for. During post-processing, it was noted that

using the data from the 72 geophones at 1-m spacing or choosing 24 geophones at 3-m

spacing from the original data produced negligible differences. For that reason, the use of

1-m geophone spacing was considered reasonable when comparing to the FOS at a larger

spacing.

There were 36 FOS zones at the 2.041-m distributed spacing for both FOS installations depths. Start and end locations along the fiber had been pre-determined by observing FOS zones of higher amplitudes response relative to sledgehammer surface impact locations.

Selection of seismic source offset with respect to the location of the receivers is an important part of designing a MASW survey to prevent contamination from near-field and far-field effects. The goal is to select an offset so that the wave field contains only plane surface wave components and not be affected by body waves and higher modes (Foti et al., 2015). Near-field and far-field effects are minimized by proper choice of distance between the source and nearest receiver, commonly known as source offset (X_1), and the receiver spread length (L), respectively (Park et al., 1999).

Park et al. (1999) suggested a rule of thumb by setting the offset equal or larger to the maximum depth of interest, Z_{max}. In 2010, Park & Carnevale investigated multiple receiver offsets and observed error estimation of phase velocities appear to be highly site dependent. In one instance, a source offset of one receiver spacing was used and compared to further offset distances. Differences in their respective dispersion curves were negligible. Similar results were obtained for an offset of 1 receiver up to an offset of 24 receivers. In the current study, the offset was selected based on a percentage of the total spread length (i.e., %L, where L is the length of installation or spread). The selected source offsets (and respective percentage of spread length) were 1 m ($\approx$1.5%L), 2 m ($\approx$3%L), 6 m ($\approx$8%L), 10 m ($\approx$14%L), 18 m ($\approx$25%L), and 28 m ($\approx$40%L). Source offsets were applied to the left and right sides of the spread to verify lateral homogeneity. Since the test site was expected to be laterally homogeneous, the two source side offsets also

63

provided additional verification of repeatability of the results. Due to the presence of a culvert at an offset of 20 m from the left side of the spread, a maximum source offset of 18 m was used to avoid introducing inhomogeneity in the data. Larger source offsets could not be accomplished since the fiber cable did not continue in the desired linear alignment beyond these offsets and signal-to-noise (S/N) ratio observed in the fiber was observed to decay. The decay in the S/N ratio results from the high sensitivity of the fiber as it gets contaminated with environmental noise.

The spread length (L) is typically adjusted to avoid the maximum receiver offset (i.e., the distance from the source to the furthest-most receiver). The reason is that contamination of body waves results from rapid attenuation of high frequency (short wavelength) surface wave components (Park et al., 1999). Highest accuracy can be achieved using a spread length equal to the maximum desired wavelengths (λ_{max}), which is estimated to be about two times the maximum depth (Z_{max}) (Park & Carnevale, 2010). A maximum expected depth of around 25 m was considered for the test site as a result of the depth to the Glendon Limestone geologic unit, expected to be 19 to 25 m in depth (Murphy & Albertson, 1996). Under this study, the spread length used was 71 m for the geophones and about 71.5 m for the FOS spreads. With these spreads, maximum measurable wavelengths will correspond to depths of about 30 m considered to be able to resolve further than the maximum expected depths.

Park et al. (1999) recommended guidelines of optimum MASW field installation for the source offset distance and spread length to avoid near-field and far-field effects. These were not strictly adopted and are justified by the purpose of this study to compare

the response on the FOS with traditional geophones regardless of source location and spread length configuration.

A schematic of the experimental setup is shown in Figure 3.8. Spacing and receiver location of geophones and FOS were maintained constant during the experiment. A 4.5-kg (10-lb) sledgehammer was used as the active seismic source for the experiments at the source offsets specified previously. Each sledgehammer impact, referred to as a shot record, was recorded simultaneously with both the geophone and FOS arrays. Three shot records were performed at each active source location for repeatability and use in stacking of records to increase signal-to-noise ratio.
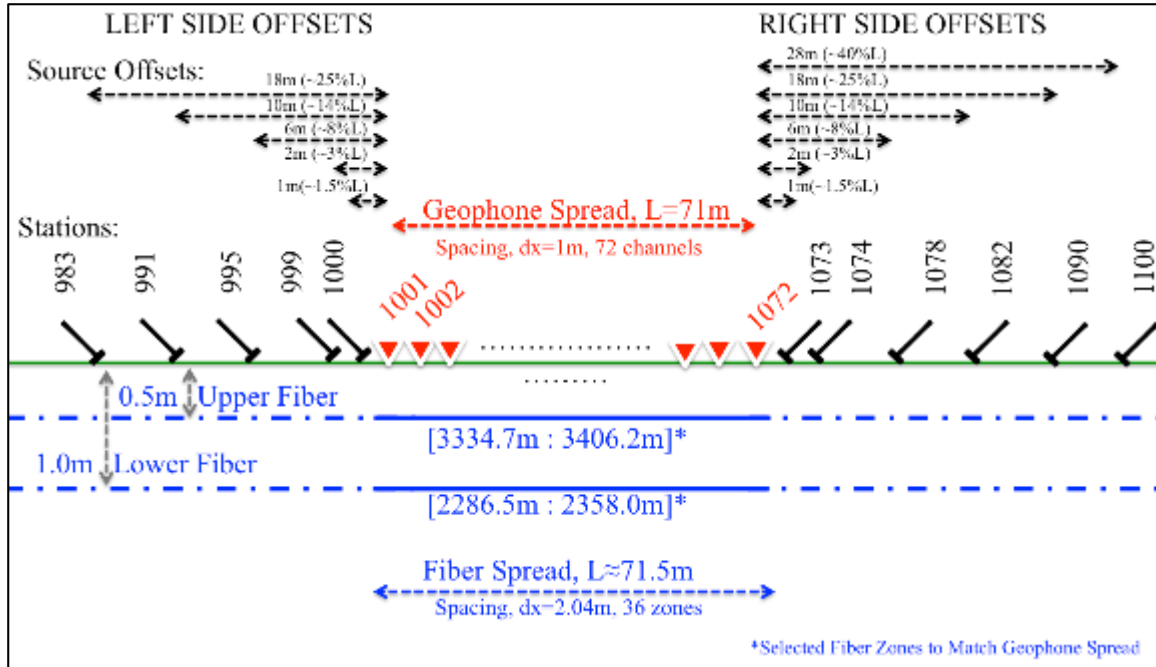
Figure 3.8   Schematic of experimental setup for MASW survey with surface vertical geophones and FOS at depths of 0.5 m and 1.0 m.

Notes:
(1) A metric stationing system was established referencing the leftmost surface vertical geophone at station 1001. Relative locations of geophones, FOS zones, and seismic source offset made use of this reference.
(2) FOS zones corresponding to the extent of the geophone spread were used. The meter marking of the fiber optic cables corresponding to these FOS zones are shown. The difference in meter marking was about 1048 m. The speed of light within the fiber is given by the speed of light in a vacuum (i.e., approx. 0.3 m/ns) divided by the index of refraction (approx. 1.5), resulting in about 0.2 m/ns. The time interval that takes the light pulse to travel from the first meter marking of the FOS at 1.0 m to the first meter marker of the FOS at 0.5 m can be determined by diving the respective distance by the speed of the light pulse. This results in 5240 ns, or about 0.005 ms. Since the data was recorded every 0.2 ms, the time interval to travel the distance of cable corresponded to about 2.5% of the sampling interval. Therefore, the FOS at the two different depths could adequately measure the same seismic response from the shot records.

3.5   Assumptions

The current study used the following assumptions as basis of its investigation.

1. Rayleigh surface waves are expected to predominate from the surface down to the installation depths of the FOS (i.e., up to 1 m deep). It was expected that these would be captured in the signals of both sensor types.

2. Strains occurring in the ground as a result of the impulsive source are directly transferred into the FOS as longitudinal strains in the optical fiber. These longitudinal strains correspond to a change in length of optical path of the fiber. The optical interrogator interprets the change in length as an optical phase change. Hence, the measured optical phase change will correspond to longitudinal ground strains.

3. Signals received from the optical interrogator are processed as received, in units of optical phase, or radians. The optical phase is proportional to the elongation of the fiber as shown in Equation (2.18). This equation, however, was developed for a single optical fiber not placed inside a protective cable. The fiber optic cable used in this study has a protective armor and additional coatings. To account for these, additional calibration is required to find a proportionality factor to convert optical phase to absolute strain. Since this study makes use of the strain proportional optical phase to assess motion and the MASW method performs amplitude normalization (as shown in the integral transformation in Equation (2.15)), it was considered unnecessary to have absolute strain amplitudes; thus justifying the use of the original output units.

67

4. Costley et al. (2015) investigated the coherency between the signals of FOS and geophones to a sledgehammer seismic source from tests performed at a predominantly sandy site. The FOS was found to have acceptable coherency to the seismic source between a frequency range between 20 and 120 Hz. The geophones had a stronger coherence than the FOS, and this occurred at the 20 to 100 Hz frequency range. For the current study, it is assumed that the geophones and FOS will respond coherently to the propagating seismic disturbances.

5. It is assumed that the effective (i.e., measured) phase velocities collected during this study coincide with the phase velocities of the fundamental mode (M0).

CHAPTER IV

FIELD EXPERIMENTS ANALYSIS AND RESULTS

4.1   Data Collection

MASW field data was collected with surface vertical geophones and buried FOS during the day of 17 March 2015. The weather was mostly clear during the time of testing. Temperatures were around 75°F. Subsequently, MASW analysis of the data from the geophones and FOS was conducted and results of the analysis were compared.

A seismic cone penetrometer test (SCPT) was later performed for ground truth verification. The test was conducted during the day of 08 April 2015. Weather was clear during testing. Temperatures ranged between 70°F and 75°F. A shear wave velocity profile was generated from the SCPT test. This was further compared with the previously determined V_S profiles from the MASW analysis using the geophones and FOS.

4.2   Test Matrix

A matrix of tests was measured simultaneously with the vertical geophones at the surface and the FOS at 0.5 m and 1.0 m. Three shot records were performed at 11 locations (shown in Figure 3.8) for a total of 33 shot records. From these, 15 shot records were from source offsets to the left side of the spread and 18 shot records were from source offsets to the right side of the spread. These are referred to as left side offsets

and right side offsets. The respective stations of the seismic source location relate to those shown in Figure 3.8 and are summarized in Table 4.1.

Table 4.1   Test matrix summary measured simultaneously with vertical geophones at the surface, and FOS at depths of 0.5 m and 1.0 m.

Source Offset	%L	Left Source Offset Location (# Shot Records)	Right Source Offset Location (# Shot Records)	Shot Record Number (Test Number)
1m	≈1.5%L	1000 (3)		2028-2030
			1073 (3)	2070-2072
2m	≈3%L	999 (3)		2025-2027
			1074 (3)	2073-2075
6m	≈8%L	995 (3)		2013-2015
			1078 (3)	2076-2078
10m	≈14%L	991 (3)		2010-2012
			1082 (3)	2079-2081
18m	≈25%L	983 (3)		2001-2003
			1090 (3)	2088-2090
28m	≈40%L	*		*
			1110 (3)	2091-2093
Total Number of Shot Records:		**15**	**18**	
		33		

*Source offsets beyond 18 m to the left side of the spread were not possible due to obstruction from the presence of a culvert

These tests generated a total of 99 seismic data files: 33 for the surface vertical geophones, 33 for the FOS at 0.5 m, and 33 for the FOS at 1.0 m. These data files were then used for the analysis.

4.3   Analysis Procedure for Field Experiment Seismograms

The resulting data files consisted of seismograms for the respective channel locations of the surface vertical geophones and the respective zones of the buried FOS at 0.5 m and 1.0 m. These seismograms were analyzed with the MASW method using Kansas Geologic Survey (KGS) SurfSeis®, a software dedicated to process seismic data for use with the MASW method. Analysis was performed for each sensor using the shot records for each respective seismic source side offset. This helped verify lateral homogeneity and repeatability of the results.

4.3.1   Preprocessing Field Experiment Seismograms

4.3.1.1   File Format Conversion and Filtering of Field Experiment Seismograms

To import data into SurfSeis®, data is required to be in the standard SEG-2 binary format (Pullan, 1990). Data obtained from geophones was already in the required format. FOS data, however, was in the CR3 proprietary format corresponding to Optiphase, Inc. It needed to be converted to SEG-2 format. This was performed using a script created in Matlab® named CR3toSEG2.m, shown in Appendix A.1. A band pass filter from 5 to 100 Hz was used to obtain the frequency range of interest. This frequency range is observed in Figure 4.1 through the Fast Fourier Transform (FFT) of one of the surface vertical geophones. The high pass cutoff of 5 Hz is used to approximate the lowest frequency recorded by the geophones of 4.5 Hz. The low pass cutoff of 100 Hz was used

71

to limit the signal to the frequencies excited by the sledgehammer. The band pass filter

used in this study is shown in Figure 4.2. An example of filtering of a FOS zone is shown

in Figure 4.3. Once data was available in the required format, it was imported into

SurfSeis®.
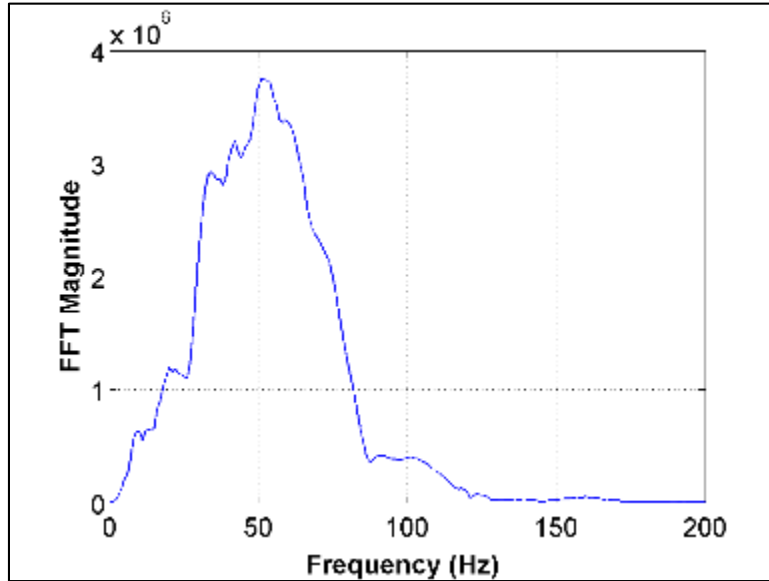
Figure 4.1   FFT response at surface vertical geophone.

Example shown for geophone located at Station 1001 resulting from sledgehammer at
1 m left source offset from Test 2028.
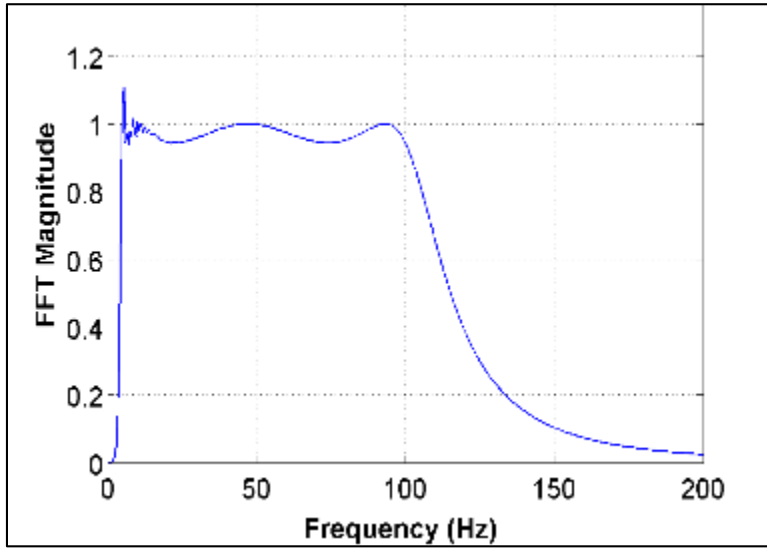
Figure 4.2　　Frequency response of band pass filter used in the preprocessing.
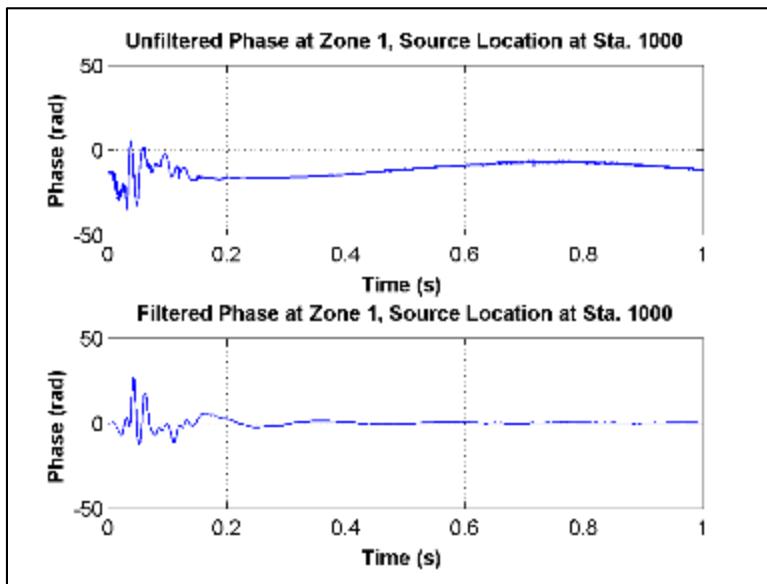
Figure 4.3　　Results from band pass filtering from 5 to 100 Hz.

Example shown for the 0.5 m FOS zone 1 (at Station 1001) resulting from sledgehammer at 1-m offset for Test 2028.

4.3.1.2   Installation Geometry Assignment of Field Experiment Seismograms

The next step involved defining the installation geometry. This consisted of specifying the location of the receivers (i.e., geophone channels or FOS zones) and seismic source. These locations were specified based on the metric stationing referenced in Figure 3.8.

4.3.1.3   Stacking Shot Records from Field Experiment Seismograms

The three replicate shot records at each seismic source location contained the same installation geometry. The responses for each set of replicate shots were similar for each type of sensor. This resulted from having been initiated by the sledgehammer trigger; differences occurred in signal amplitude and noise. Seismic amplitudes imparted by the sledgehammer impact were observed in seismograms of all different sensors. The main seismic energy amplitudes are demonstrated with dashed polygons in the trace seismograms for the different sensors in Figures 4.4 through 4.6.
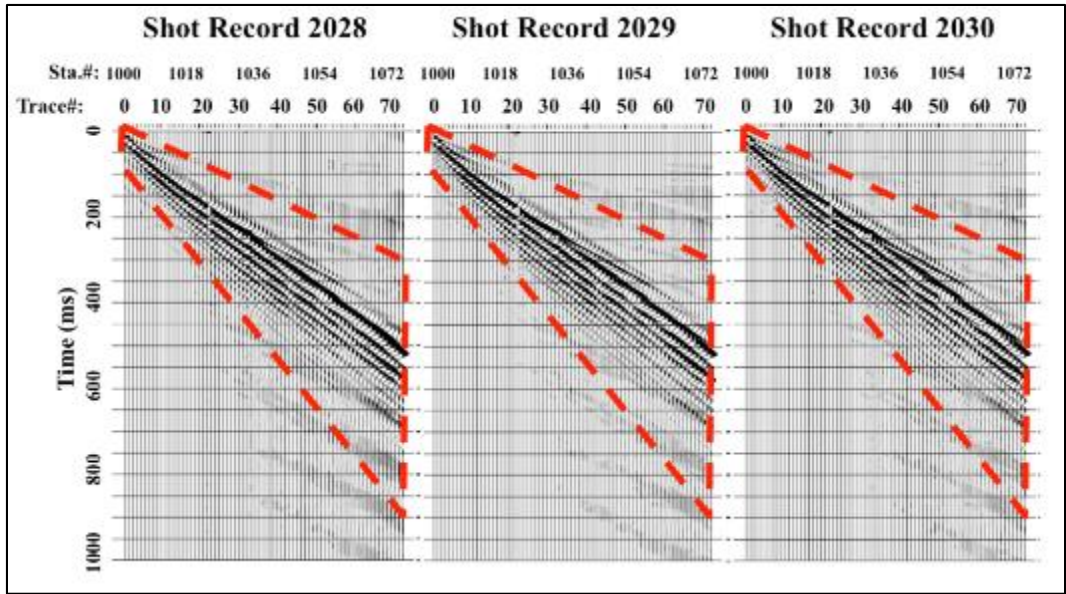
Figure 4.4   Replicate shot records from surface vertical geophones.

Three shot records measured with surface vertical geophones were produced using a sledgehammer at 1-meter offset. Similarities in Rayleigh wave amplitudes in main seismic energy amplitudes are show with dashed polygons.
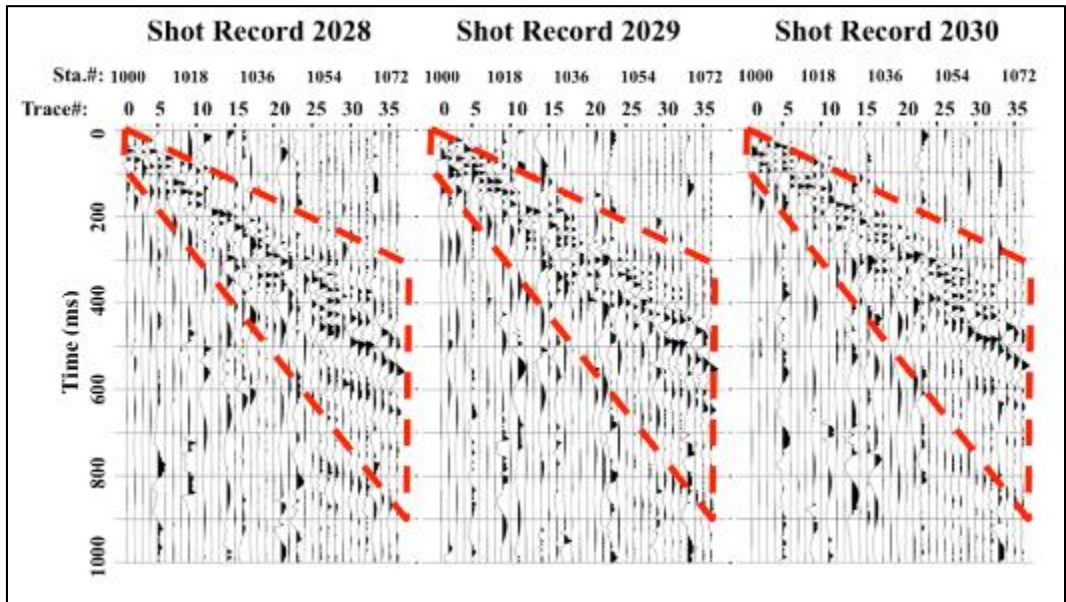
Figure 4.5   Replicate shot records from FOS at 0.5-m depth.

Three shot records measured with FOS at depth of 0.5-m were produced using a sledgehammer at 1-meter offset. Similarities in Rayleigh wave amplitudes in main seismic energy amplitudes are show with dashed polygons.

75
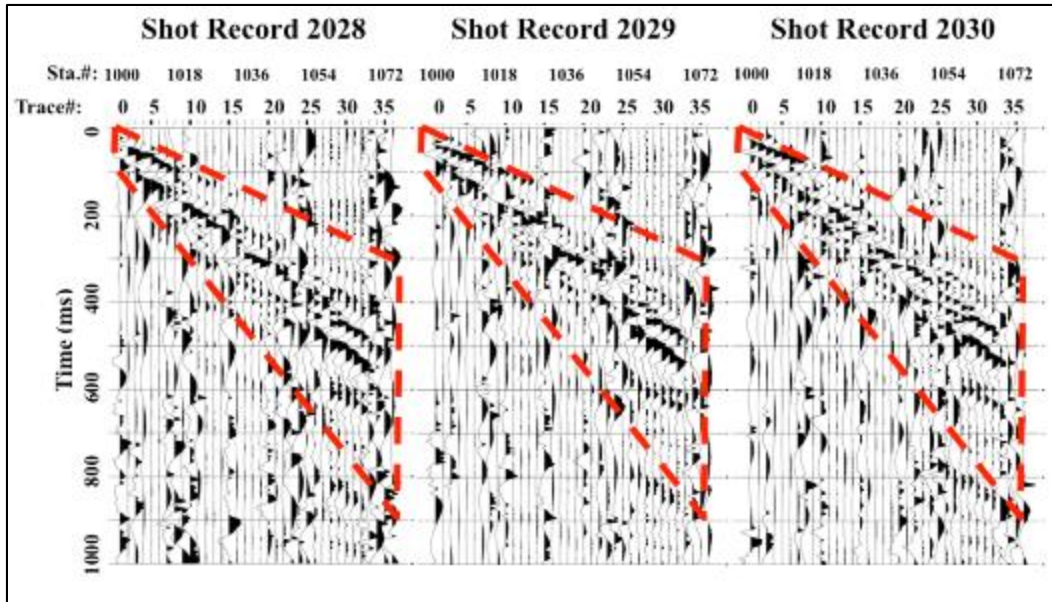
Figure 4.6   Replicate shot records from FOS at 1.0-m depth.

Three shot records measured with FOS at depth of 1.0-m were produced using a sledgehammer at 1-meter offset. Similarities in Rayleigh wave amplitudes in main seismic energy amplitudes are show with dashed polygons.

The replicate seismograms were subsequently combined using SurfSeis® to increase signal to noise ratio and attenuate incoherent noise resulting from the environment and sensor measurements. This was performed by summing the respective traces from each shot record on the same time scale in a process called stacking. An example of stacking of seismograms is shown in Figure 4.7.

76
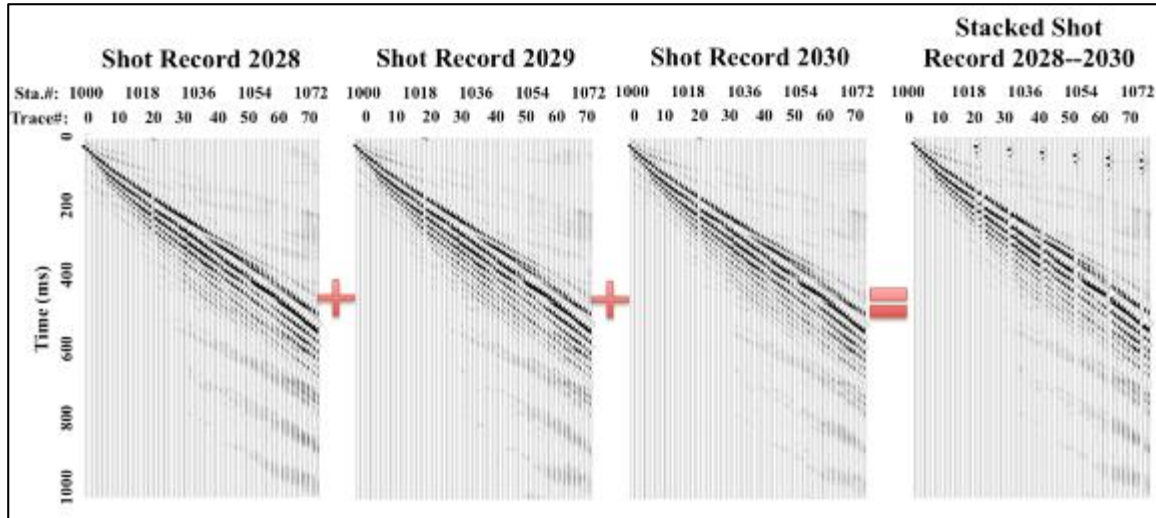
Figure 4.7   Example of three replicate records summed into a single stacked record.

4.3.2   Dispersion Analysis from Field Experiment Seismograms

4.3.2.1   Individual Dispersive Imaging from Field Experiment Seismograms

With the resulting summed stacked seismograms, the coherency patterns of the propagating velocities of each constituent measurement were used to calculate the variation of phase velocities as a function of frequency, i.e., dispersive imaging. This was performed in SurfSeis® as discussed in section 2.2.2.3.1 using the *phase-shift* method by scanning through different phase velocities over the desired frequency of interest. For this study scanning was performed for phase velocities ranging from 50 to 1000 m/sec in 1-m/sec increments over a selected frequency range of 5 to 100 Hz in 0.01-Hz increments. These ranges were considered to cover the expected phase velocities (corresponding to the expected shear wave velocities) and the depths of investigation. The scheme used by this method was summarized in Figure 2.22. An example of the resulting dispersive imaging is shown in Figure 4.8.

77
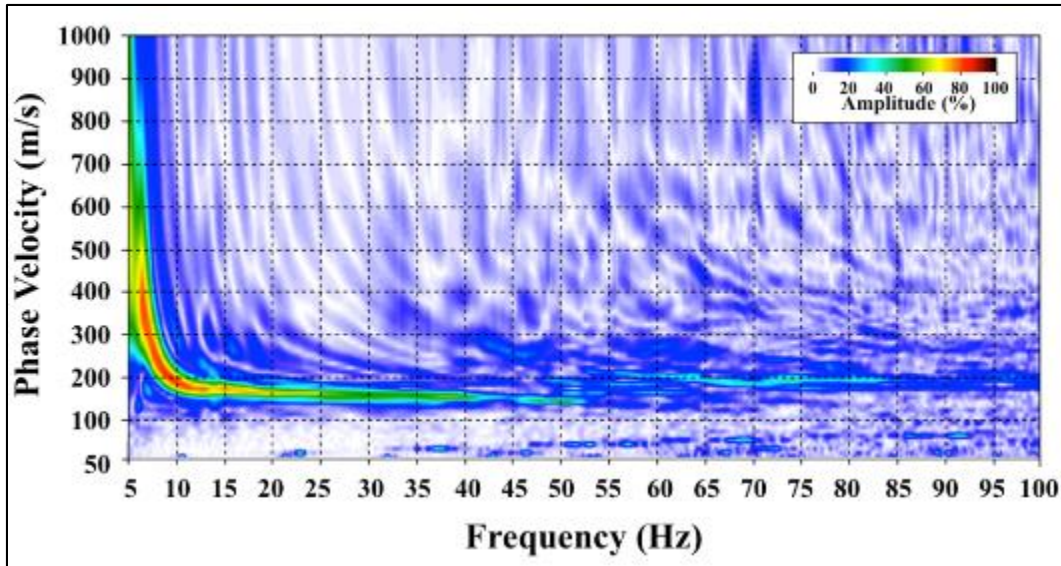
Figure 4.8   Example of dispersive image from vertical geophones.

Obtained using the stacked surface vertical geophone seismograms from Tests 2001-2003 with the left source offset at 18 m.

4.3.2.2   Combined Dispersive Imaging from Field Experiment Seismograms

In MASW analysis, the investigated subsurface profile represents the average properties at the mid-station (or center location) of the receiver spread. Receiver locations were maintained constant during testing and thus contained the same mid-station. This justified the combination of individual dispersive images into one representative image of seismic source side (i.e., left side or right side) for each sensor. The combination of dispersive images was achieved by scanning through the range of frequencies and summing the respective normalized phase velocity amplitudes of individual dispersive images. The resulting combined dispersive image captures the energy imparted by the different seismic source offsets and allows for a better representation of the fundamental Rayleigh-mode, M0. Figure 4.9 shows how the combined dispersive image takes advantage of the response captured by the individual dispersive images at different source

offsets. By adding together the respective amplitudes from different source offsets, the

lower frequencies as well as the higher frequencies are better represented allowing for a

more defined M0 dispersive curve.
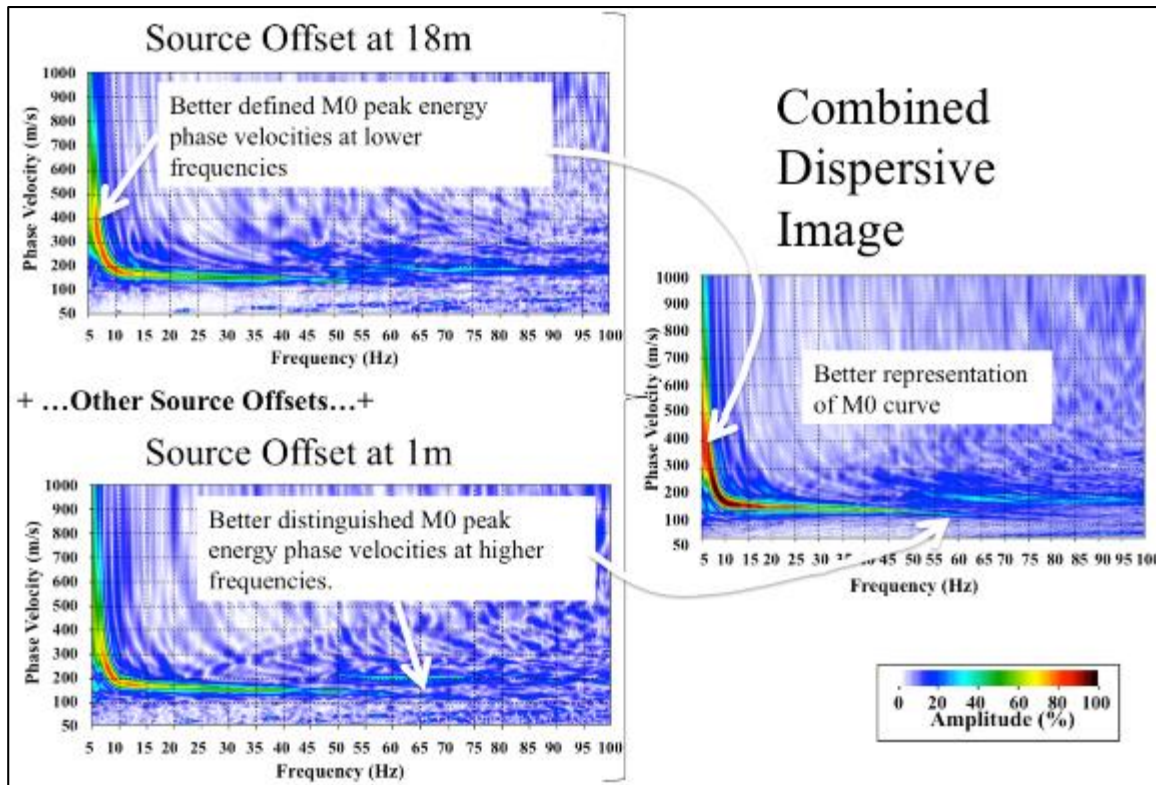
Figure 4.9   Example of a combined dispersive image from the individual dispersive images.

Using tests performed with surface vertical geophones from left side seismic source offsets.

4.3.2.3   Dispersion Curve Selection from Field Experiment Seismograms

Using the combined dispersive images, qualitative interpretation was applied to

select discrete points of peak fundamental-mode phase velocity amplitude over different

frequencies and obtain a dispersion curve. An example is shown in Figure 4.10. Selection

of these points was based on phase velocity amplitude energy of above 50%. It was

79

decided that, at a minimum, 15 points were to be selected. In many instances, however, more points were needed to better define the curvature representing the dispersion curves. Other considerations for interpretation of the dispersion curves included: (1) avoiding frequencies gaps greater than 5 Hz over which the M0 dispersion curve could not be interpreted with high confidence, and (2) avoiding locations of possible higher mode contamination of the fundamental mode (M0). An example of these considerations is shown in Figure 4.11.

Data from geophones and FOS were treated independently. Interpretation of the fundamental mode for each respective sensor was performed with no consideration of the dispersion curve selection of other sensors (and other source offset side) to reduce data manipulation.

Influences on higher modes were noted in the dispersive images. However, since the MASW, on which this study concentrates, focuses on determination of the fundamental modes of Rayleigh waves, only the M0 dispersion curve was used for analysis.
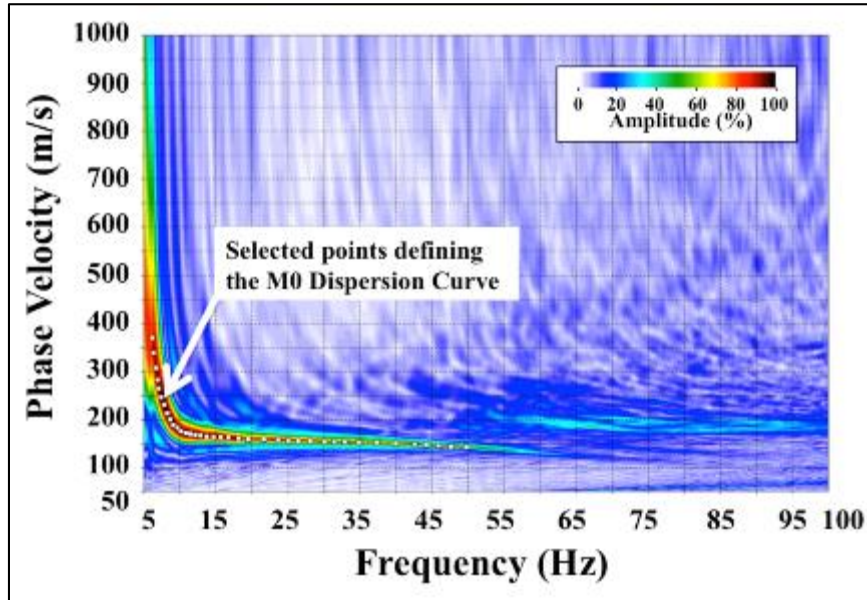
Figure 4.10   Well-defined M0 qualitative dispersion curve interpretation.

Using combined dispersive image for tests performed using surface vertical geophones from left source offsets.
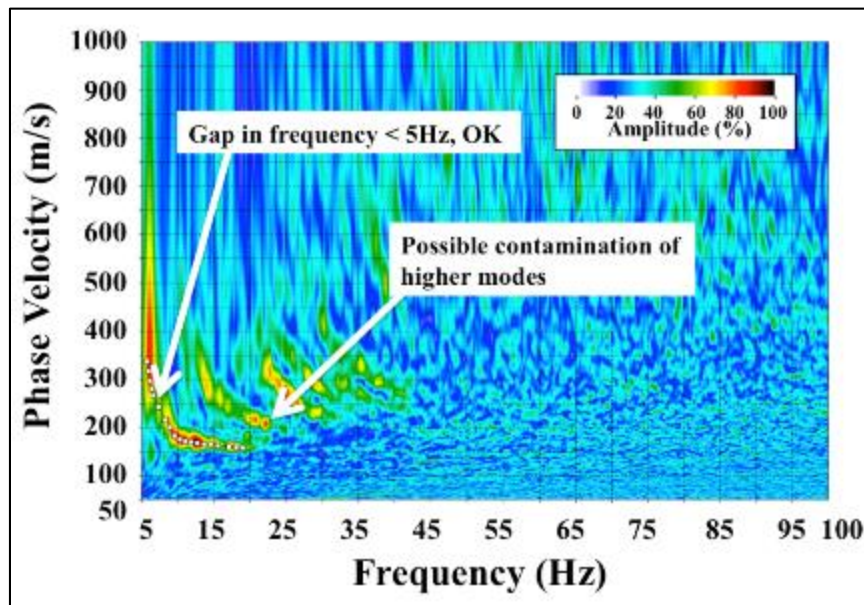
Figure 4.11   Considerations for qualitative dispersion curve interpretation when higher modes and gaps were observed.

Using combined dispersive image for tests performed using 1.0 m deep FOS from left source offsets.

4.3.3   Inversion Analysis from Field Experiment Seismograms

The resulting dispersion curves were then used for inversion (back-calculation) to obtain 1-D V_S profiles with depth for the different sensors. This was performed in SurfSeis® as discussed in section 2.2.2.3.2 making use of a simplified least squares approach using an iterative solution with the Levenberg–Marquardt and singular-value decomposition techniques. In essence, the experimentally obtained dispersion curve is compared to a theoretically calculated dispersion curve found using assumed subsurface properties. Using an initial model with assumed material properties shown in Table 4.2, a theoretical forward dispersion curve was used to compare to the measured dispersion curve. The theoretical dispersion curve is calculated from a forward model of Rayleigh wave propagation that contains the four unknowns in the inversion problem, which are: layer thickness (h), density (ρ), S-wave velocity (V_S) and Poisson's ratio (υ). Each of these parameters has different contributions to the dispersion curve calculations, however, the influence of Poisson's ratio and density are considered negligible. These can be estimated based on past experience without affecting the final results of the inversion (Foti, 2000).

Due to unknown the variability of the expected soil deposits with depth, a constant value of Poisson's ratio of 0.3 was chosen. This value covers the range of Poisson's ratio for loess of 0.1 to 0.3 (Bowles, 1995), while covering other typical ranges for silts and sands, which vary from 0.2 to 0.4 (Holt and Kovacs, 1981). Although this value might be considered low for saturated clay soils, which can range from 0.4 to 0.5 (Holt and Kovacs, 1981), it was considered justifiable due to negligible effect of Poisson's ratio on the inversion process (Foti, 2000).

82

A constant density with depth of 1.55 g/cm^3 was used for the inversion model. This value was selected to represent the range of values of 1.27 to 1.67 g/cm^3 for loess referenced by Murphy & Albertson, 1996), while also tries to account for other types of soils whose range can vary from about 1.2 g/cm^3 in dry densities to about 2.4 g/cm^3 in wet densities (Holt and Kovacs, 1981). This constant value was justified due to the unknown elevation of the water table (to distinguish between wet and dry densities), unknown subsurface variability to where densities will change, and negligible effect of density on the inversion process (Xia et al., 1999; Foti, 2000).

The initial model consisted of ten layers with variable thickness. Ten layers were considered adequate for vertical resolution as well as numerical stability. A lower number of layers will trade-off vertical resolution, while a larger number will add greater uncertainty in the inverted values (Xia et al., 1999). The variable thickness of the layers is made to accommodate layers to the dispersion curves curvature. The corresponding thickness of layers was adjusted based on the wavelength scaling as a function of frequency as outlined in Equation (2.16). To project the maximum depth of investigation, a depth to wavelength ratio (Z_{MAX}/λ_{MAX}) of 0.35 was used. This ratio followed the conservative end of the range defined in the relationship of Equation (2.8). The maximum wavelength, λ_{MAX}, was solved for using Equation (2.6), with inputs of phase velocity at the lowest frequency defined in the dispersion curve and its corresponding frequency.

Estimates of shear wave velocities for the initial model were found multiplying the average phase velocity over each layer by a factor of 1.08. The value of 1.08 was determined from Equation (2.5) using the selected Poisson's ratio of about 0.3.

83

Table 4.2   Initial Model Parameters Used for Inversion Analysis from Field
            Experiment Seismograms

Material Property	Values considered for analysis
Layer Thickness (h)	Depth is scaled using the corresponding wavelengths as a function of frequency as shown in Equation (3.13). Layers are adjusted by the rate of change of values picked in the dispersion curve.
Density (ρ)	1.55 g/cm^3
Poisson's Ratio (υ)	0.3
Shear Wave Velocity (V_S)	Initial estimate is based on average dispersion curve phase velocities corresponding to each layer as 1.08 V_R

Through the inversion process, only V_S was updated iteratively to obtain a new forward theoretical dispersion curve until an acceptable fit to the measured dispersion curve was achieved. Stopping criteria considered for an acceptable fit included a root mean square error (RMSE) in phase velocity of 5.0 m/sec and a maximum of 10 iterations. These values were considered appropriate, as smaller RMSE values yielded similar results and the iterations never reached the specified maximum number of iterations. The final V_S values were considered to be the 1-D V_S profile of the site. An overview of the analysis procedure is presented as a flowchart in Figure 4.12.
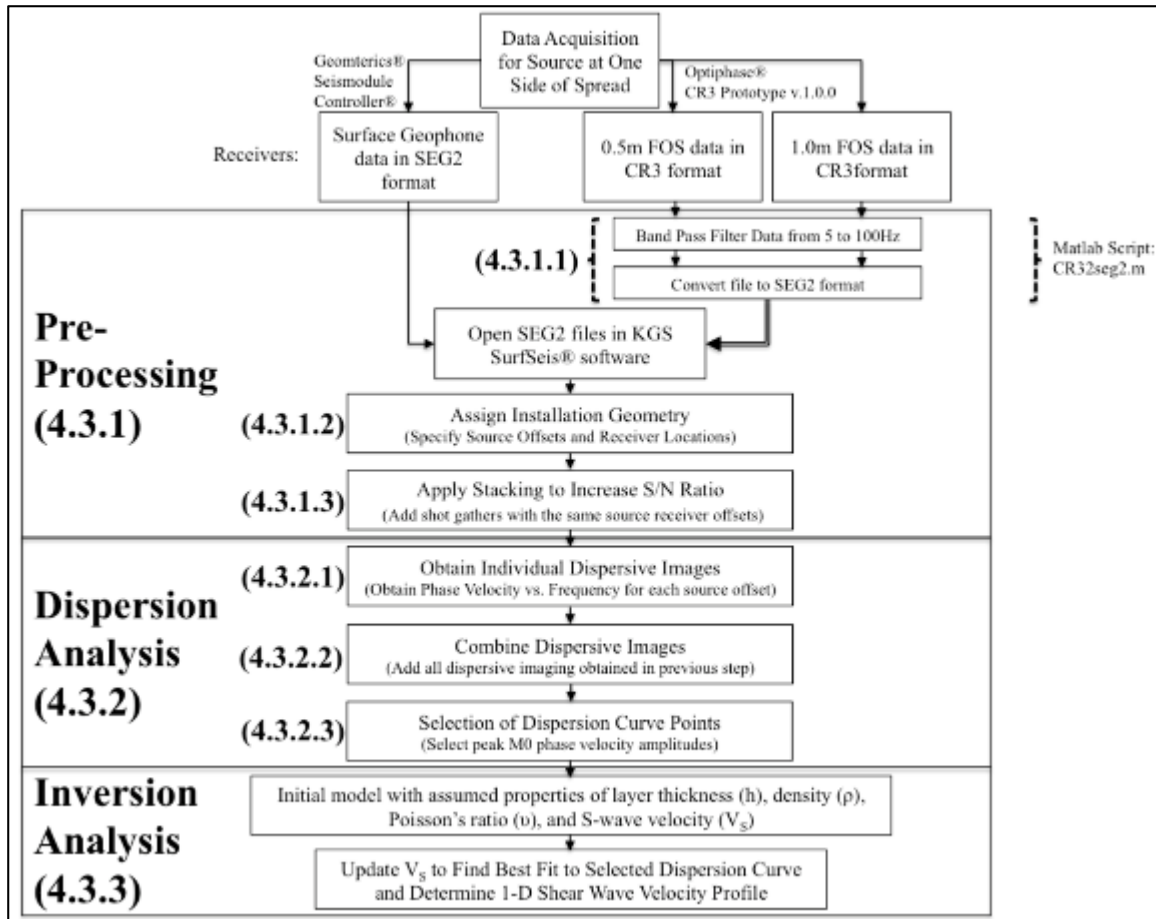
Figure 4.12   MASW procedure to obtain 1-D S-wave velocity profile from field
experiment seismograms.

4.4   Field Experiment Seismogram Results

4.4.1   Stacked Field Experiment Seismograms

Seismic signals were recorded with vertical geophones mounted at the ground

surface and FOS buried at depths of 0.5 m and 1.0 m. The time domain signals for the

different geophone channels and FOS zones were obtained for each individual shot

record and represented as digital seismograms. Resulting seismograms were stacked (i.e.,

summed) for each seismic source-offset distance to improve signal-to-noise ratio. The

resulting stacked seismograms from the surface vertical geophones, FOS at depth of

0.5 m, and FOS at depth of 1.0 m are shown respectively in Figures 4.13 through 4.15 for

the seismic source to the left side of the spread. Figure 4.16 through 4.18 show the

stacked seismograms for the same sensors using the seismic source to the right side of the

spread.

The signals obtained with the FOS (shown in Figures 4.14, 4.15, 4.17, and 4.18)

exhibited greater noise than the signals obtained with the surface vertical geophones

(shown in Figures 4.13 and 4.16). A likely source of noise is referred to as fading, which

occurs when the backscattered light from a zone end is low and the receiver does not

have sufficient signal to demodulate. This causes large fluctuations in the output signal.

Although the amount of noise in the data was evident, seismograms were used "as is" for

MASW analysis. This is justified by the fact that incoherent noise between traces will

cancel.
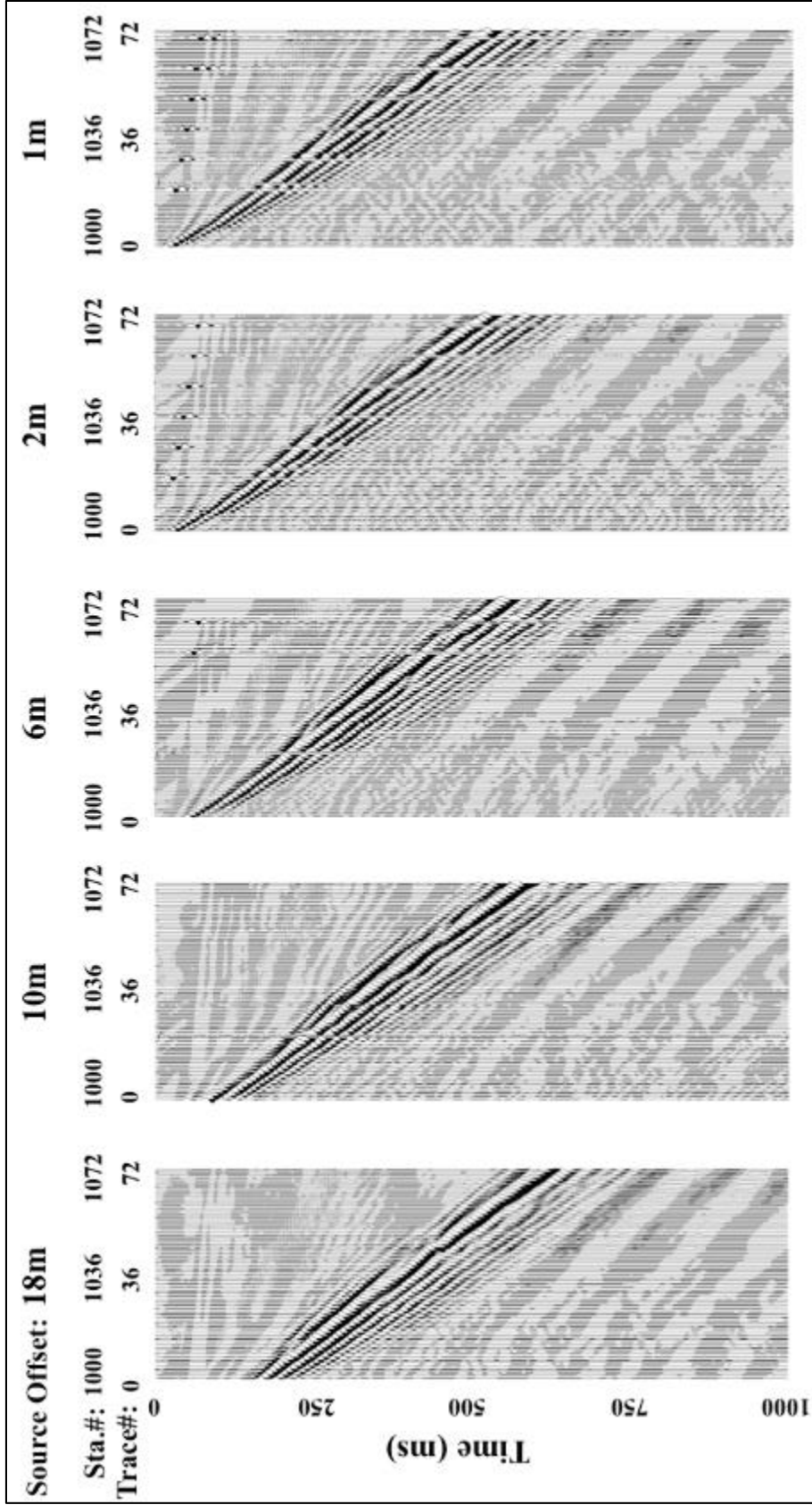
Figure 4.13   Stacked seismograms with normalized trace amplitudes from vertical geophones at the surface for the active source located to the left side of the spread.
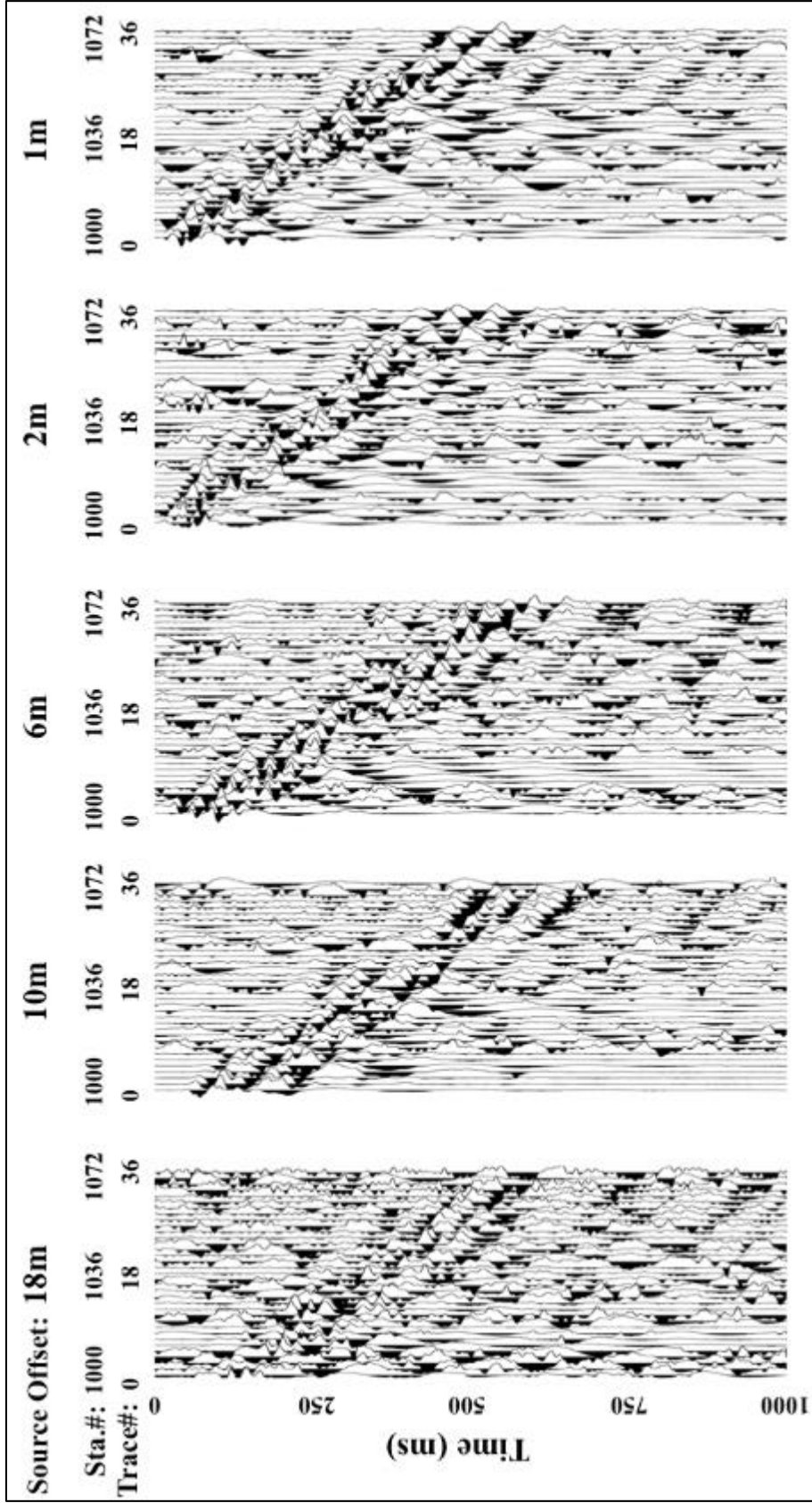
Figure 4.14   Stacked seismograms with normalized trace amplitudes from FOS at depth of 0.5 m for the active source located to the left side of the spread.

88
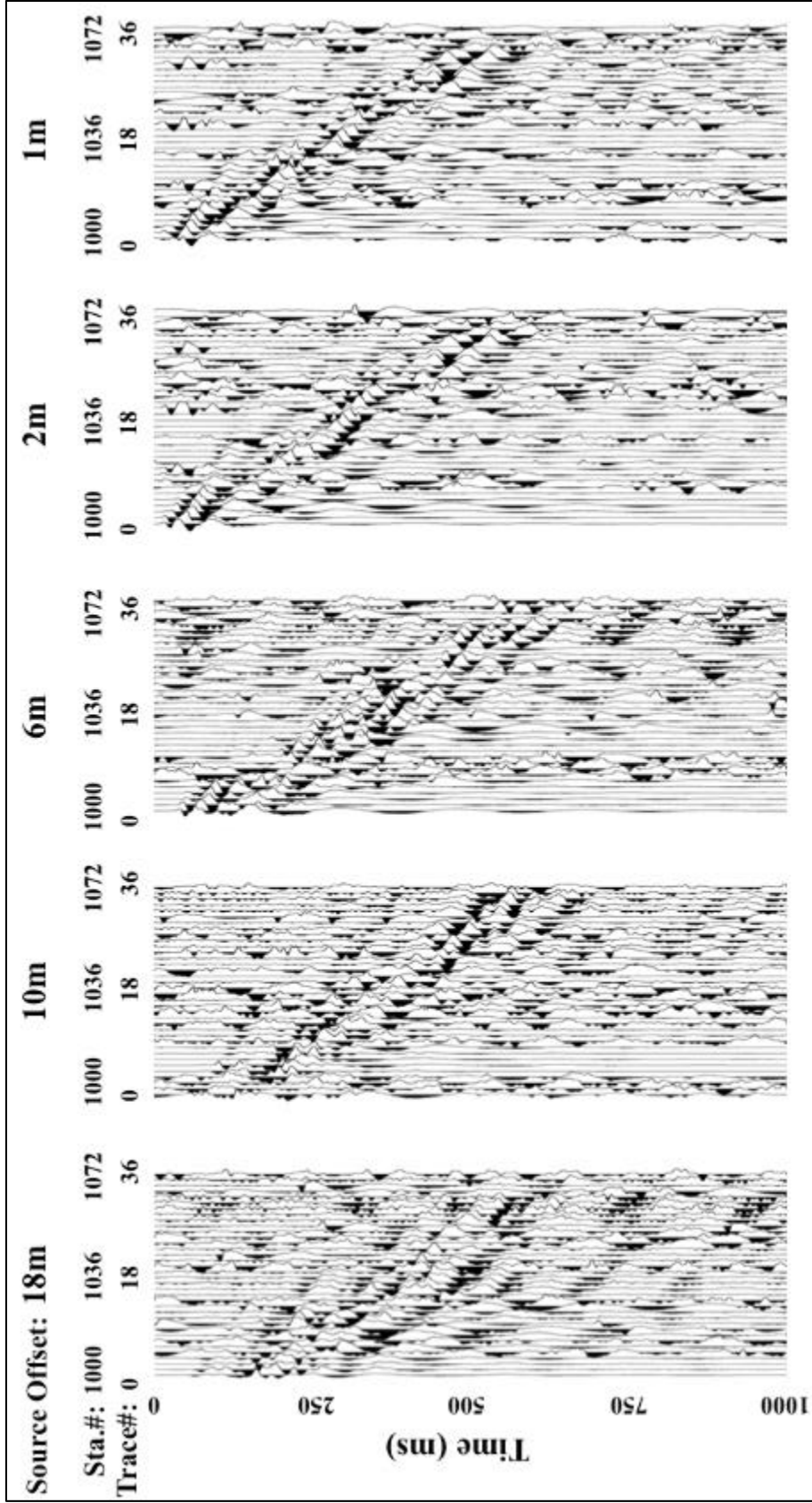
Figure 4.15   Stacked seismograms with normalized trace amplitudes from FOS at depth of 1.0 m for the active source located to the left side of the spread.
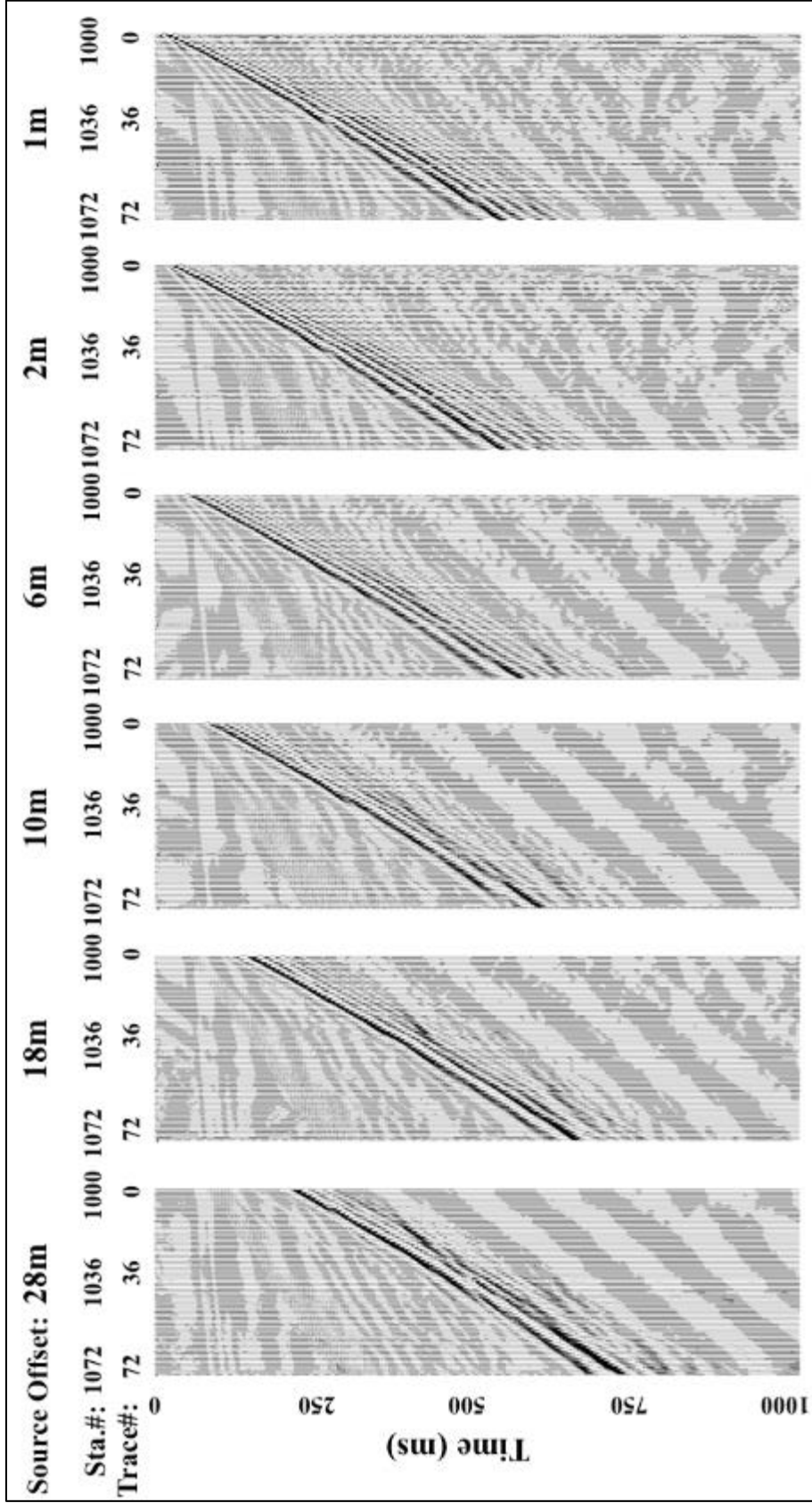
Figure 4.16   Stacked seismograms with normalized trace amplitudes from vertical geophones at the surface for the active source located to the right side of the spread.
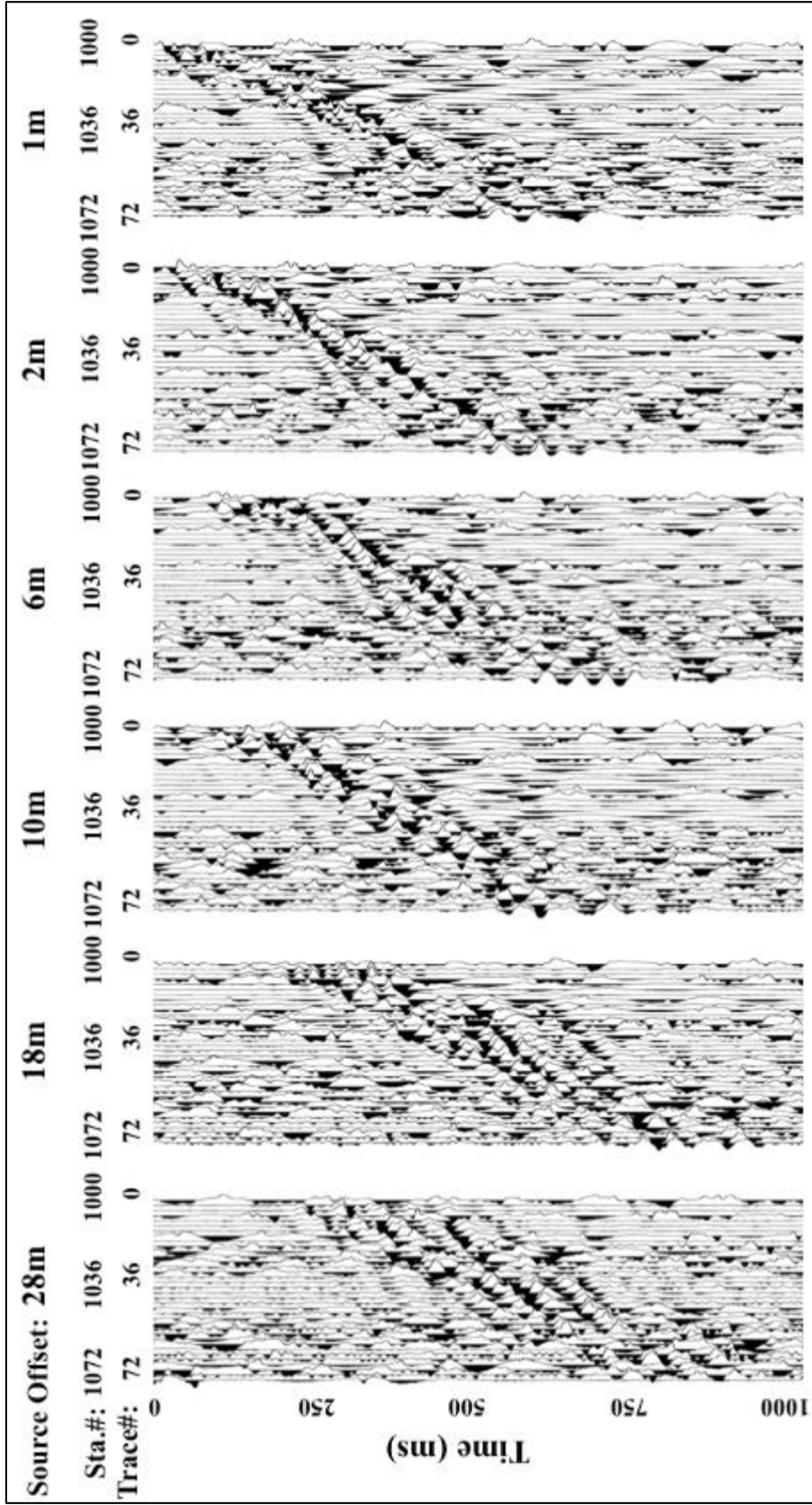
Figure 4.17 Stacked seismograms with normalized trace amplitudes from FOS at depth of 0.5 m for the active source located to the right side of the spread.

91
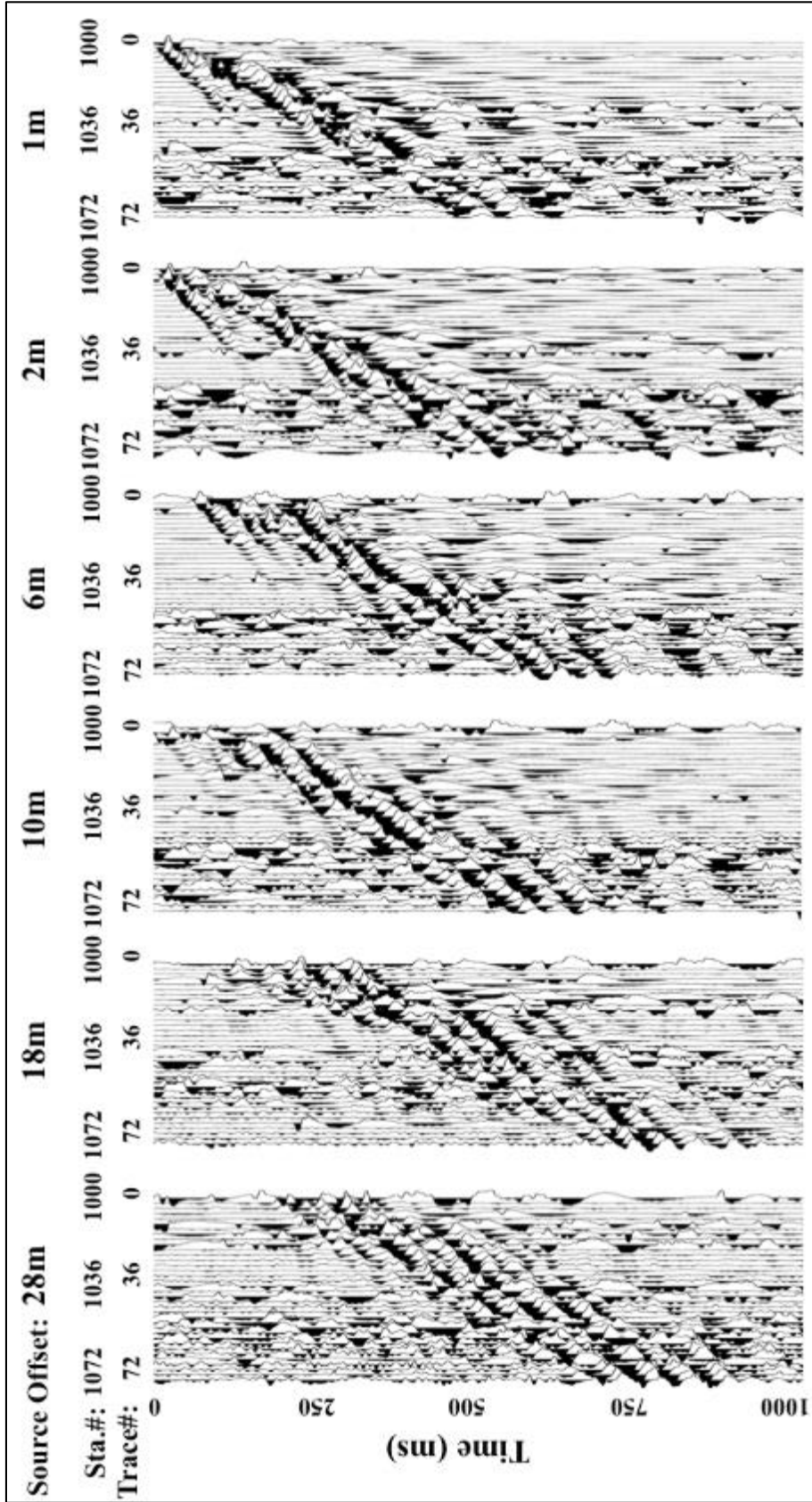
Figure 4.18   Stacked seismograms with normalized trace amplitudes from FOS at depth of 1.0 m for the active source located to the right side of the spread.

4.4.2   Combined Dispersive Imaging Results from Field Experiment Seismograms

Representative combined dispersion images were created with data acquired with

each sensor array for the left and right seismic source side offsets. Results are shown in

Figures 4.19.
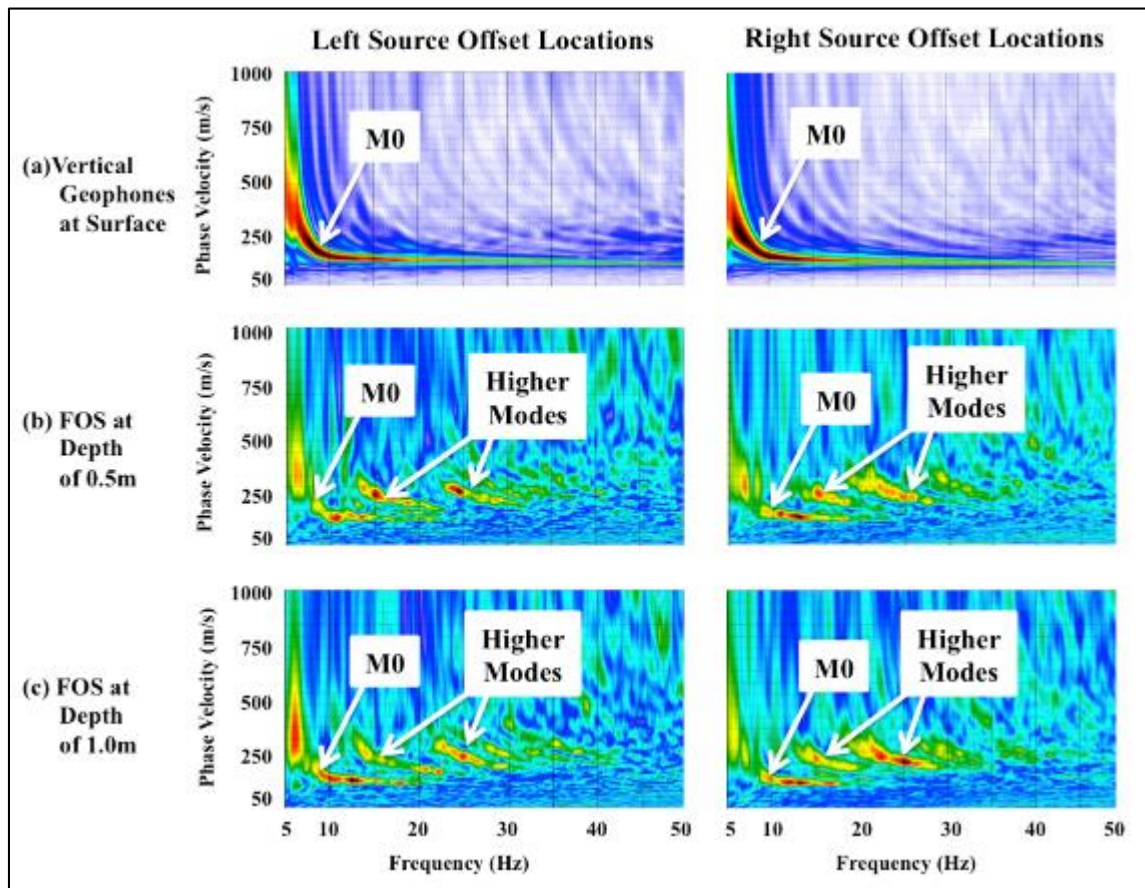
Figure 4.19   Combined dispersive images obtained with the different sensors for the left
and right side seismic source offsets.

Also showing peak amplitudes phase velocities corresponding to R-wave fundamental
mode (M0) and the existence of higher modes. The frequency ranged from 5 to 100 Hz in
the analysis. Figure shows frequencies under 50 Hz to focus on the frequency range were
most of the energy in the FOS signal concentrated.

By visually comparing the results for the seismic source offsets located to the left and right side of the spreads, similarities in the trends of phase velocities as a function of frequency were observed. These similarities suggested that the site was laterally homogeneous and results were reproducible for each sensor.

4.4.3   Dispersion Curve Results from Field Experiment Seismograms

Patterns of the apparent fundamental Rayleigh mode M0, noted in Figure 4.19, were used for dispersion curve interpretation. Discrete points of interpreted peak fundamental-mode phase velocity amplitude over different frequencies were selected to obtain the M0 dispersion curve. The selected dispersion curves are shown in Figure 4.20.
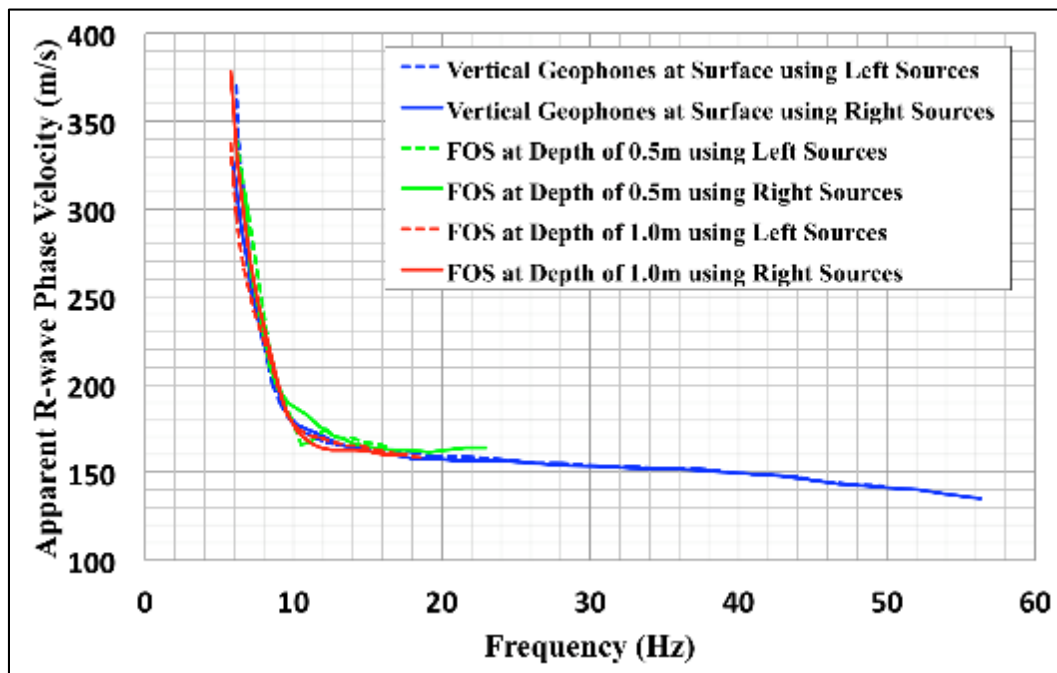
Figure 4.20   Comparison of interpreted dispersion curves from the field experiment seismograms for the different sensors and respective seismic source offset sides.

The frequency range of the dispersion curves govern the wavelengths of the excited Rayleigh waves, and thus the depths to which the shear wave velocities can be estimated. Frequencies, as low as 6 Hz, were perceived with the FOS and geophone arrays. As a result, this allowed the MASW V_S profiles to reach approximately the same depths of investigation.

The M0 dispersion curves obtained using the geophone array extended to higher frequencies than those obtained with the FOS. Higher frequencies are used to determine the V_S at shallower depths. Figure 4.19(a) shows a well-defined M0 for the geophone dispersive images up to frequencies of about 50 Hz. This allowed for easier interpretation of the M0 dispersion curve. The combined dispersive images obtained from the FOS measurements, shown in Figures 4.19(b, c), show separation of M0 at the lower frequencies. At higher frequencies, contamination of higher modes prevented further interpretation of the M0 dispersion curves. The detection of higher modes was likely the result of the sensor depth rather than sensor type. This is further explored through synthetic seismograms in the following chapter. The observed frequencies of the M0 dispersion curves were limited to below 15 to 25 Hz for the FOS at a depth of 0.5 m. The frequencies of the M0 dispersion curve for the FOS at a depth of 1.0 m were limited to below 20 Hz.

Both the geophones and FOS dispersion curves were fairly consistently interpreted as shown in Figure 4.20. One of the main differences in the interpretation of the M0 dispersion curves was the limitation in frequency range in the FOS previously mentioned and minor discrepancies in the selection of points to represent the dispersion curves.

4.4.4 Shear Wave Inversion Results from Field Experiment Seismograms

A least-squares inversion of the selected M0 dispersion curves was applied to estimate 1-D V_S profiles as described in section 4.3.3. Inversion parameters were used consistently for all sensors. The final inverted V_S profiles obtained using the dispersion curves are shown in Figure 4.21.
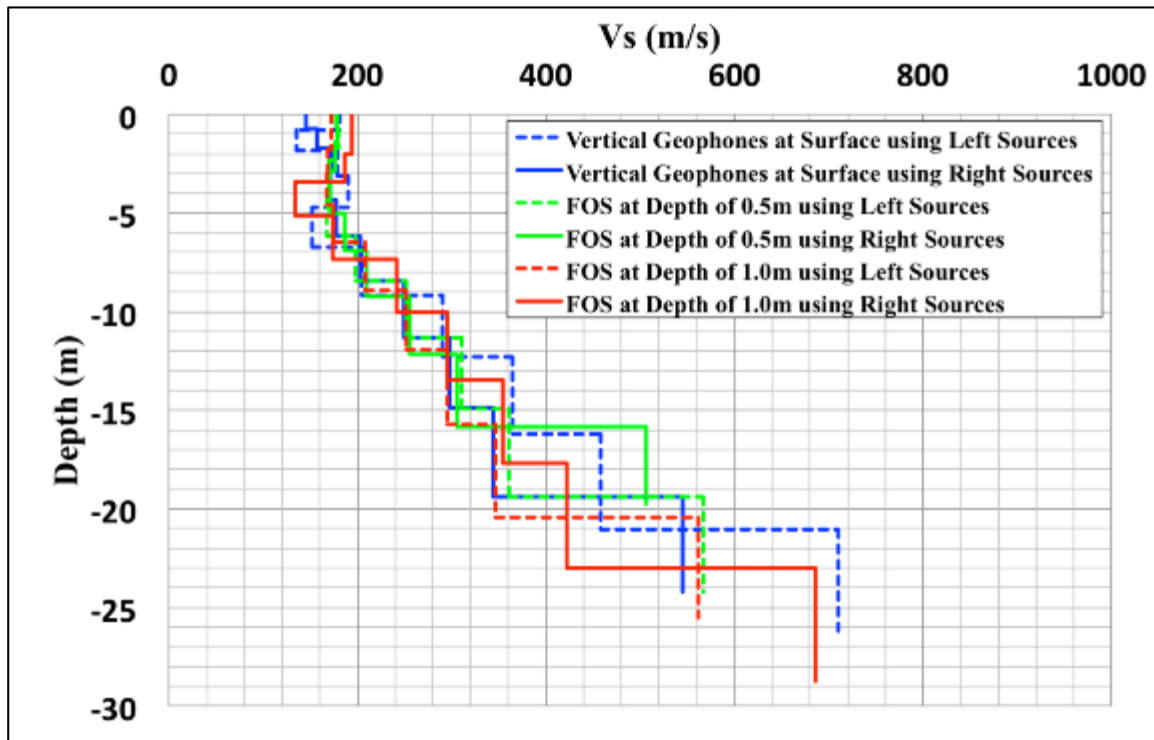
Figure 4.21   Final inverted V_S profiles obtained from the different dispersion curves using the field experiment seismograms.

It was noted that the V_S profile obtained with the different sensors was within the ranges of depth and V_S of the expected geology described in Figure 3.5. Differences in shear wave velocities show the non-uniqueness of the inversion process, where multiple shear wave profiles (and also other changing material properties) can yield similar

dispersion curves. Depths from 24.21 to 26.32 m were obtained using the surface vertical geophones. Depths from 19.78 to 24.21 m were obtained using the FOS at a depth of 0.5 m. Depths from 25.53 to 28.74 m were obtained using the FOS at a depth of 1.0 m. Irrespective of these differences, the shear wave velocities obtained with the FOS at the two different depths were in the same range as those obtained with surface vertical geophones. Depths of investigation up to about 25 m were achieved during the inversion using the MASW analysis. This depth is about the expected depth of the Glendstone Limestone considered to define the depth of interest, as previously described in Chapter III.

4.5   Ground Truth Verification using Seismic Cone Penetrometer Test

In order to validate the V_S inversions obtained with the MASW analysis, a Seismic Cone Penetrometer Test (SCPT) was performed at mid length of the sensor installation. The SCPT test was performed about 22 days after the MASW field experiments with the FOS and geophones, due to unavailability of the SCPT equipment. As mentioned in section 2.2.1, the SCPT is a Cone Penetrometer Test (CPT) used in conjunction with down-hole measurements and it is commonly used for V_S profiling due to its cost effectiveness and fast data acquisition. Furthermore, since this method is invasive, direct measurements are made and it does not suffer from the non-uniqueness of the inversion solution. The experiment followed the ASTM D 7400-14: Standard Test Methods for Downhole Seismic Testing.

The SCPT setup involved the CPT cone and push rod normally pushed into the ground and a steel shear beam pressed onto the ground using the CPT vehicle weight. These are shown in Figure 4.22. Two horizontal geophones located inside the push rod

were used for measurements. A sledgehammer was used to horizontally strike the end of the steel shear beam and generate a SH-wave. A contact trigger attached to the sledgehammer measured the exact starting time of the hammer strike. One of the two geophones was aligned parallel to the shear beam to record the arrival time of the strike. Care was taken by keeping track of the rod alignment to avoid rotating the geophones as additional rods were added and the cone was pushed further into the ground.
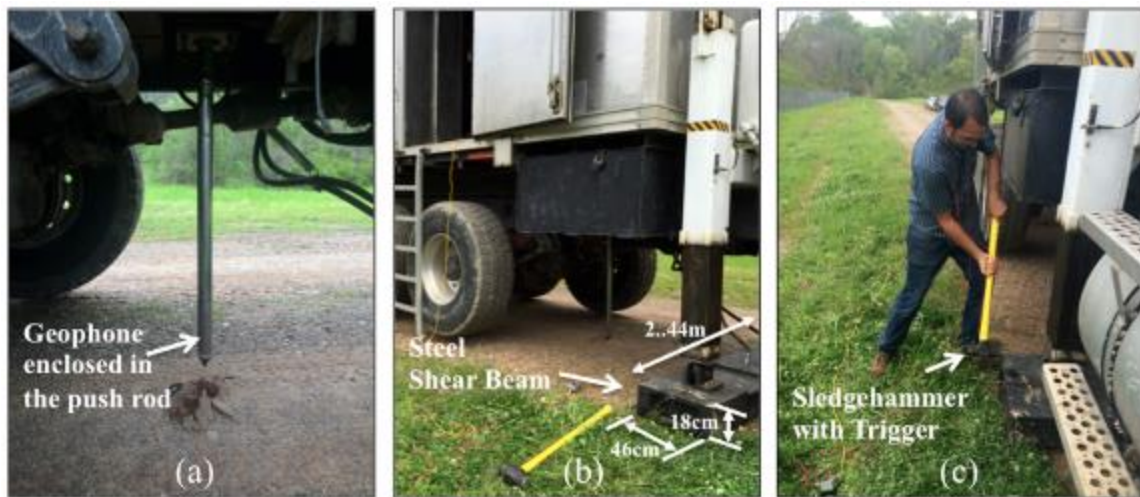
Figure 4.22   Seismic Cone Penetrometer Test (SCPT) setup.

Seismic recordings were performed every approximately 1 m in depth. To do this, the cone rod was pushed down manually about every 1 m and then stopped. When stopped, a hammer strike was performed on the shear beam. Amplitude and times of arrival were recorded at the geophone for each depth location. The average shear wave velocity was calculated for each given depth interval as (ASTM D7400-14):

$$V_S = \frac{L_2 - L_1}{\Delta T_{R2-R1}},$$
(4.1)

98

as shown in Figure 4.23, L_1 and L_2 are the respective straight-line distances. Generalized at increasing depths of the CPT geophones, the hypotenuse, L_i, is given by:

$$L_i = \sqrt{D_i^2 + X_{distance\ to\ source}^2} \qquad (4.2)$$

and ΔT_{R2-R1} is the difference in arrival times of the measured shear waves at the increasing depths. The distance from the shear beam producing the SH source to the location of the cone, $X_{distance\ to\ source}$, was 2 m. Straight-line distances were found using this offset. A schematic of this procedure is shown in Figure 4.23.
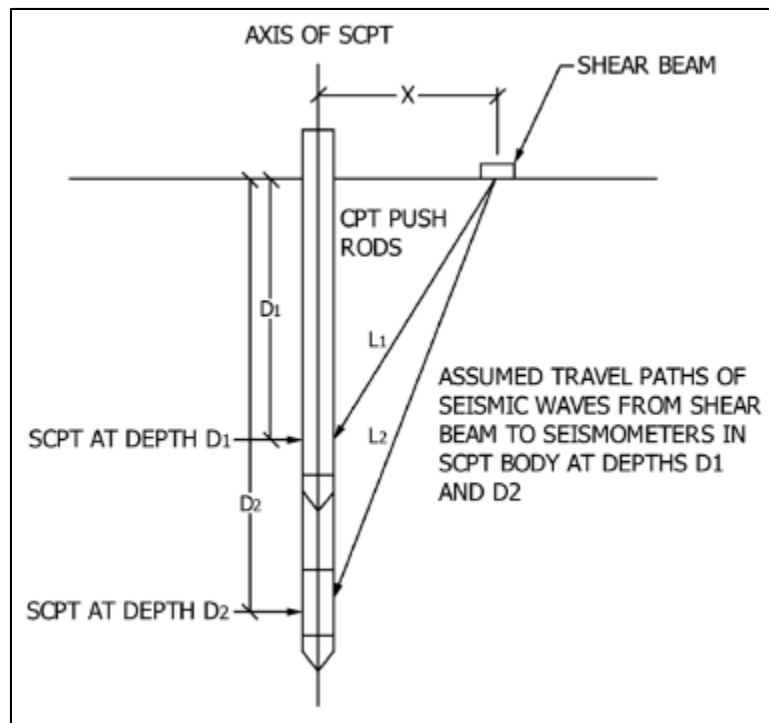
Figure 4.23   Methodology to obtain Vs using SCPT.

(Taken from ASTM D7400-14)

During the SCPT field tests, cone rod penetration with depth was controlled manually and depths were recorded and used to calculate the straight-line distance to the

sensor. At each depth the cone penetrometer was stopped, seismic measurements were made, as shown in Figure 4.24. A total of 21 SCPT records (depths) were collected. Readings were taken from 0.61 m from the ground surface up to a depth of 21.44 m. Although a target depth of 25 m was selected for the SCPT test, greater depths than 21.44 m were not possible due to drilling refusal of the CPT rig. At the depth of 21.44 m, the Glendon Limestone, which is considered first bedrock encountered in borings in the area, may be present and likely prevented advancement to further depths. In addition, the final depth achieved with the SCPT was comparable to depths achieved with the MASW method.

The delay time from the source to the receiver at each depth was interpreted using the first trough point of the recorded wave trains. These are shown as crosses in Figure 4.24. By comparing the delay times between respective depths from the SCPT depth records, the shear wave velocity was estimated using Equation (4.1). Corresponding V_S values are shown in Figure 4.24.

From the SCPT results, a shear wave velocity profile was constructed, as shown in the solid thick black line in Figure 4.25. MASW results shown in Figure 4.21 are also included for comparison.

Depth Record #	Depth (m)	Straight-Line Distance to Sensor (m)	Delay (ms)	V_S (m/s)
1	0.61	2.09	4.69	
2	2.39	3.12	13.12	121.65
3	3.4	3.94	18.12	165.64
4	4.4	4.83	23.28	172.21
5	5.41	5.77	28.44	181.13
6	6.41	6.71	33.67	181.05
7	7.42	7.68	39.29	172.61
8	8.42	8.65	43.98	206.71
9	9.41	9.62	48.67	205.95
10	10.42	10.61	53.20	218.55
11	11.42	11.59	56.48	299.98
12	12.42	12.58	60.31	257.49
13	13.41	13.56	64.84	215.97
14	14.43	14.57	66.71	539.90
15	15.43	15.56	68.12	702.93
16	16.44	16.56	71.17	328.57
17	17.43	17.54	73.04	525.75
18	18.43	18.54	75.39	422.91
19	19.43	19.53	77.96	386.95
20	20.42	20.52	80.15	449.79
21	21.44	21.53	82.34	463.64

Figure 4.24   Depth records obtained using SCPT and calculated V_S with depth.

101
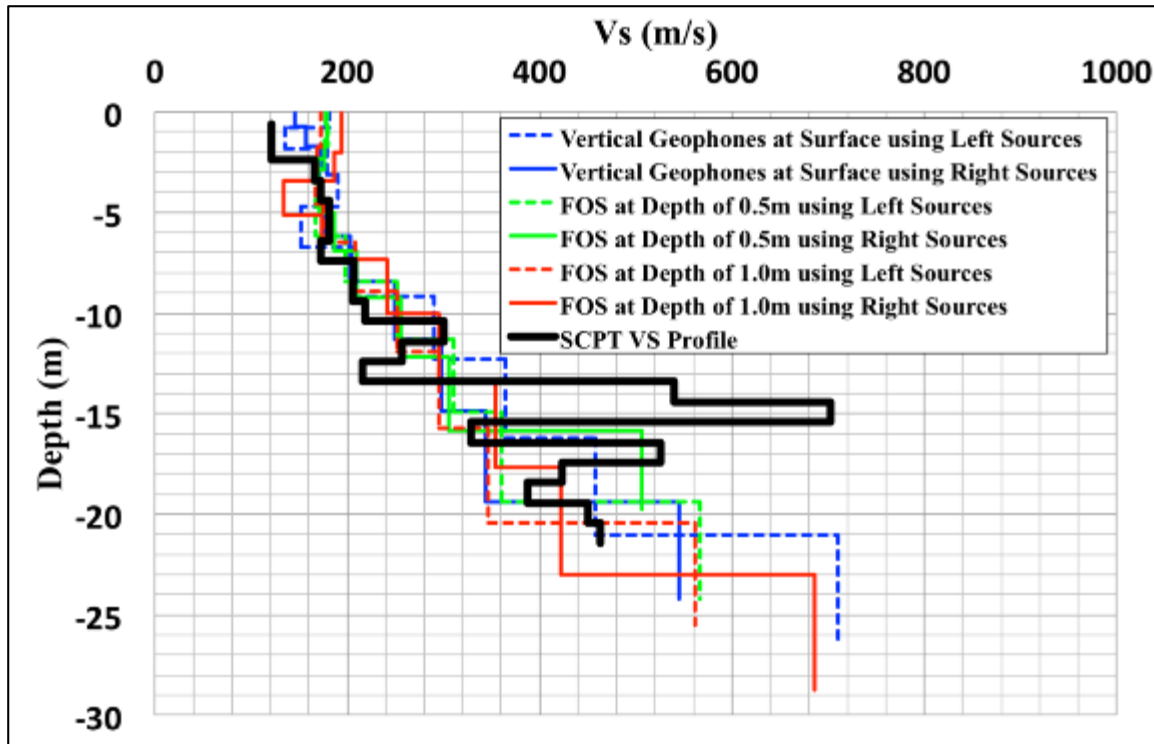
Figure 4.25   Shear wave velocity profile from SCPT test compared to field MASW
inverted shear wave velocity profiles.

When comparing the SCPT V_S with the MASW inverted V_S for the different

sensor arrays, larger discrepancies were observed at depths greater than 10 m. CPT tip

resistance and sleeve friction data was collected as the push rod advanced further with

depth to perform SCPT soundings and are included in Appendix B. CPT data suggests

that at these depths, thin sand layers with higher tip resistance were encountered. Based

on the expected geology at these depths, it could have been caused by the Catahoula

Formation, which may have existing sandstone layers (Murphy & Albertson, 1996).

Resolving thin layers at greater depths is a limitation of the MASW method. When thin

layers are close to the ground surface, these can be well resolved; at great depths the

resolution is limited and only large changes can be detected (Foti et al., 2015).

Differences in the MASW V_S profiles are also justified by the non-uniqueness of the

inversion problem, in where different subsurface properties could yield an identical

theoretical dispersion curve that is used for inversion (Foti et al., 2015).

CHAPTER V

SYNTHETIC SEISMOGRAMS METHODOLOGY

5.1   Introduction

A dynamic 2-D axisymmetric finite element (FE) analysis was used to model a field MASW survey and obtain time domain signals (i.e., traces) of vertical velocities, horizontal velocities, and longitudinal strains at discrete locations. These traces were to simulate data collected with vertical geophones, horizontal geophones and FOS, respectively. The data was extracted at three different depths: 0.0 m (i.e., at the ground surface), 0.5 m, and 1.0 m. At each depth, a set of signals for each modeled sensor type resulted in a synthetic seismogram dataset. These were then used in MASW analysis in the following chapter. The main objective of the synthetic seismograms was to further explore the phenomenon occurring at depth with the buried FOS and orientation of the FOS measurands.

5.2   Finite Element Model Description

A MASW survey test was modeled using a 2-D axisymmetric finite element (FE) geologic soil half-space model using the commercial software package COMSOL Multiphysics®. The FE model consisted of a simplified multi-layer model of the material properties of physical test site of the field experiments, and boundary conditions and excitation to simulate a MASW field data collection.

5.2.1 Finite Element Model Geometry

The test site was modeled as a 2-D axisymmetric 100-m-wide by 100-m-deep half-space. The axisymmetric boundary condition was applied to the leftmost boundary to reduce the model to 2-D; this is further explained in section 5.2.3. The extents of the model were selected to accommodate the array of sensors to be investigated (i.e., a 70-m sensor spread) and minimize undesirable reflections from the bottom and right side boundaries of the model.

At the surface (i.e., at 0.0 m) and at depths of 0.5 m and 1.0 m, 36 discrete points at 2-m spacing were added to the model starting at an offset of 2.5 m from the axisymmetric axis. Such discrete points are representative of 70-m spreads of geophone channel and FOS zone locations at the three different depths. The 2-m spacing represented the location between such channels and zones. This spacing was selected, as this was similar to the spatial distribution of FOS zones used in the field experiments (i.e., 2.041 m). The spacing was applied identically for all synthetic receivers to provide direct comparison of results. The offset of 2.5 m from the axisymmetric axis represented the distance from the seismic source to the first receiver (i.e., source-offset distance).

Geometrical discretization was also applied to the model for mesh consideration. Two fine layers were set up near the free surface to simplify meshing and data extraction at depths of 0.5 m and 1.0 m. At the ends of the spread, lines were extended to depth to ensure meshing uniformity. The resulting model geometry is shown in Figure 5.1.
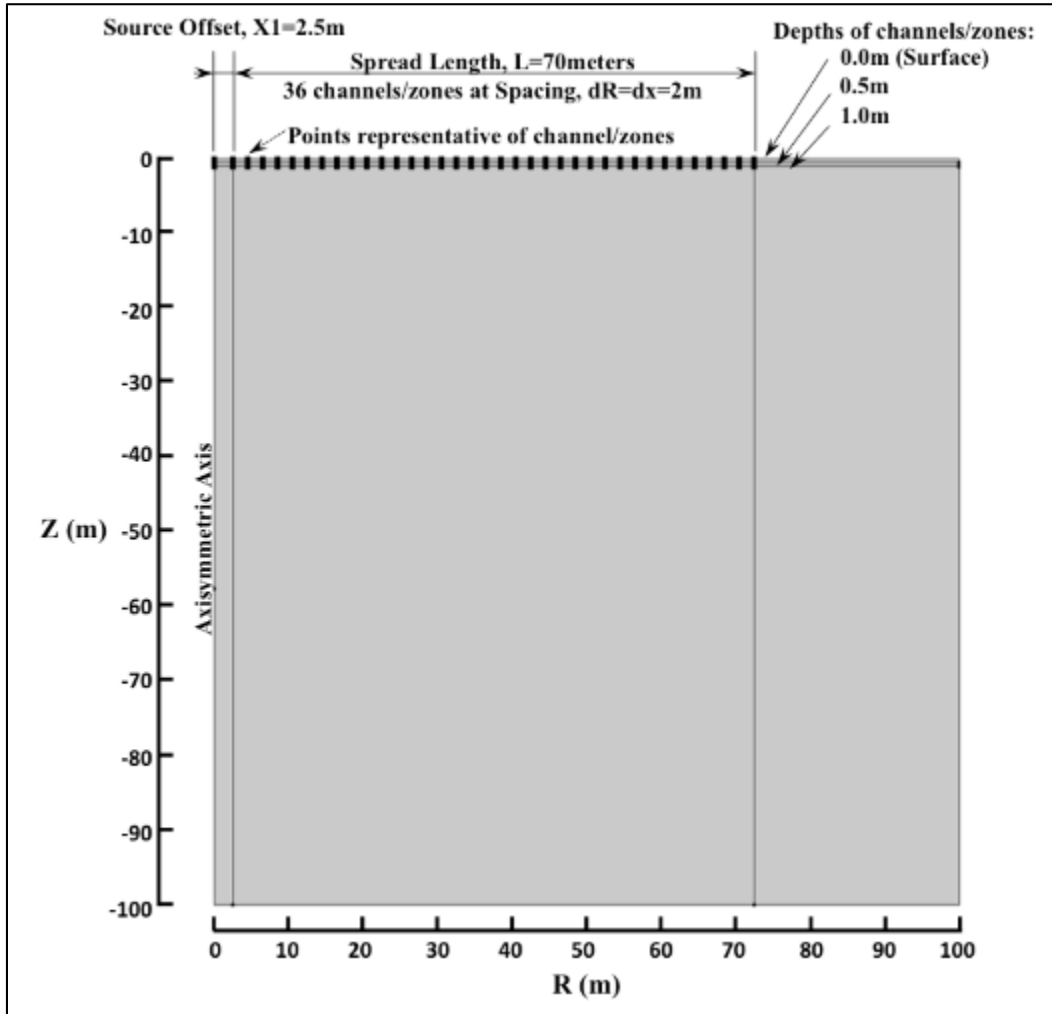
Figure 5.1   Finite element model geometry showing channel/zone locations.

5.2.2   Finite Element Model Material Properties

In the 2-D FE axisymmetric model, layers of soil were assumed to be horizontally homogeneous and isotropic. In the vertical direction, material properties varied. Layers of materials were not outlined in the geometry since interfaces within the different geologic materials were assumed to be continuous (Kramer, 1996), and thus were defined in the model as a function of depth.

Based on elastic wave propagation theory, material properties follow linear elastic relationships (Foti et al., 2015). To define soil layers in the wave propagation model, linear elastic material properties included: S-wave velocity, P-wave velocity and density.

An S-wave velocity profile was idealized to simulate MASW results of the field experiments discussed in the previous chapter. The idealization was based on an approximated visual average of the inverted shear wave velocities from the different sensors in the MASW field experiments. The V_S profile idealization consisted of five different layers as shown in Figure 5.2. The selection of five layers was selected to accommodate to the variation of V_S values with depth every 5 m up to a depth of 20 m. A constant V_S value was assigned for depths below 20 m.
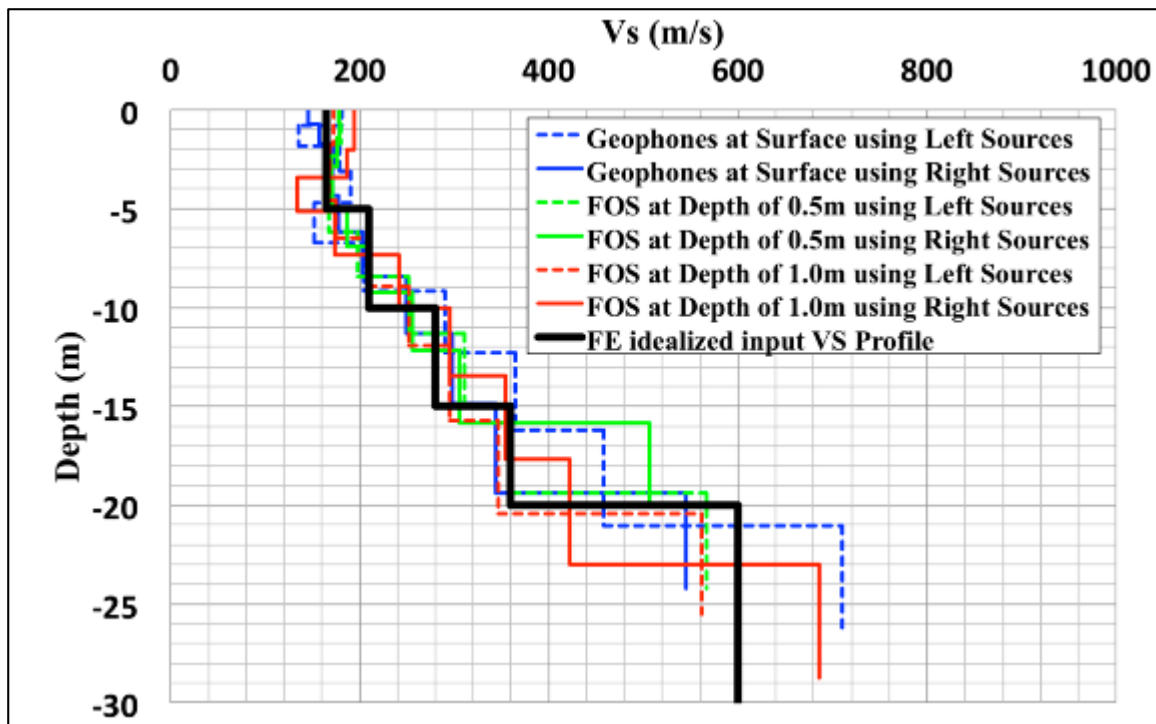
Figure 5.2   Finite element idealized input shear wave velocity profile compared to inverted MASW shear wave profiles obtained through field experiments.

The resulting V_S profile with depth was: 165 m/sec from 0.0 to 5.0 m in depth; 210 m/sec from 5.0 to 10.0 m in depth; 280 m/sec from 10.0 to 15.0 m in depth; 360 m/sec from 15.0 to 20.0 m in depth; and 600 m/sec beyond 20.0 m in depth. The idealized V_S profile input used in the FE model served to compare the accuracy of the inverted MASW V_S profile results from the synthetic seismograms.

P-wave velocities were set up based on the V_P/V_S ratio defined in Equation (2.3) using a constant Poisson's ratio value with depth of 0.3 (as defined in the field experiments). This resulted in a V_P with depth equal of about 1.87 V_S.

A constant density with depth of 1550 kg/m^3 was used, equal to the one assumed during the analysis of the field experiments. The use of a constant Poisson's ratio (used in V_P) and density allowed this study to ignore the effects on the variation of these properties with depth, and instead focus on the difference with depth in inverted MASW V_S results.

Material properties for the idealized layers are summarized in Figure 5.3.

5.2.3   Finite Element Model Boundary Conditions

The leftmost boundary of the model was defined as an axisymmetric boundary condition to simplify the 3-D wave propagation problem into a 2-D axisymmetric model. This simplification allowed signal decay due to geometrical spreading. The geometrical spreading permits the vertical transient displacement applied at the surface along the axisymmetric axis to propagate along cylindrical wave fronts (Foti et al., 2015). These wave fronts subsequently attenuate body waves and surface waves as a function of distance and depth, as would be expected in field measurements.

The upper surface (ground surface) was a free boundary condition to allow surface waves (i.e., Rayleigh waves) to generate.

The bottom and rightmost boundaries were low-reflecting boundary conditions, as defined by COMSOL® (2012). This type of boundary condition attempts to create a perfect impedance match, $\sigma \cdot \boldsymbol{n}$, for both P- and S-waves at the boundary such that:

$$\sigma \cdot \boldsymbol{n} = -\rho_{mat} V_{P_{mat}} \left(\frac{d\boldsymbol{u}}{dt} \cdot \boldsymbol{n}\right) \boldsymbol{n} - \rho_{mat} V_{S_{mat}} \left(\frac{d\boldsymbol{u}}{dt} \cdot \boldsymbol{t}\right) \boldsymbol{t} , \tag{5.1}$$

where $\boldsymbol{n}$ and $\boldsymbol{t}$ are the unit normal and tangential vectors at the boundary, respectively; ρ_{mat}, V_{Pmat} and V_{Smat} are the density, *P*- and *S*-wave velocities of the material domain adjacent to the boundary; and *du/dt* is the derivative of the displacement vector at the boundary. Equation (5.1) can be generalized as:

$$\sigma \cdot \boldsymbol{n} = -\boldsymbol{d}_i(\rho_{mat}, V_{P_{mat}}, V_{S_{mat}}) \frac{d\boldsymbol{u}}{dt} , \tag{5.2}$$

where the mechanical impedance $\boldsymbol{d}_i$ is a diagonal matrix that can be modified for user input. The default impedance in COMSOL® defined as:

$$\boldsymbol{d}_i = -\rho_{mat} \left(\frac{V_{P_{mat}} + V_{S_{mat}}}{2}\right) \boldsymbol{I} , \tag{5.3}$$

was used. Using the impedance in these boundary conditions, significant reflections from the boundaries back into the region of interest in the model (i.e., 70 m spreads of sensors) were prevented without the added expense of extending the size of the model.

Boundary conditions used in the model are summarized in Figure 5.3.
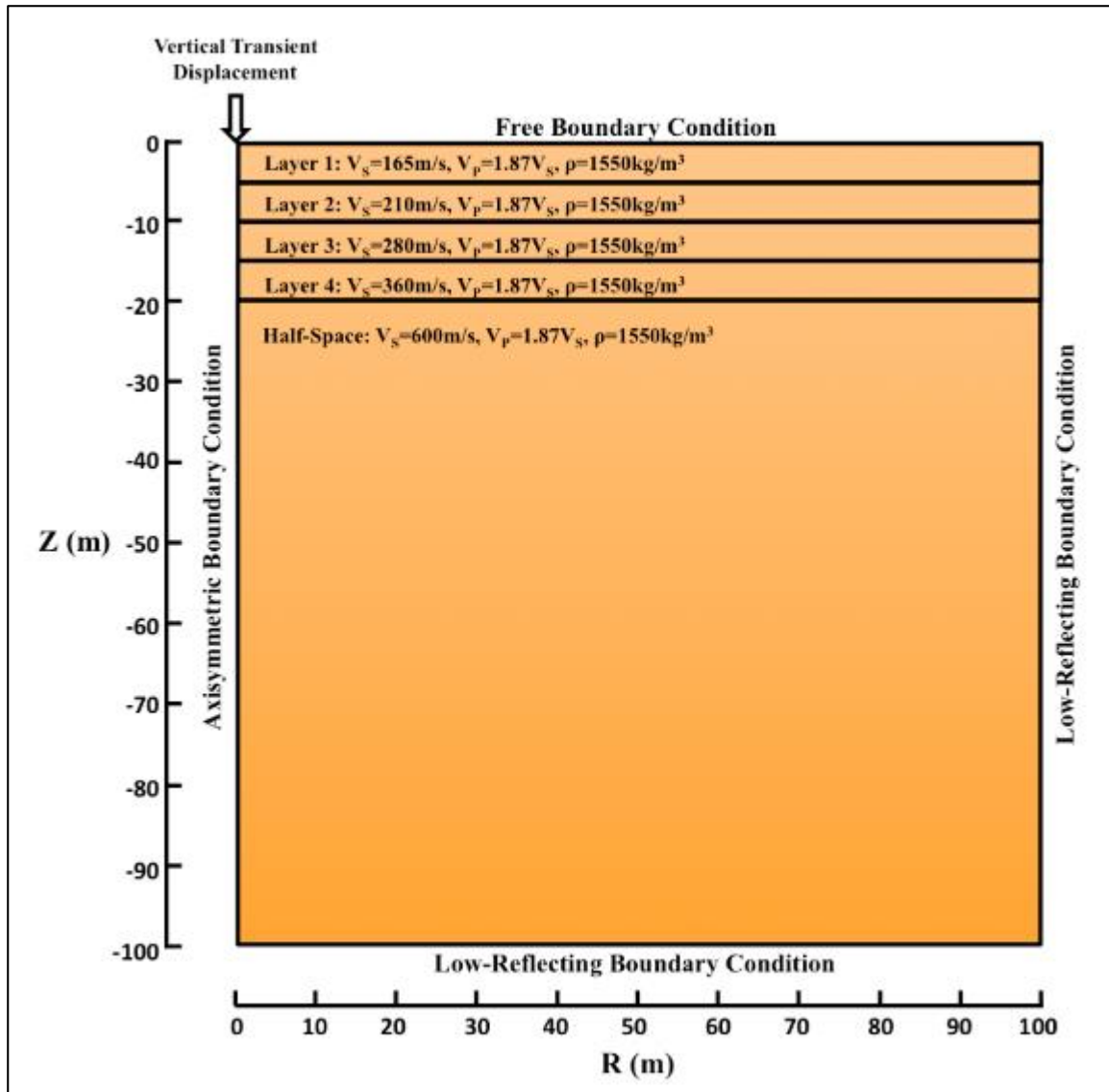
Figure 5.3   Boundary conditions and material properties used in the 2-D axisymmetric finite element model.

5.2.4   Finite Element Model Transient Impulse Loading

A vertical transient displacement was imposed on the axis of symmetry at the ground surface, as shown in the upper left corner of the model in Figure 5.3. The impulse

was a Gaussian pulse with center at 0.05 sec with a standard deviation of 0.01 sec. The

resulting time domain displacement input is shown in Figure 5.4.
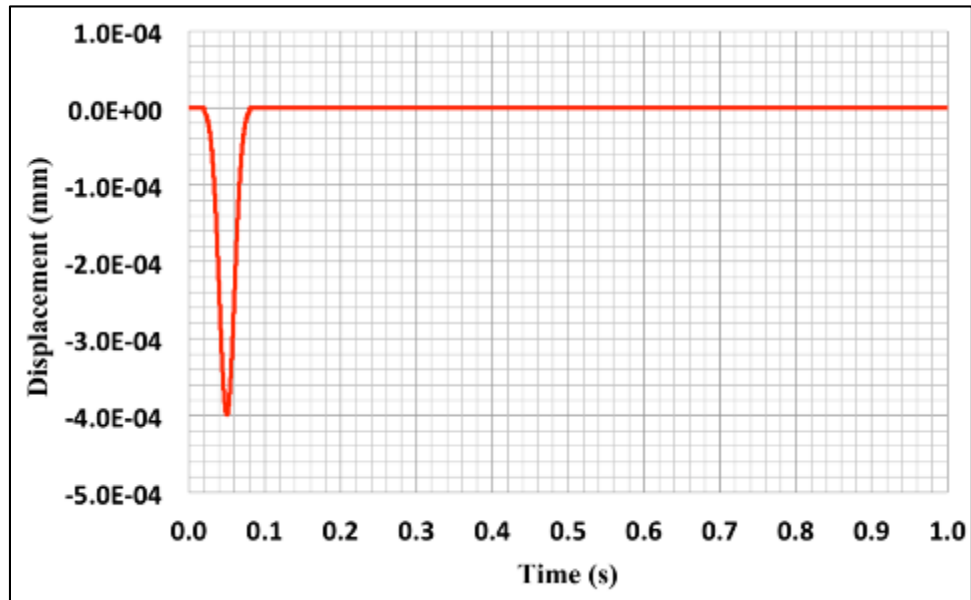
Figure 5.4   Gaussian vertical transient input displacement used during the simulation.

The FFT response from the Gaussian displacement input is shown in Figure 5.5. It

can be observed that at frequencies of about 60 Hz and above, amplitudes were limited by

the energy imparted by the input Gaussian transient displacement pulse.
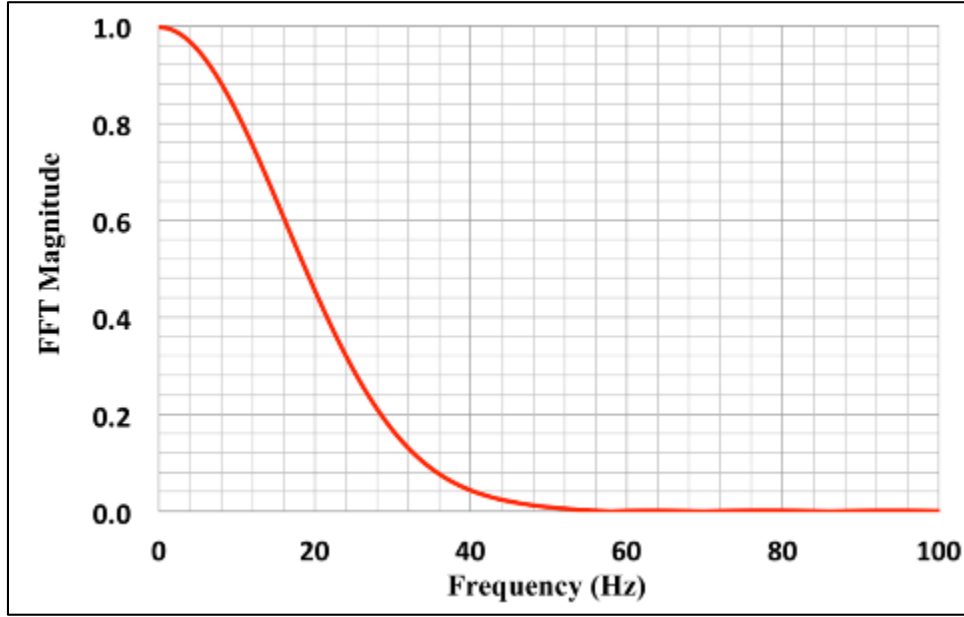
Figure 5.5   FFT of Gaussian vertical transient input displacement.

5.2.5   Finite Element Mesh

After preparing the model, spatial discretization considerations were needed. This
was defined in the simulation through the mesh element size. The mesh element size was
controlled by the minimum Rayleigh wavelength, λ_{Rmin}, defined in this study as:

$$\lambda_{Rmin} = \frac{V_{Rmin}}{f_{max}},$$
(5.4)

where V_{Rmin} is the minimum R-wave velocity and f_{max} is the maximum frequency input
imparted by the input seismic source load. In this study, V_R can be approximated as
0.93V_S using Equation (2.5) with the constant Poisson's ratio of 0.3. Thus, since the
minimum shear wave velocity, V_{Smin}, defined in the model was 165 m/sec, this resulted in
a V_{Rmin} of about 153 m/sec. The f_{max} used in this study was considered to be
approximately 60 Hz, based on the FFT response shown in Figure 5.5. Using these values
in Equation (5.4), λ_{Rmin} is about 2.56 m. To ensure that the finite element mesh could

112

resolve λ_{Rmin}, the maximum element size, Δx_{max}, was set to allow discretization of a minimum of eight elements per wavelength, such that:

$$\Delta x_{max} = \frac{\lambda_{Rmin}}{8}.$$ (5.5)

This resulted in a Δx_{max} of 0.32 m. For meshing uniformity within discrete locations to be sensed, Δx_{max} was further simplified to 0.25 m. This allowed for about 10 elements within the minimum wavelength considered. A quadratic discretized mesh with quadrilateral element size of 0.25 m was used throughout the model. The mesh consisted of a total of 160,800 elements, as shown in Figure 5.6.
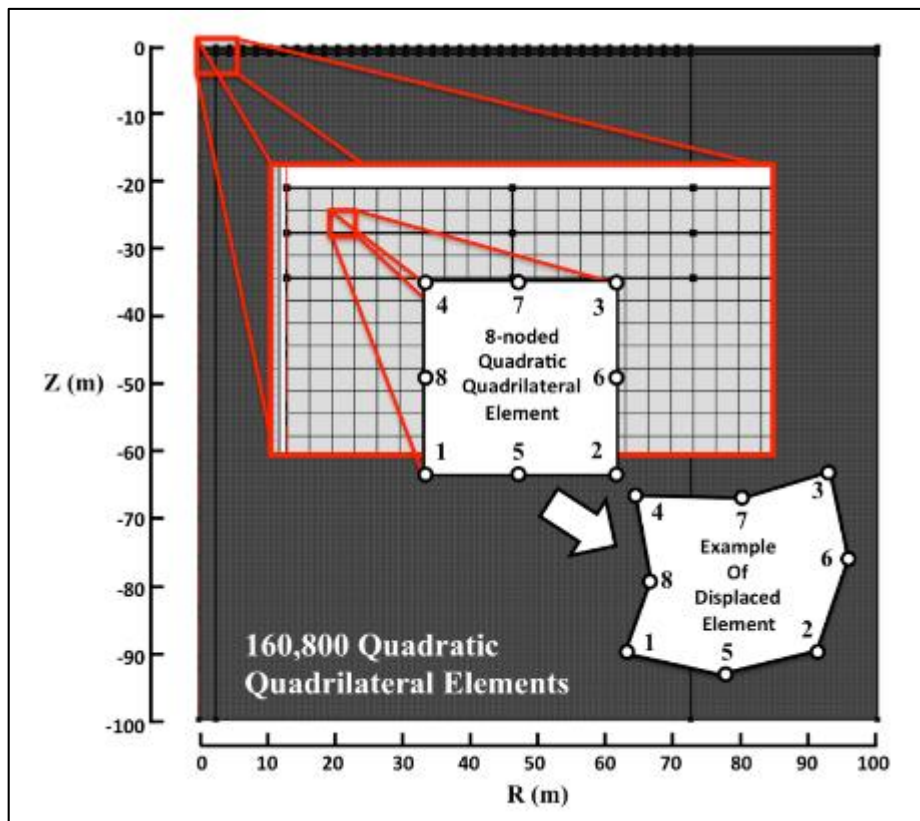
Figure 5.6   Quadratic discretized mesh with uniform square quadrilateral elements of size of 0.25 m used throughout the model.

113

5.2.6   Finite Element Time Domain Analysis

Following the spatial discretization, temporal resolution was defined using a critical time step, $\Delta t_{critical}$. Although COMSOL® mainly uses an implicit time integration solver, $\Delta t_{critical}$ was determined using the Courant-Frederichs-Lewy (CFL, 1928) condition defined by:

$$CFL = \frac{V_{Pmax}\Delta t_{critical}}{\Delta x_{max}} \tag{5.6}$$

where V_{Pmax} is the maximum P-wave velocity, given by *1.87 V_{Smax}* (i.e., 1.87 * 600 m/sec), which results in 1122 m/sec. Solving for a CFL value of 0.5 to ensure numerical stability, $\Delta t_{critical}$, can be solved for as:

$$\Delta t_{critical} = \frac{0.5\Delta x_{max}}{V_{Pmax}}. \tag{5.6}$$

This resulted in a critical time step of 0.00011 sec. Therefore, for the time dependent simulation, a time-step size of 0.0001 sec was used for a total simulation time of 1 sec. Data was saved for every 0.001 sec of simulation time, similar to the data collected during the field experiments. A snapshot of displacement at 0.2 sec of simulation is shown in Figure 5.7. Corresponding vertical velocities, horizontal (i.e., radial) velocities, and horizontal (i.e., radial) strains for the same snapshot in time are shown in Figure 5.8, 5.9, and 5.10, respectively.
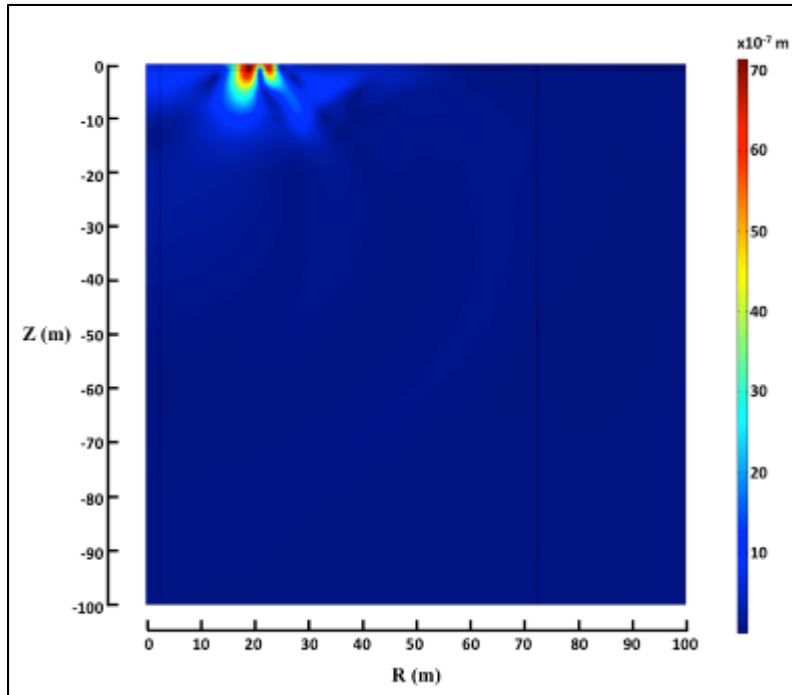
Figure 5.7   Snapshot of total displacement at 0.2 sec of simulation time.
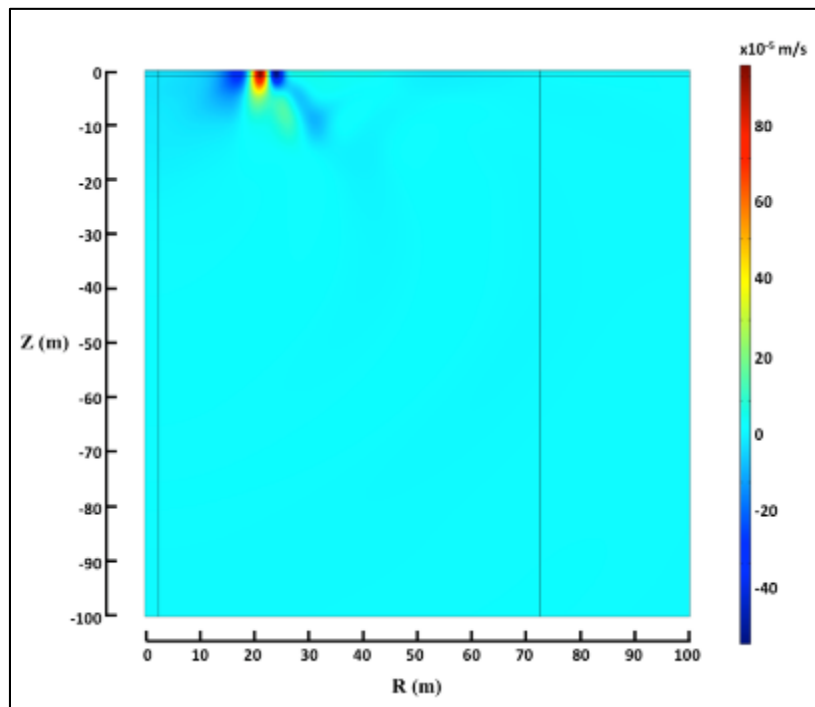
Figure 5.8   Snapshot of vertical velocities at 0.2 sec of simulation time.

115
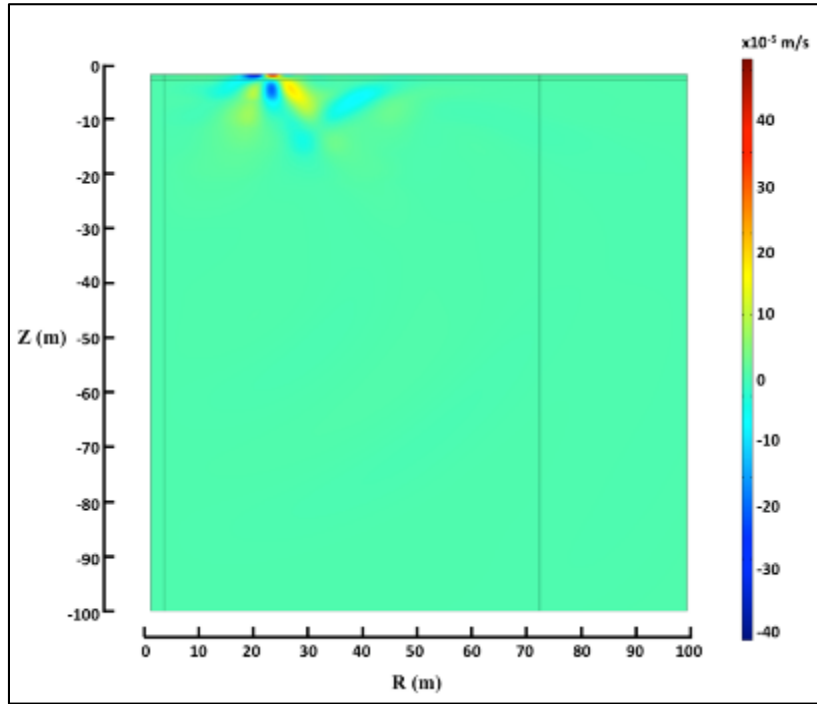
Figure 5.9   Snapshot of horizontal velocities at 0.2 sec of simulation time.
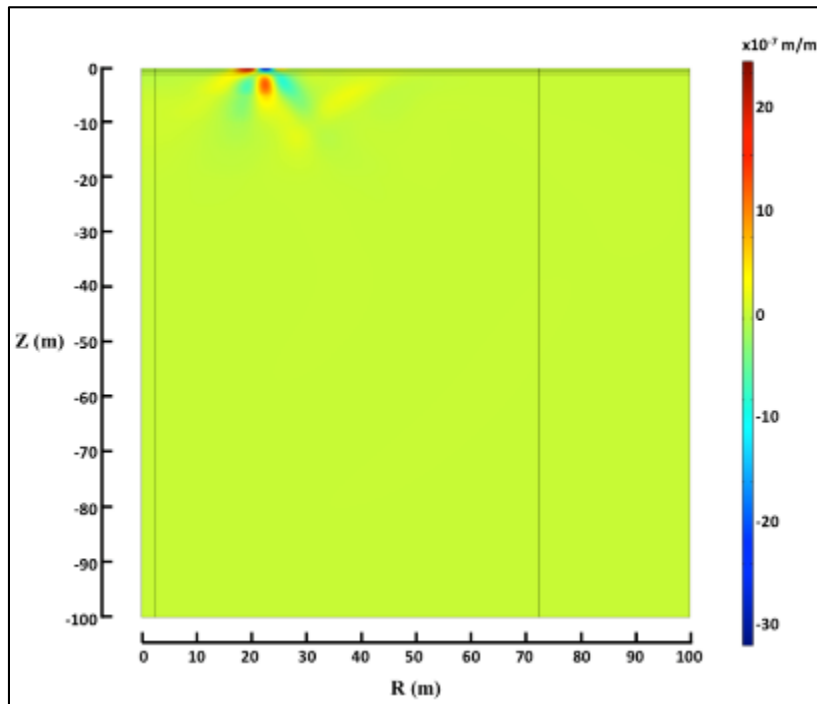
Figure 5.10   Snapshot of horizontal strains at 0.2 sec of simulation time.

5.3   Extraction of Synthetic Seismograms

Although velocity and strain data were obtained throughout the model in the finite element analysis, as shown in Figures 5.8 through 5.10, time domain signals (i.e., traces) were only extracted at discrete points defined in the geometry shown in Figure 5.1. Remaining data was not used in this study. Extraction of time domain signals of vertical and horizontal velocities at the discrete points represented vertical and horizontal geophones, respectively, at depths of 0.0 m (i.e., at the surface), 0.5 m, and 1.0 m. Traces of average horizontal strain over 5-m lengths centered at the defined discrete points representative of FOS zones were obtained at the same depths. Synthetic seismograms resulting from acquired traces allowed comparisons to be made for the geophones and FOS at different depths.

Although no sensors were used in the model, the point vertical velocities are referred to as vertical geophones, point horizontal velocities will be referred as horizontal geophones, and average horizontal strains will be referred to as FOS. The respective depths were used to describe the sensor location.

CHAPTER VI

SYNTHETIC SEISMOGRAMS ANALYSIS AND RESULTS

6.1   Synthetic Seismograms Data

Synthetic seismograms of simulated vertical and horizontal geophones, and simulated FOS for different installation depths were obtained through a finite element (FE) dynamic analysis, as described in Chapter V. MASW analysis of the synthetic data from the geophones and FOS was conducted. Results of the MASW analysis were compared with respect to sensor type and installation depth. The subsequent MASW inverted V_S profiles for the different types of sensors and installation depths were compared to the idealized input shear wave velocity profile used in the FE model.

6.2   Synthetic Seismogram Test Matrix

As previously described, spreads of vertical and horizontal geophones, and FOS zones were simulated using discrete points in the 2-D FE model. A total of 36 discrete points were used, spaced every 2 m. The sensor arrays formed spreads of 70 m in length. All measurements were obtained from the same FE model using the vertical displacement pulse acting on the ground surface along the axis of symmetry, at a source offset of 2.5 m. A test matrix describing the difference in the synthetic seismogram data is shown in Table 6.1.

Table 6.1   Test matrix summary of synthetic seismograms obtained with vertical and horizontal geophones, and FOS at depths 0.0 m, 0.5 m, and 1.0 m.

Sensor Type	Sensor Depth
Vertical Geophones	0.0 m
	0.5 m
	1.0 m
Horizontal Geophones	0.0 m
	0.5 m
	1.0 m
FOS Zones	0.0 m
	0.5 m
	1.0 m

These synthetic seismograms generated a total of nine seismic data files: three for the vertical geophones, three for the horizontal geophones and three for the FOS. Every set of three seismic data files for each sensor corresponded to depths of 0.0 m, 0.5 m, and 1.0 m. These data files were then used for the MASW analysis.

6.3   Analysis Procedure for Synthetic Seismograms

Synthetic seismograms were processed using a similar procedure as the field data using KGS's SurfSeis® software.

6.3.1   Preprocessing Synthetic Seismograms

6.3.1.1   File Format Conversion of Synthetic Seismograms

All seismograms from the FE were obtained in ASCII format and needed to be converted in the standard SEG-2 binary format (Pullan, 1990) required to import data into SurfSeis®. This was performed using a script created in Matlab® named ASCIItoSEG2.m, shown in Appendix A.2. Once data was available in the required format, it was imported into SurfSeis®.

6.3.1.2 Installation Geometry Assignment of Synthetic Seismograms

After data was imported into SurfSeis®, installation geometry was assigned. This involved specifying the location of the synthetic receivers (i.e., geophones and FOS) and offset of the seismic source (i.e., transient pulse) to the first receiver. The metric stationing system used referenced the first receiver from the seismic source as station 1001. The increment between stations was set as 2 m based on the spacing of the receivers. Following this stationing system, receiver locations were assigned to be from station 1001 to station 1036. Seismic source offset was set at 2.5 m, which represents Station 999.75. The geometry assignment with the corresponding metric stationing reference is shown in Figure 6.1.
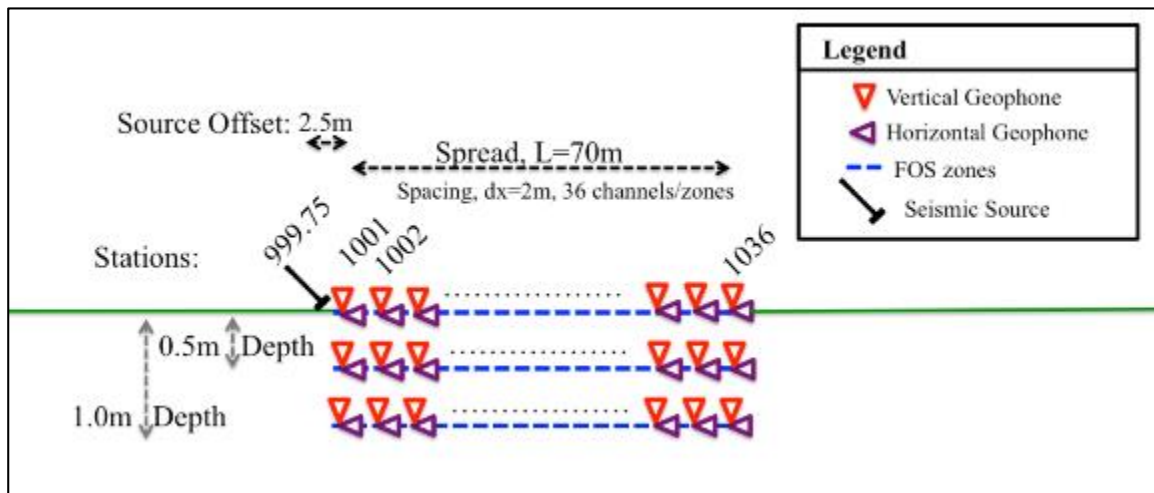
Figure 6.1   Synthetic seismogram installation geometry metric stationing system.

6.3.2 Dispersion Analysis from Synthetic Seismograms

6.3.2.1 Dispersive Imaging from Synthetic Seismograms

Using the synthetic seismograms, the coherency patterns of the propagating velocities of each constituent measurement were used to calculate the variation of phase velocities as a function of frequency, i.e., dispersive imaging. This was performed using the *phase-shift* method (as discussed in section 2.2.2.3.1) implemented in SurfSeis® by scanning through different phase velocities over the desired frequency of interest. Identically to the analysis of the field data, scanning was performed for phase velocities ranging from 50 to 1000 m/sec in 1-m/sec increments over a selected frequency range of 5 to 100 Hz in 0.01-Hz increments. The scheme used by this method was summarized in Figure 2.22. An example of the resulting dispersive imaging from the synthetic seismograms is shown in Figure 6.2. Compared to the analysis of the field data, no combination of dispersive images was performed since only one source offset was used for the simulation.
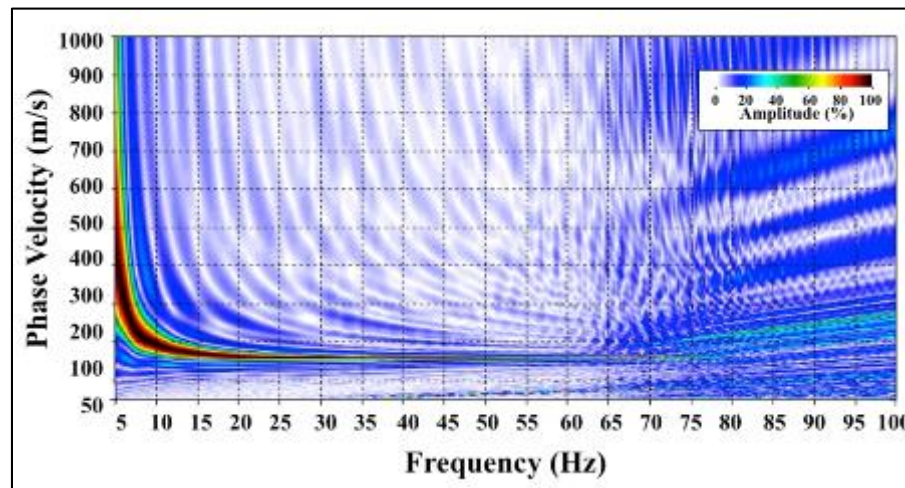
Figure 6.2   Example of dispersive image obtained using synthetic seismograms of vertical geophones at the surface.

6.3.2.2 Dispersion Curve Selection from Synthetic Seismograms

The resulting dispersive images from each synthetic seismogram were used to determine the fundamental mode dispersion curves. This was performed applying qualitative interpretation to select discrete points of peak fundamental-mode phase velocity amplitude over different frequencies. An example was shown in Figure 4.10 for the field data analysis. In the same manner as the analysis of the field data, selection of these points was based on phase velocity amplitude energy of above 50%. It was decided that, at a minimum, 15 points were to be selected. In many instances, however, more points were needed to better define the curvature representing the dispersion curves. Other considerations for interpretation of the dispersion curves included: (1) avoiding frequencies gaps greater than 5 Hz over which the M0 dispersion curve could not be interpreted with high confidence, and (2) avoiding locations of possible higher mode contamination of the fundamental mode (M0). An example of these considerations was shown in Figure 4.11.

Interpretation of the fundamental mode for each respective sensor was performed with no consideration of the dispersion curve selection of other sensors (and other depths) to treat each data independently.

Influences on higher modes were noted in the dispersive images. However, since the MASW, on which this study concentrates, focuses on determination of the fundamental modes of Rayleigh waves, only the M0 dispersion curve was used for analysis.

6.3.3   Inversion Analysis from Synthetic Seismograms

Following the same steps used in the analysis of the field data, the resulting dispersion curves were then used for inversion (back-calculation) to obtain 1-D V_S profiles with depth for the different sensors. An initial inversion model was defined using the input material properties used in the FE model shown in Table 6.2. A theoretical forward dispersion curve was calculated using the initial inversion subsurface properties, which consisted of: layer thickness (h), density (ρ), S-wave velocity (V_S), and Poisson's ratio (υ). Although the layer thicknesses of the FE model were known, the initial inversion model consisted of ten layers with variable thickness. Similar to the inversion of the field data, having ten layers was considered to provide adequate vertical resolution as well as numerical stability for the inversion to resolve changes in the dispersion curves. The variable thickness of the layers was made to accommodate layers to the dispersion curves curvature. The corresponding thickness of layers was adjusted based on the wavelength scaling as a function of frequency as outlined in Equation (2.16). To project the maximum depth of investigation, a depth to wavelength ratio (Z_{MAX}/λ_{MAX}) of 0.35 was used. This ratio followed the conservative end of the range defined in the relationship of Equation (2.8). The maximum wavelength, λ_{MAX}, was solved for using Equation (2.6), with inputs of phase velocity at the lowest frequency defined in the dispersion curve and its corresponding frequency.

Estimates of shear wave velocities for the initial inversion model were found multiplying the average phase velocity over each layer by a factor of 1.08. The value of 1.08 was determined from Equation (2.5) using the selected Poisson's ratio of about 0.3.

Table 6.2   Initial Model Parameters Used for Inversion Analysis of Synthetic
           Seismograms

Material Property	Values considered for analysis
Layer Thickness (h)	Depth is scaled using the corresponding wavelengths as a function of frequency as shown in Equation (3.13). Layers are adjusted by the rate of change of values picked in the dispersion curve.
Density (ρ)	1.55 g/cm^3
Poisson's Ratio (υ)	0.3 (In the FE model V_P was defined using this constant value of Poisson's ratio, which resulted in $V_P = 1.87 \, V_S$)
Shear Wave Velocity (V_S)	Initial estimate is based on average dispersion curve phase velocities corresponding to each layer as 1.08 V_R

Through the inversion process, only V_S was updated iteratively to obtain a new forward theoretical dispersion curve until an acceptable fit to the measured dispersion curve was achieved. Stopping criteria considered for an acceptable fit included a root mean square error (RMSE) in phase velocity of 5.0 m/sec and a maximum of 10 iterations. These parameters were identical to those used in the field data analysis, and were considered appropriate, as smaller RMSE values yielded similar results and the iterations never reached the specified maximum number of iterations. The final V_S values were considered to be the 1-D V_S profile of the site. An overview of the analysis procedure is presented as a flowchart in Figure 6.3.
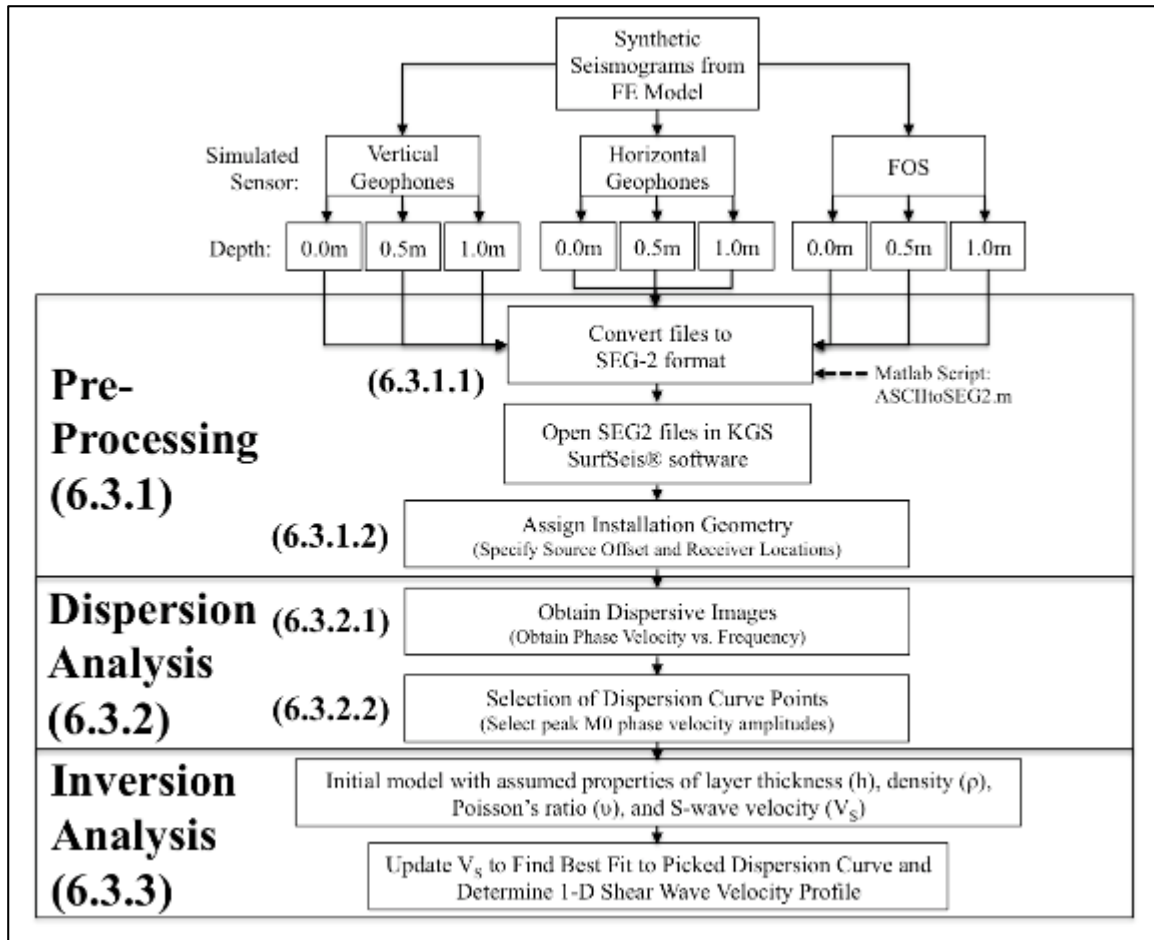
Figure 6.3   MASW procedure to obtain 1-D S-wave velocity profile from synthetic seismograms.

6.4   Synthetic Seismogram Results

6.4.1   Synthetic Seismograms

Seismograms of the vertical geophones (represented using point vertical velocities), horizontal geophones (represented using point horizontal velocities), and distributed FOS (represented by averaged horizontal strains) were obtained at depths of 0.0 m, 0.5 m, and 1.0 m using the FE model. The normalized trace amplitude synthetic seismograms are shown in Figure 6.4 for the vertical geophones, horizontal geophones,

and FOS, respectively. Because of the absence of noise in the synthetic signals, the arrival times of the different wave types are easily distinguished. The normalized amplitudes shown in Figures 6.4 depict slight variations in trends of arrival times. This variation may be likely caused by the interaction of different wave types or the arrival times associated with different modes. This is further justified by the decrease of vertical and horizontal amplitudes with depth as shown in Figure 2.4. By comparing the trace amplitudes of the geophones and FOS, there is better agreement of the FOS with the horizontal geophones since both measured the horizontal component of the wave propagation. It was also noted that the seismograms recorded minor reflections due to the low-reflecting boundary ends of the model. Since the seismic source offset and direction is specified in the installation geometry, such minor inverse propagating amplitudes, although coherent, were ignored in the post processing.
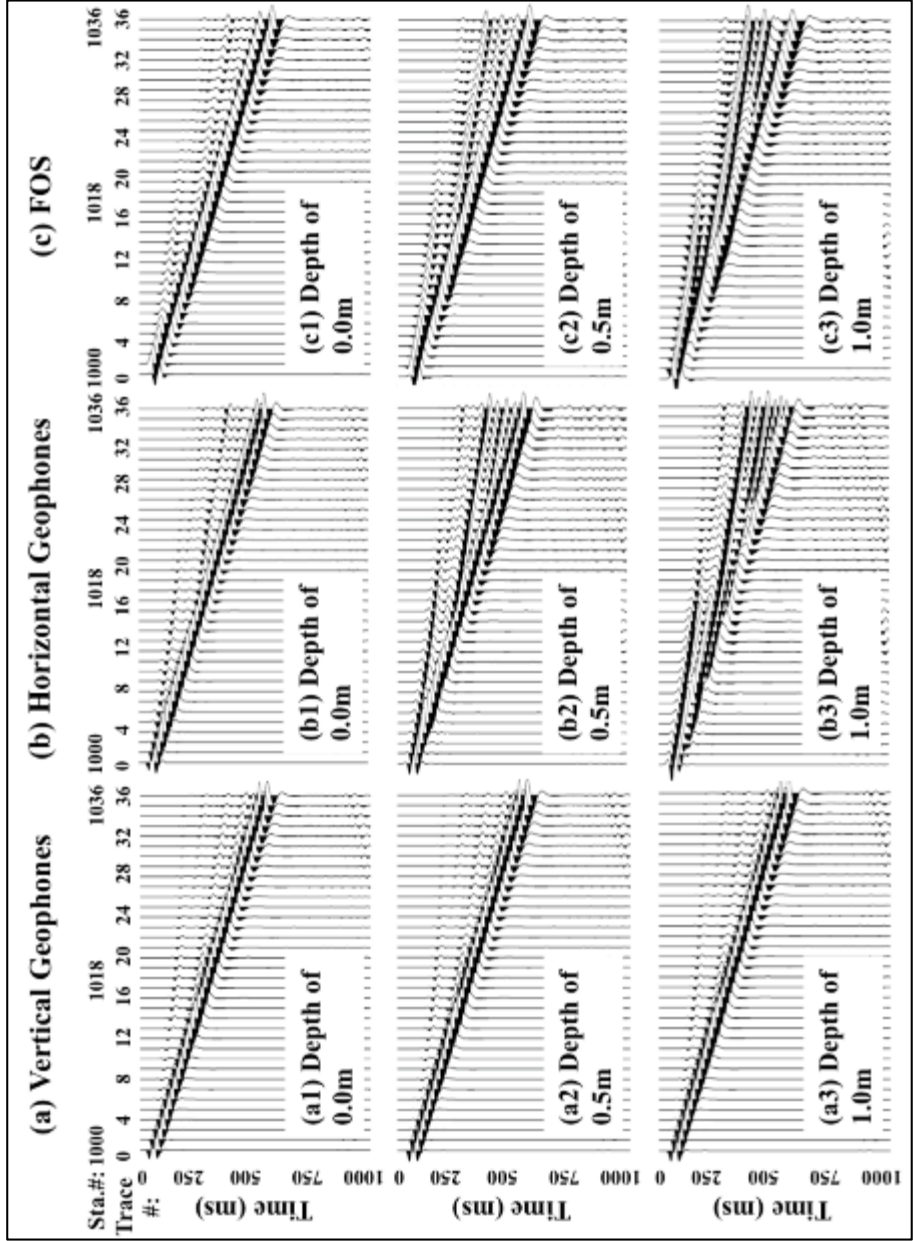
Figure 6.4   Synthetic seismograms with normalized trace amplitudes.

For the simulated (a) vertical geophones, (b) horizontal geophones, and (c) FOS at the extracted depths of 0.0 m, 0.5 m, and 1.0 m, respectively.

127

6.4.2 Dispersive Imaging Results from Synthetic Seismograms

Dispersive images were created with synthetic data obtained for each simulated sensor at the different depths investigated. Results are shown in Figure 6.5.

Amplitudes were limited by the energy imparted by the input Gaussian transient displacement pulse at frequencies above 60 Hz, as previously shown in Figure 5.5. Even though this was evident at frequencies above 60 Hz, these high frequencies are typically not excited in field data collections by the type of seismic source used (e.g., sledgehammer). For this reason, the ultimate goal of obtaining a V_S profile with depth was not affected.

Although the dispersive images from the different sensors are similar in many ways there are some important differences. The vertical geophones dispersive images, shown in Figures 6.5 (a1, a2, a3), showed good consistency with depth where the fundamental modes were apparent. On the other hand, the dispersive images of the horizontal sensors (i.e., horizontal geophone and FOS), shown in Figures 6.5 (b1, b2, b3, c1, c2, c3), were not as consistent with depth. As explained through the seismograms, this could have resulted from the interaction of different wave types and effects associated with different modes.

The dispersive image of the horizontal geophones at the surface (Figure 6.5(b1)) showed a very well defined fundamental mode. At depths of 0.5 m and 1.0 m (Figures 6.5 (b2, b3)), the existence of higher modes was more evident and frequencies were more limited in range.
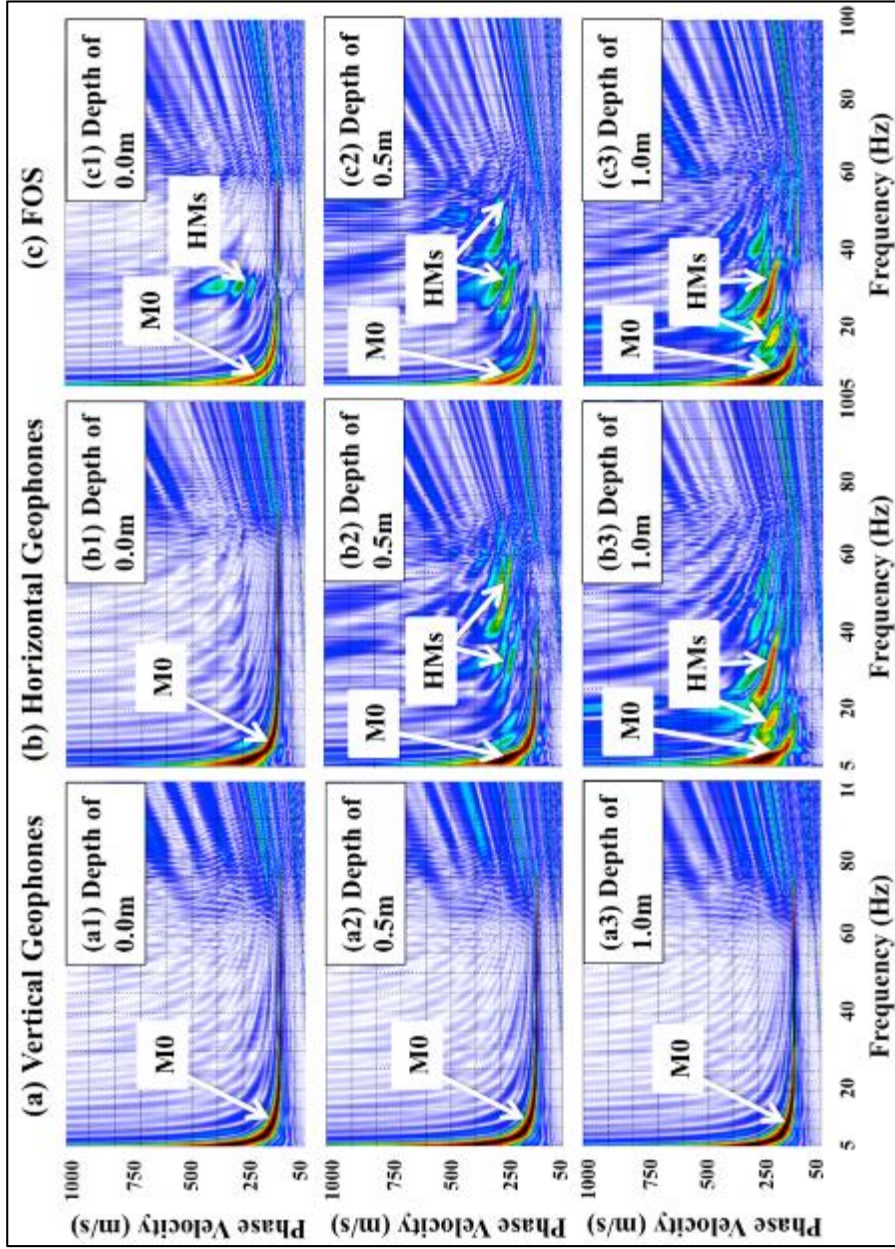
Figure 6.5   Dispersive images obtained from synthetic seismograms of the different sensors and respective sensor depths.

Also showing peak amplitudes phase velocities corresponding to R-wave fundamental mode (M0) and the existence of higher modes (HMs).

129

The FOS dispersive images (Figures 6.5(c1, c2, c3)) displayed higher modes at the surface and these were more apparent with increasing depth. The frequency ranges of the fundamental mode were similar to those obtained with the horizontal geophones.

6.4.3   Dispersion Curves Results from Synthetic Seismograms

As in the case of the field experiments, patterns of the apparent fundamental Rayleigh mode M0, noted in Figure 6.5, were used for dispersion curve interpretation. Discrete points of interpreted peak fundamental-mode phase velocity amplitude over different frequencies were selected to obtain the M0 dispersion curve. The selected dispersion curves are shown in Figure 6.6.
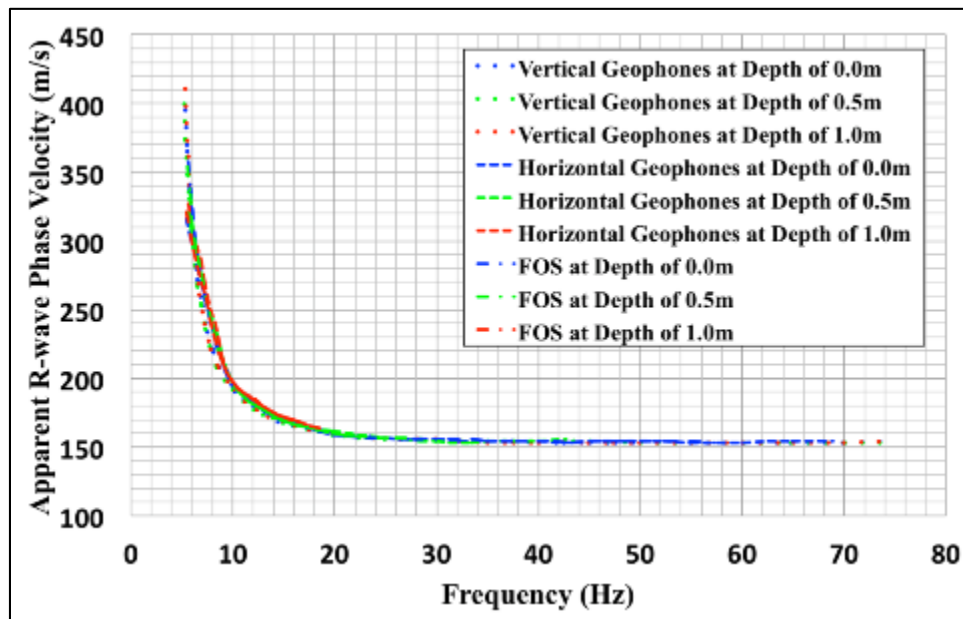
Figure 6.6   Comparison of interpreted dispersion curves from the synthetic experiment seismograms for the different sensors and respective sensor depths.

Ranges in frequency of the dispersion curves affect the depths at which the shear wave velocities can be estimated. Frequencies, as low as 5 Hz, were achieved for all sensor types. As a result, this allowed the survey to reach about the same depths of investigation.

The M0 dispersion curve obtained with the vertical geophones achieved higher frequencies than horizontal geophones and FOS. As previously mentioned, higher frequencies are used to determine V_S at shallow depths. It was also observed that higher frequencies were obtained with the simulated sensors placed at the ground surface than the buried sensors.

The R-wave M0 dispersion curve was defined for the dispersive images of the vertical geophones up to frequencies to about 75 Hz with no apparent influence of higher modes, as shown in Figures 6.5(a1, a2, a3). As a result, the M0 dispersion curve was selected with easier judgment for the different investigated depths.

The selection of M0 dispersion curves for the horizontal geophones and the FOS were similar since both sensors are essentially a function of the horizontal component of wave propagation. The M0 could be resolved easily for both of these sensors at the lower frequencies. The maximum frequency at which M0 could be resolved, however, decreased with depth as higher modes obscured the fundamental mode, as shown in Figures 6.5(b2, b3, c2, c3).

The dispersive images associated with the horizontal geophones at the surface were easier to interpret. This was a result of the peak amplitude phase velocities in the dispersive images representing M0 extending continuously to higher frequencies, as shown in Figures 6.5(b1, b2, b3). The dispersive images associated with the FOS,

however, were more difficult to interpret. This was due to gaps caused by possible higher

modes in the peak phase velocity associated with M0, as shown in Figures 6.5(c1, c2, c3).

These gaps are likely the result of the sensor length, or aperture, of the longitudinal strain

measurement. The aperture relates to the FOS measuring the average strain over 5-m

zones in comparison to the geophones measuring velocity at discrete point locations. A

possible higher mode displacement pattern could have generated a stronger frequency

response over a length of FOS, not perceived otherwise by the geophones. For this

reason, based on the frequency gap considerations on selecting dispersion curve points

mentioned in section 6.3.2.2, slightly higher frequencies were interpreted for the

dispersion curves of the horizontal geophones.

6.4.4   Shear Wave Inversion Results from Synthetic Seismograms

To maintain consistency in the interpretation for estimating 1-D V_S profiles for

each of the obtained dispersion curves, the inversion procedure was performed in the

same manner as the field experiments. The procedure and inversion parameters used are

described in section 6.3.3. The final inverted V_S profiles obtained using the dispersion

curves are shown in Figure 6.7.
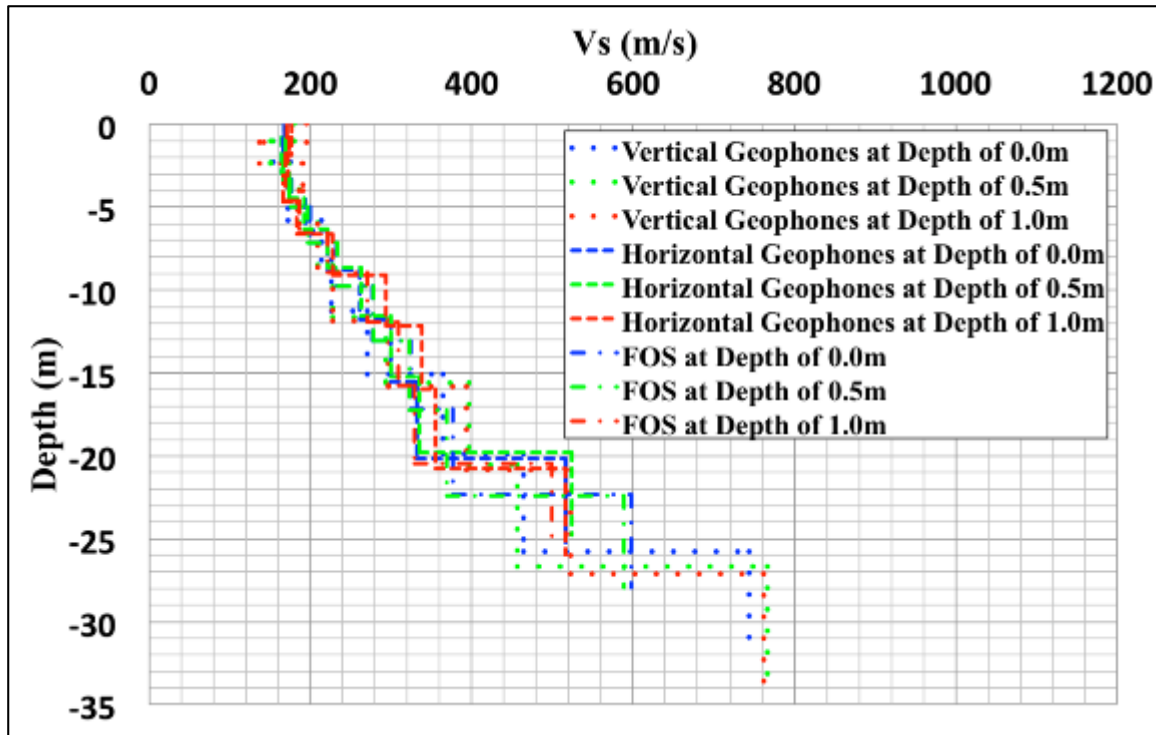
Figure 6.7   Final inverted Vs profiles obtained from the different dispersion curves using the synthetic seismograms.

Differences in shear wave velocities show the non-uniqueness of the inversion process, where multiple shear wave profiles (and also other changing material properties) can yield similar dispersion curves. Depths from 32.23 to 33.98 m were obtained using the vertical geophones. Depths from 24.77 to 25.96 m were obtained using the horizontal geophones. Depths from 25.59 to 27.96 m were obtained using the FOS. Irrespective of these differences, the shear wave velocities obtained with the FOS at the different sensor depths were in the same range as those obtained with vertical and horizontal geophones.

6.5 Verification using Idealized Shear Wave Velocity Input in Finite Element Model

In order to verify the V_S inversion results obtained through the MASW analysis, the FE input shear wave velocity profile, shown in Figure 5.2, was utilized. Figure 6.8 includes the FE input V_S profile, as well as the inverted MASW V_S profiles for comparison from Figure 6.7.
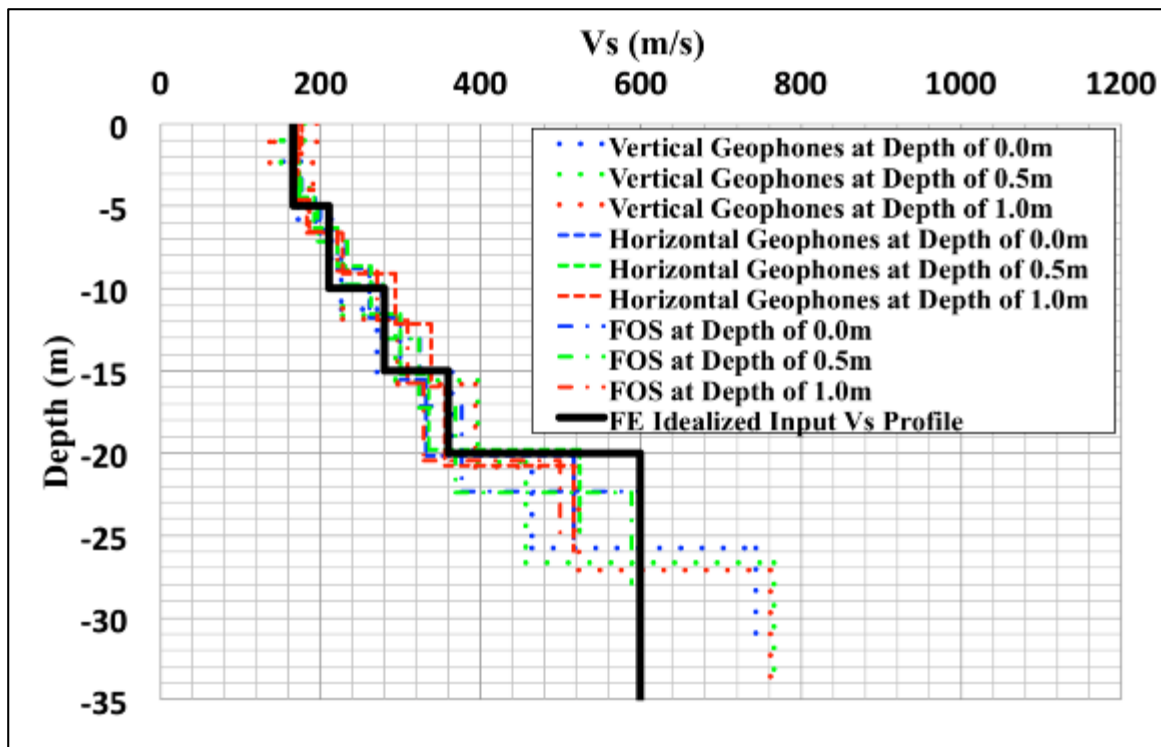
Figure 6.8   Input shear wave velocity profile used in finite element model compared to MASW inverted shear wave velocity profiles obtained from synthetic seismograms.

Comparing the FE V_S input with the MASW inverted V_S for the different sensor arrays, comparable V_S values were observed, particularly at the shallower depths. Results show that the vertical geophones have slightly more variation near the surface than the

horizontal sensors and overestimate the V_S at the lowest layer outlined in the FE model. This was observed at the three different sensor depths, shown in Figure 6.8. Profiles determined with horizontal geophones and FOS appeared to have better overall agreement with the FE input V_S profile. As explained in the results from the field experiments, differences in the MASW V_S profiles are also justified by the non-uniqueness of the inversion problem, in where different subsurface properties could yield an identical theoretical dispersion curve that is used for inversion (Foti et al., 2015).

CHAPTER VII

SUMMARY AND DISCUSSION OF RESULTS

7.1 Introduction

The results from field experiments and synthetic seismograms are summarized
and discussed. The results from both approaches are used to describe the effectiveness of
FOS when compared to geophones. The main two topics to be discussed include the
effects of sensor orientation (i.e., vertical vs. horizontal measurements) and depth; and
differences in uncertainty related to the measurements with FOS and geophones.

7.2 Horizontal Surface Wave Propagation and Effects of Installation Depth

The effects on sensor orientation and installation depth was investigated through
synthetic seismograms obtained with the finite element model and were compared to
results obtained in the field experiments. In the synthetic seismograms shown in
Figure 6.4 it can be noted that the seismograms measured by the FOS resemble more
those produced by the horizontal geophones than those produced by the vertical
geophones. This is due to the fact that horizontal (or longitudinal) strains measured by the
FOS are dependent on the horizontal displacement of wave propagation. The distinction
between vertical and horizontal orientation sensors (i.e., vertical geophones and FOS,
respectively) can be also observed in the field experiment seismograms in Figures 4.13
through 4.18.

The dispersive images resulting from the synthetic seismograms were similar to the dispersive images obtained in the field experiment. At the surface (i.e., depth of 0.0 m), the dispersive images of the synthetic vertical geophones (Figure 6.5(a1)) compared very well to those obtained in the field experiment (Figure 4.15(a)), where the fundamental mode was dominant. Similarities in the dispersive images using synthetic seismograms from the buried FOS (Figure 6.5(c2, c3)) were also observed with regard to the appearance of higher modes measured in the field (Figures 4.5(b, c)). The appearance of higher modes was observed in the dispersive images produced by the buried horizontal synthetic seismograms, i.e., horizontal geophones (Figure 6.5(b2, b3)) and FOS (Figure 6.5(c2, c3)), and not in the buried vertical geophones with depth (Figure 6.5(a2, a3)). A possible explanation for this is that the horizontal displacement vanishes with depth and becomes negative at greater depths, as shown in Figure 2.4 and Figure 2.5, while the vertical motion stays always positive. This occurs at a critical depth, $Z_{critical}$, near the surface. This depth can be calculated using Equation (2.4) for different values of V_R, V_S, V_P, and f_R. For demonstration purposes, assuming a V_S of 165 m/sec (which was about the minimum determined V_S), calculating V_R and V_P as a function of Poisson's ratio of 0.3 and V_S using Equations (2.5) and (2.2) (resulting in $V_R \approx 0.93 V_S$, and $V_P \approx 1.87 V_S$), and assuming a frequency, f_R, of 20 Hz, results in $Z_{critical}$ of about 1.38 m. However, at a higher frequency, f_R, let's say 60 Hz, $Z_{critical}$ will be 0.46 m. This shows that horizontal measurements, such as those measured with horizontal geophones and FOS, at wavelengths related to higher frequencies will vanish at $Z_{critical}$ and become negative below this depth. For this reason the horizontal velocities and strains measured at these depths are likely to be more sensitive to higher modes (related to a different

displacement pattern) and less sensitive to the fundamental mode. Hence, the maximum frequency at which the fundamental mode M0 is observed decreases with increasing sensor depth for both horizontal sensors. This results in a limitation in frequency range in the M0 dispersion curves. These limitations in frequency range associated with the horizontal measurements at depth were observed to be in similar ranges for the dispersion curves obtained from the field experiments and synthetic seismograms. The limitations in frequency ranges for the surface vertical geophones and buried FOS, which are the measurements of interest to this study, are summarized in the following:

1. Surface vertical geophones provided broader frequency ranges from about 5 Hz to above 50 Hz.

2. For the FOS at a depth of 0.5 m, frequencies ranged from about 5 Hz to under 25 Hz.

3. For the FOS as a depth of 1.0 m, the range in frequencies was from about 5 Hz to less than 20 Hz.

Regardless of the limitations in frequency content, a minimum frequency limit of about 5 Hz was achieved for all measurements. This was used to determine the maximum depth of investigation. This depth is based on the maximum wavelength, which is based on the phase velocity at the minimum frequency, as previously discussed in Chapters IV and VI. For this reason, the dispersion curves used for V_S inversion reached similar depths of investigation.

As previously noted, higher frequencies in the dispersion curves differed in ranges for the different sensors and depths, particularly in the horizontal sensors. To resolve V_S at shallow depths, higher frequencies than those measured were determined through

138

theoretical dispersion curves used in the inversion analysis. Theoretical dispersion curves were compared to the measured dispersion curves from the field experiments and synthetic seismograms. Once an acceptable least-square fit of theoretical dispersion curves to the measured dispersion curve was found, the theoretical dispersion curve extended to higher frequencies to define V_S at the shallow depths of the profile. It should be noted that for the site considered, V_S in the shallow portion of the profile was not expected to have significant variation. Thus, the acceptable fit made by the theoretical dispersion curve extending to higher frequencies than those measured did not seem to have an adverse affect in the results. For that reason, although differences in frequency ranges existed, V_S profiles could be obtained from the surface down to the maximum depths.

7.3   Uncertainties in MASW Inversion from the Different Sensors

The MASW inverted shear wave velocity profiles in Figures 4.21 and Figure 6.8 demonstrate that the inversion solution is non-unique. In the field experiments, the MASW V_S profiles were expected to resemble the V_S profile determined from the Seismic Cone Penetration Test (SCPT). In the synthetic seismograms, the MASW V_S profiles were expected to resemble the Finite Element (FE) input V_S profile. Comparing the adequacy of the MASW V_S profiles, V_{S_MASW}, obtained from the different sensors to the expected V_S profiles, $V_{S\_EXPECTED}$, could not be performed qualitatively. An attempt was made to quantify the discrepancies of errors between the V_{S_MASW} and $V_{S\_EXPECTED}$ using the root mean square error (RMSE) of V_S:

$$RMSE_{V_S} = \sqrt{\frac{\sum_{i=1}^{n}\left(V_{S\_EXPECTED}-V_{S\_MASW}\right)^2}{N}}, \qquad (7.1)$$

where N is the total number of inversion points. Since a total of 10 layers was used for all inversions, the number of inversion points, N, was 10.

The $RMSE_{Vs}$ was calculated at the mid-depth of the inverted layers, since inverted values are representative to these depths. Figures 7.1 and 7.2 show the V_{S_MASW} values projected at the mid-depth of the inverted layers for each sensor/depth for the field experiments and synthetic seismograms, respectively. The $RMSE_{Vs}$ accounted for the overall error magnitude of V_S when comparing the V_{S_MASW} with respect to the expected values, $V_{S\_EXPECTED}$, at these corresponding depths. Lower $RMSE_{Vs}$ values are representative of closer agreement of inverted MASW V_S profile to the expected V_S profile. $RMSE_{Vs}$ values were computed independently for the field experiments using the SCPT V_S profile and for the synthetic seismograms using the idealized input V_S profile. As previously stated, these were assumed to be the expected values.
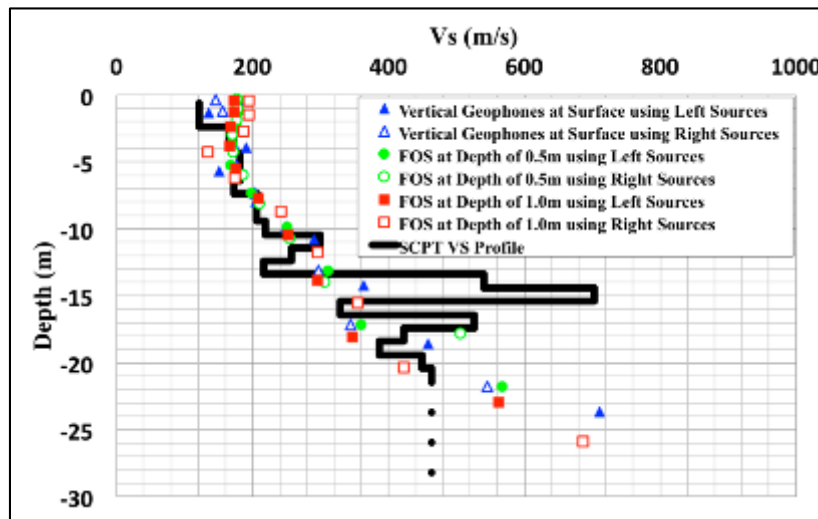
Figure 7.1   Field experiment V_{S_MASW} and $V_{S\_EXPECTED}$ used in $RMSE_{Vs}$ calculations.

V_{S_MASW} at the mid-depths of each layer for the corresponding sensor/depth from results obtained using field experiments seismograms. Also included is the SCPT V_S profile considered to be $V_{S\_EXPECTED}$ for the field experiments.

140
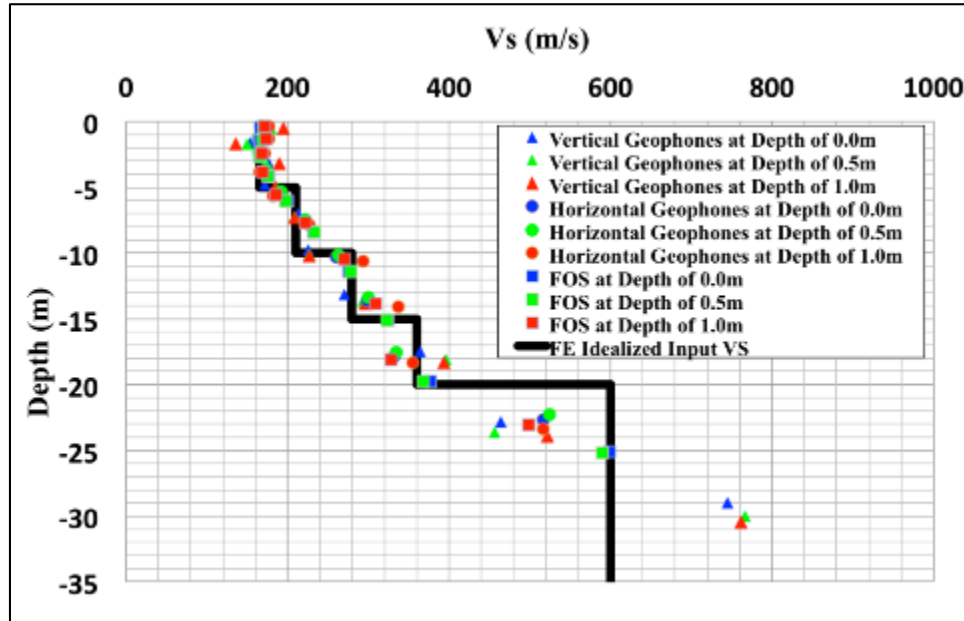
Figure 7.2   Synthetic seismograms V_{S_MASW} and $V_{S\_EXPECTED}$ used in $RMSE_{Vs}$ calculations.

V_{S_MASW} at the mid-depths of each layer for the corresponding sensor/ location from results obtained using synthetic seismograms. Also included is the FE idealized input V_S profile considered to be $V_{S\_EXPECTED}$ for the synthetic seismograms.

RMSE$_{Vs}$ values are summarized in Table 7.1 for the field experiments, grouped according to sensor type, depth, and seismic source offset side combinations. The two seismic source offset sides (i.e., to the left and right side of the spread) were included to verify repeatability of experimental results. Averaging the two seismic source offsets resulted in average RMSE$_{Vs}$ values for each sensor. The results in Table 7.1 show that average RMSE$_{Vs}$ for the different sensors and depths were in the range of about 81 to 87 m/sec. While the RMSE for the FOS were slightly lower, it must be noted that the inversion results depended on the interpretation of the dispersion curve and thus the points selected to represent the dispersion curves may have propagated some variations that influenced the differences in RMSE. The RMSE$_{Vs}$ of field experiment results show

that the FOS at depths of 0.5 m and 1.0 m yield similar errors as those obtained with the vertical geophones at the surface.

Table 7.1   Summary of RMSE$_{Vs}$ values from field experiments V$_S$ inversion.

Sensor	Depth (m)	Seismic Source Side Offset	RMSE$_{Vs}$ (m/sec)	Average RMSE$_{Vs}$ for Sensor Type and Depth (m/sec)
Vertical Geophones	0.0	Left	101.1	**86.8**
		Right	72.4	
FOS	0.5	Left	76.7	**81.1**
		Right	85.4	
	1.0	Left	90.4	**85.8**
		Right	81.3	

RMSE values of V$_S$ obtained using synthetic seismograms are summarized in Table 7.2. These are listed according to sensor type and depth combinations. Corresponding RMSE$_{Vs}$ are shown for each combination. Results show that RMSE for the different sensor and depth combinations varied from sensor to sensor. This might have been caused by the limitation of using one source offset instead of having multiple source offset to obtain a better representation the fundamental mode dispersion curve, as done in the field experiments. RMSE$_{Vs}$ values obtained for the vertical geophones were the highest, and were in the range of about 63 to 73 m/sec. RMSE$_{Vs}$ values associated with the horizontal geophones were lower, in the range of about 27 to 35 m/sec. The values of RMSE$_{Vs}$ for the FOS were in the range of about 15 to 36 m/sec. It must be noted, however, that RMSE values at depths 0.0 and 0.5 m were about 15 m/sec and the RMSE value at the depth of 1.0 m was 36 m/sec. The RMSE$_{Vs}$ values associated with

synthetic seismograms show that the V_{S_MASW} obtained with the FOS had overall less

errors than those obtained with the geophones.

Table 7.2   Summary of RMSE$_{Vs}$ values from synthetic seismograms V_S inversion.

Sensor	Depth (m)	RMSE$_{Vs}$ for Sensor Type and Depth (m/sec)
Vertical Geophones	0.0	**63.3**
	0.5	**73.1**
	1.0	**62.9**
Horizontal Geophones	0.0	**30.1**
	0.5	**27.5**
	1.0	**34.5**
FOS	0.0	**15.2**
	0.5	**15.7**
	1.0	**36.0**

The uncertainties in the RMSE$_{Vs}$ values obtained from the inverted V_S profile

from the field experiments were similar in range, whereas greater differences were

observed using the synthetic seismograms. The differences in uncertainty may have

occurred because:

1. Field experiments were compared against a V_S profile obtained with the

   SCPT that exhibited greater variation than the idealized V_S profile from

   the FE model.

2. Inversion of field experiments was performed with dispersion curves from

   combined dispersive images of multiple offsets while the synthetic

   seismograms only used the dispersion curve from one source offset.

3. FOS seismograms from the field experiments exhibited noise, which although did not provide coherent signals for use in MASW analysis may have added a degree of error to the results.

4. Slight differences in dispersion curve interpretation may have propagated to the V_S inversion.

Other factors may have contributed to the difference in errors; however, although the V_S inversion using the MASW method will be subject to non-unique solutions, the buried FOS achieves comparable errors to surface vertical geophones typically employed for data acquisition.

CHAPTER VIII

CONCLUSIONS AND RECOMMENDATIONS

8.1 Conclusions

The major goal of this study was to demonstrate the feasibility of performing MASW analysis to obtain a 1-D V_s profile using distributed FOS for data acquisition by comparing it to traditional vertical geophones placed at the surface. These results demonstrate the feasibility of using FOS to perform an MASW survey. Through field experiments and synthetic seismograms it was observed that FOS provided comparable results to those obtained using surface vertical geophones. Although differences in dispersive images were observed, the fundamental mode dispersion curves for the lower frequencies were interpreted in a consistent manner. It was also observed that the limitation in the FOS dispersion curves in the upper frequency range (from 20 to 25 Hz) was a result of the FOS being installed at depths were it is suspected that horizontal displacements may have vanished for higher frequencies (i.e., longer wavelengths). Dispersion curves in general were determined for similar lower frequencies (around 5 Hz), achieving thus similar depths of investigation. Shear wave inversion results of the FOS to the geophones were also observed to be comparable in range. Differences were justified by the non-uniqueness of the inversion process. The $RMSE_{Vs}$ values obtained for field experiments and synthetic seismograms show that the errors of the V_s inversion were to the same degree or better than those obtained with vertical geophones.

8.2   Recommendations for Future Research

While this research proved the feasibility of using the MASW method with buried

FOS, further research is needed to investigate other aspects not covered herein such as:

- Other test sites and soil types. In the field experiments and synthetic seismograms, the site was normally dispersive (i.e., increasing stiffness with depth). Other sites may display different behavior and additional effects.

- Multimodal MASW analysis. As observed in the FOS during the experiments and synthetic seismograms, higher modes were evident. Since this study is an initial feasibility study, it was constrained to only using the fundamental mode (M0) for analysis. The potential use of multi modal data to incorporate higher modes can provide better accuracy during the V_S inversion by reducing the number of non-unique solutions (Ivanov et al., 2010).

- Joint Inversion Analysis. While the seismic acquisition for MASW analysis was performed, further investigation can be done to perform seismic refraction, briefly described in section 2.2.2, using buried FOS for joint analysis with MASW (Ivanov et al., 2000; Foti et al., 2015).

- Specialized Fibers. A standard telecommunication fiber cable was used in this study due to its availability to be used for distributed sensing. This was further justified by the difference in cost of standard fiber optic telecommunication cable (2-5 US$/m) when compared to specialized fiber optic cable (15-30 US$/m) (Glisic, 2013). While the feasibility of using standard fiber optic telecommunication cable in the field experiments provided adequate results, they exhibited noise in their signals. Specialized fiber cable configurations with different coatings have been developed for sensing purposes, as used in Daley et al. (2013). These are expected to be less subject to noise since they are intended specifically for high fidelity measurements. The performance of different specialized fiber optic cables for collecting data to perform MASW analysis should be evaluated to determine if data quality could provide improvements in MASW V_S results.

- New technology advancements. The rapid growing fiber optic sensing community is continuously advancing with new Optical Time Domain Reflectometers (OTDRs), fibers and software. As technology improves, other system configurations may provide beneficial advantages in the use of FOS as a sensor with increased resolution and improved sensitivity.

146

REFERENCES

American Society of Civil Engineers, 2006. *ASCE/SEI 41-06 - Seismic Rehabilitation of Existing Buildings*. ASCE STANDARD. Reston, VA: American Society of Civil Engineers.

Anderson, N. & Thitimakorn, T., 2004. *A 2-D MASW Shear-Wave Velocity Profile Along a Test Segment of Interstate I-70, St. Louis, Missouri*. Technical Report. Jefferson City, MO: Missouri Department of Transportation Research, Development and Technology Division University of Missouri-Rolla.

ASTM, 2014. *D7400-14: Standard Test Methods for Downhole Seismic Testing*. ASTM Std. West Conshohocken, PA: American Standard for Testing and Materials International.

Ballard, R.F., 1964. *Determination of Soil Shear moduli at Depth by In Situ Vibratory Techniques*. Miscellaneous paper No.4-691. Vicksburg, MS: Waterways Experiment Station.

Bao, X. & Chen, L., 2012. Recent Progress in Distributed Fiber Optic Sensors. *Sensors*, 12, pp.8601-39.

Bowles, J.E., 1995. *Foundation Analysis and Design*. 5th ed. New York: McGraw-Hill.

Brandenber, S.J., Ballana, N. & Shantz, T., 2010. *Shear Wave Velocity as a Statistical Function of Stadard Penetration Test Resistance and Vertical Effective Stress at Caltrans Bridge Sites*. Technical Report. Davis: Pacific Earthquake Engineering Research Center University of California.

Building Seismic Safety Council, 2003. NEHRP Recommended Provisions for Seismic Regulations for New Buildings and Other Structures (FEMA 450). In *Chapter 3*. Federal Emergency Management Agency (FEMA). pp.17–49.

COMSOL, 2012. Structural Mechanics Module User's Guide. *Version COMSOL 4.3a*.

Cooley, J.W. & Tukey, J.W., 1965. An Algorithm for the Machine Calculation of Complex Fourier Series. *Mathematics of Computation*, 19, pp.297-301.

Courant, R., Friedrichs, K. & Lewy, H., 1967 [Republished from 1928]. On the Partial Difference Equations of Mathematical Physics. *IBM Journal of Research and Development*, 11 (2), pp.215-234.

Corning, 2015. *Product Specification 024EC5-14100D53_NAFTA_AEN*. [Online] Available at: http://catalog.corning.com/opcomm/en-US/catalog/ProductDetails .aspx?cid=ribbon_outdoor_cables_web&pid=9059&vid=9060&rot=fiber_optic_ cables_web&context=;CCS_Global_Web_Catalog;fiber_optic_cables_web; outdoor_cables_web;ribbon_outdoor_cables_web;ribbon_outdoor_cables_web; &rooot=products [Accessed 01 May 2015]. SST-Ribbon™ Single-Tube, Gel-Free, Armored Cable, 24 F, Single-mode (OS2).

Costley, R.D., Parker, M.W., Ketcham, S.A, Hathaway, K.K., Galan-Comas, G., Milburn, T.W., Smith, E.W., Wadman, H.M., Simms, J.E., and Folks, W.R., Seismic Testing on the Linear Sensor Test Bed at the Field Research Facility, ERDC/GSL TR-XX-XX. Vicksburg, MS: US Army Engineer Research and Development Center. In progress.

Daley, T.D. et al., 2013. Field testing of fiber-optic distributed acoustic sensing (DAS) for subsurface seismic monitoring. *The Leading Edge*, 32(6), pp.699-706.

Dickenson, S.E., 1994. *Dynamic Response of Soft and Deep Cohesive Soils during the Loma Prieta Earthquake of October 17, 1989*. PhD Thesis. Dept. of Civil and Environmental Engineering, University of California, Berkeley, CA.

E-Fiber Optic Network (EFON), 2015. *Fiber Optic Cable Tutorial*. [Online] Available at: http://www.efoncable.com/showfaq.asp?id=18 [Accessed 01 May 2015].

EPI Group, 2015. *Images from EPI projects around the world – Top 5*. [Online] Available at: http://epi.co.uk/2013/03/images-from-epi-projects-around-the-world-top-5/ [Accessed 01 May 2015].

Foti, S., 2000. *Multistation Methods for Geotechnical Characterization using Surface Waves*. PhD Thesis. Torino, Italy: Politecnico di Torino.

Foti, S., Lai, C.G., RIx, G.J. & Strobbia, C., 2015. *Surface Wave Methods for Near-Surface Site Characterization*. Boca Raton, FL, USA: Taylor & Francis Group, LLC.

Gazetas, G. & Yegian, M.K., 1979. Shear and Rayleigh Waves in Soil Dynamics. *Journal of the Geotechnical Engineering Division*, 105(12), pp.1455-70.

Glisic, B., 2013. *Distributed Fiber Optic Sensing Technologies and Applications – An Overview*. ACI Special Publication, SP-292. American Concrete Institute.

Grau, R.W., 1993. *Effects of Variable Tire Pressure on Road Surfacings-Volume I: Design, Construction, Behavior Under Traffic, and Test Results*. Technical Report GL-93-20. Vicksburg, MS: U S Department of Agriculture Forest Service Waterways Experiment Station.

Green, J.W. & Bograd, M., 1973. *Environmental Geology of Pocahontas, Clinton, Raymond, and Brownsville Quadrangle, Hinds County, Mississippi.* Mississippi Geological Survey, Environmenal Geology, Series No.1

Holtz, R.D. & Kovacs, W.D., 1981. *An Introduction to Geotechnical Engineering.* Englewood Cliffs, New Jersey: Prentice Hall.

Hons, M.S., 2008. *Seismic sensing: Comparison of geophones and accelerometers using laboratory and field data.* MS Thesis. Calgary, Alberta: University of Calgary.

Hui, R. & O'Sullivan, M., 2009. *Fiber Optic Measurement Techniques.* Burlington, MA: Elsevier Inc.

Ivanov, J., Park, C.B., Miller, R.D., Xia, J., Hunter, J.A., Good, R.L. & Burns, R.A, 2000. Joint analysis of surface-wave and refraction events from river-bottom sediments. In *Technical Program Expanded Abstracts, SEG, 70th Annual Meeting.* Calgary, Alberta, Canada, 2000, pp.1307-1310.

Ivanov, J., Miller, R.D., Xia, J. & Peterie, S, 2010. Multi-mode inversion of multi-channel analysis of surface waves (MASW) dispersion curves and high-resolution linear radon transform (HRLRT). In *Technical Program Expanded Abstracts, SEG, 80th Annual Meeting.* Denver, Colorado, 2010, pp.1902-1907.

Jones, R., 1958. In-situ Measurement of the Dynamic Properties of Soil by Vibration Methods. *Géotechnique*, 8(1), pp.1-21.

Jones, R., 1962. Surface wave technique for measuring the elastic properties and thickness of roads - theoretical development. *British Journal of Applied Physics*, 13(1), pp.21-29.

Kramer, S.L., 1996. *Geotechnical Earthquake Engineeering.* Upper Sadle River, New Jersey: Prentice Hall.

Krinitzsky, E.L. & Turnbull, W.J., 1967. Loess Deposits of Mississippi. *Geological Society of America Special Papers*, 94, pp.1-62.

Lamb, H., 1904. On the Propagation of Tremors over the Surface of an Elastic Soil. *Philosophical Transactions of the Royal Society, Series A, Containing Papers of a Mathematical or Physical Character*, 203, pp.1-42.

Lin, S., 2014. *Advancements in active surface wave methods- modeling, testing, and inversion.* PhD Thesis. Ames, Iowa: Iowa State University.

Mayne, P.W., 2012. Geotechnical Site Characterization in the Year 2012 and Beyond. In *GeoCongress 2012-Geotechnical Engineering State of the Art and Practice.* Oakland, CA, 2012. ASCE.

McMehan, G.A. & Yedlin, M.J., 1981. Analysis of Dispersive Waves by Wave Field Transformation. *Geophysics*, 46(6), pp.869-74.

Miller, R.D. & Ivanov, J., 2005. *Seismic Tests on IBWC Levees: Weslaco, Texas*. Lawrence, KS: University of Kansas.

Miller, R.D., Ivanov, J., Hartung, S. & Block, L., 2004. Seismic Investigation of a Sinkhole on Clearwater Dam. In *SAGEEP 2004*., 2004. Environment and Engineering Geophysical Society.

Miller, R.D., Xia, J., Park, C.B. & Ivanov, J., 2000. Shear Wave Velocity Field from Surface Waves to Detect Anomalies in the Subsurface. In *Proceedings of the First International Conference on the Application of Geophysical Methodologies to Transportation Facilities and Infrastructure*. St. Louis, MO, 2000.

Mitschke, F., 2010. *Fiber Optics: Physics and Technology*. Springer-Verlag Berlin Heidelberg.

Murphy, L. & Albertson, P.E., 1996. Engineering Geological Geographical Information System of the Waterways Experiement Station. *Mississippi Geology*, June. pp.25-39.

Nazarian, S., 2012. Shear Wave Velocity Profiling with Surface Wave Methods. In *GeoCongress 2012-Geotechnical Engineering State of the Art and Practice*. Oakland, California, United States, 2012. ASCE.

Nazarian, S. & Stokoe, K.H., 1983. *Evaluation of Moduli and Thickness of Pavement Systems by Spectral Analysis of Surface Waves Method*. Research Project. Austin, TX: Texas State Department of Highways and Public Transportation The University of Texas at Austin.

Nolet, G. & Panza, G.F., 1976. Array Analysis of Seismic Surface Waves: Limits and Possibilities. *Pure and Applied Geophysics*, 114(5), pp.775-90.

Optiphase, Inc., 2012. *CR3 Prototype System User Manual*. Optiphase.

Park, C.B., 2005. Shear- Wave Velocity (Vs) Profiling by Surface Wave (MASW) Method. In *Symposium on the Application of Geophysics to Engineering and Environmental Problems (SAGEEP) 2005*. Atlanta, GA, 2005. Environment and Engineering Geophysical Society.

Park, C.B., 2011. Imaging Dispersion of MASW Data—Full vs. Selective Offset Scheme. *Journal of Environmental Engineering and Geophysics*, 16(1), pp.13-23.

Park, C.B. & Carnevale, M., 2010. Optimum MASW Survey - Revisit after a Decade of Use. In *GeoFlorida 2010: Advances in Analysis, Modeling & Design*., 2010. ASCE.

Park, C.B., Miller, R.D. & Miura, H., 2002. Optimum field parameters of an MASW survey. In *SEG-Japan 2012*. Tokyo, Japan, 2002.

Park, C.B., Miller, R.D. & Xia, J., 1997. *Multi-channel analysis of surface waves (MASW)--"A summary report of technical aspects, experimental results, and perspective"*. University of Kansas. Kansas Geological Survey Open-file Report 97-10.

Park, C.B., Miller, R.D. & Xia, J., 1998. Imaging dispersion curves of surface waves on multi-channel record. In *Technical Program with Biographies, SEG, 68th Annual Meeting*. New Orleans, LA, 1998. SEG.

Park, C.B., Miller, R.D. & Xia, J., 1999. Multi-channel analysis of surface waves (MASW). *Geophysics*, 64(3), pp.800-08.

Park, C.B., Miller, R.D. & Xia, J., 2001. Offset and Resolution of Dispersion Curve in Multichannel Analysis of Surface Waves (MASW). In *Symposium on the Application of Geophysics to Engineering and Environmental Problems 2001*. Denver, Co, 2001. Environment and Engineering Geophysical Society.

Park, C.B., Miller, R.D., Xia, J. & Ivanov, J., 2000. Multichannel seismic surface-wave methods for geotechnical applications. In *Proceedings of the First International Conference on the Application of Geophysical Methodologies to Transportation Facilities and Infrastructure*. St. Louis, MO, 2000. Geophysics 2000.

Penumadu, D. & Park, C.B., 2005. Multichannel Analysis of Surface Wave (MASW) Method for Geotechnical Site Characterization. *Earthquake Engineering and Soil Dynamics*, pp.1-10.

Pullan, S. E., 1990, Recommended standard for seismic (/radar) files in the personal computer environment: Geophysics, 55, no. 09, 1260-1271.

Rayleigh, L., 1885. On Waves Propagated Along the Plane Surface of an Elastic Solid. *Proceedings of the London Mathematical Society*, 1-17, pp.4-11.

Richart, F.E., Hall, J.R.J. & Woods, R.D., 1970. *Vibration of Soils and Foundations*. Englewood Cliffs, NJ: Prentice-Hall, Inc.

Rinaldi, V.A., Zeballos, M.E. & Rocca , R.J., 2006. Geotechnical characterization and behaviour of Argentinean collapsible loess. In *Proceedings of the Second International Workshop on Characterisation and Engineering Properties of Natural Soils.*, 2006. Taylor & Francis 2006.

Rix, G.J., Stokoe, K.H. & Roesset, J.M., 1991. *Experimental Study of Factors Affecting the Spectral-Analysis-of-Surface-Waves Method*. Research Report Number 1123-5 (FHWA/TX-91+1123-5). Austin, TX: Texas State Department of Highways and Public Transportation The University of Texas-Austin.

Ryden, N., Park, C.B., Ulriksen, P. & Miller, R.D., 2004. Multimodal Approach to Seismic Pavement Testing. *Journal of Geotechnical and Geoenvironmental Engineering*, 130(6), pp.636-45.

Seed, H. B. & Idriss, I. M., 1981. *Evaluation of liquefaction potential sand deposits based on observation of performance in previous earthquakes*. ASCE National Convention (MO), pp. 81–544.

Stokoe, K.H. & Santamarina, J.C., 2000. Seismic-Wave-Based Testing in Geotechnical Engineering. In *International Conference on Geotechnical and Geological Engineering, GeoEng 2000*. Melbourne, Australia, 2000. Australian Geomechanics Society.

Strobbia, C., 2003. *Surface Wave Methods: Acquisition, Processing and inversion*. PhD Thesis. Torino, Italy: Politecnico Di Torino.

Udd, E., 1990. *Fiber Optic Sensors: An Introduction for Engineers and Scientists*. New York: John Wiley & Sons, Inc.

Wair, B.R., DeJong, J.T. & Shantz, T., 2012. *Guidelines for Estimation of Shear Wave Velocity Profiles*. Guidelines. Davis: Pacific Earthquake Engineering Research Center University of California.

Webster, P., Wall, J., Perkins, C. & Molenaar, M., 2013. Micro-Seismic Detection using Distributed Acoustic Sensing. In *2013 SEG Annual Meeting*. Houston, Texas, 2013. Society of Exploration Geophysicists.

Williams, R.T. & Pnemadu, D., 2011. Multichannel Analysis of Surface Waves (MASW) at the National Geotechnical Engineering Site at Texas A&M University (NGES/TAMU). In *Geo-Risk 2011- Geotechnical Risk Assessment and Management*. Atlanta, GA, 2011. ASCE.

Xia, J., Miller, R.D. & Park, C.B., 1999. Estimation of Near-Surface Shear-Wave Velocity by Inversion of Rayleigh waves. *Geophysics*, 64(3), pp.691-700.

Xia, J., Miller, R.D. & Park, C.B., 2000. Construction of a 2-D Vertical Shear-Wave Velocity Field by the Multichannel Analysis of Surface Wave Technique. In *Proceedings of the Symposium on the Application of Geophysics to Engineering and Environmental Problems (SAGEEP)*. Arlington, Va., 2000.

Xia, J., Xu, Y. & Miller, R.D., 2007. Generating an Image of Dispersive Energy by Frequency Decomposition and Slant Stacking. *Pure and Applied Geophysics*, 164(5), pp.941-56.

APPENDIX A

MATLAB® SCRIPTS

A.1 CR3toSEG2.m.

The FOS data was in the CR3 proprietary format corresponding to Optiphase, Inc. and needed to be filtered and converted to SEG2 format to be able to be imported into SurfSeis®. A band pass filter from 5 to 100 Hz was used. This frequency range covers the frequencies of interest that are excited with the sledgehammer as the seismic source, as well as the typical frequency range used for MASW analysis. The following script shows how this was performed.

```
% -----------------------------------------------------------------------
%
%   Program:       CR3toSEG2.m
%   Date created: 2015/01/31
%   Last changed: 2015/07/11
%   Description:   Converts CR3 proprietary FOS format into seg-2 format
%   Author:        Gustavo Galan-Comas
%   Dependencies: c32readin.m
%                     (Not available for public release-
%                      Includes Proprietary format from Optiphase, Inc.)
%                  fn_writeseg2_mod.m
%                      (Modified from fn_writeseg2.m (Lamb, 2011)
%   References:    Lamb, A., 2011, fn_writeseg2.m (Matlab function
%                     developed to write a SEG2 formatted file to read
%                     into rayfract):
%                     (http://rayfract.com/pub/fn_writeseg2.m)
%                  Pullan, S. E., 1990, Recommended standard for
%                     seismic (/radar) files in the personal computer
%                     environment: Geophysics, 55, no. 09, 1260-1271.
%                  SegyMAT code: http://segymat.sourceforge.net/
%
% -----------------------------------------------------------------------

clear all; clc

%% User Input parameters
% -------------------------------------
%Predetermined FOS zones corresponding to MASW spread were included
%in function 'cr3readin.m'
Sensor={'FOS_0.5m','FOS_1.0m'};

%Seismic Source Station
SourceStation=1000;

% Filter cutoffs
hp = 5;   % Hz, high pass cutoff
lp = 100; % Hz, low pass cutoff

%% Select file to convert and process
% -------------------------------------
[ file_name, directory_name ] = uigetfile( '*.CR3P.data' );
```

154

```
for FOSi=1:2 %Get data from both FOS depths
%% Read in CR3 file and import raw data
% ----------------------------------
% (Function Not shown due proprietary information)
% ----------------------------------
[ t,FOSdata_raw, samplefreq, FOSdx, FOSzones, RECORDnum ] ...
    = cr3readin( file_name, directory_name, Sensor{FOSi});

%% Apply Band Pass Filter
% ----------------------------------
    Wn = [0 0];
    Wn(1) = hp/(samplefreq/2);  % High Pass cutoff
    Wn(2) = lp/(samplefreq/2);  % Low Pass cutoff
    [b,a] = cheby1(4,0.5,Wn);

FOSdata_filt = filter( b, a, FOSdata_raw, [], 1 );

%% Convert CR3 imported data into Seg-2 file
% ----------------------------------
    %% Inputs for SEG2 required
    %Sample rate
        smrate= 1 / samplefreq;  %secs
    %Number of channels/traces
        c=length(FOSzones);
    %Number of samples per trace
        ns= length(t);
    %Trace Data
        Data=FOSdata_filt;
    %H=SegTraceHeaders structure
        for i=1:c
            field1='DelayRecordingTime';    value1=0;  %No Delay
             offset=1; %starting station of 1st Receiver
             dx=FOSdx;
            field2='GroupX'; value2=offset+dx*(i-1);  %Receiver Location
            field3='cdp'; value3=1; %Common Depth Point Option(Default)
            field4='cdpTrace';   value4=i; %Channel Number
            field5='EnergySourcePoint'; value5=RECORDnum ;
                %'Shot number' - Set to Record number, since shot
                  records were different for every shot
            field6='SourceX';value6=SourceStation; %'Source Station no.'
            field7='FieldRecord'; value7=RECORDnum;  %'Record number'

            H(i)=struct(field1,value1,field2,value2,field3,value3,...
             field4,value4,field5,value5,field6,value6,field7,value7);
        end
    %Path
        %path= directory_name;




    %% Call function 'fn_writeseg2_vFOS.m' to get data into Seg-2 format
    fn_writeseg2_mod(Data,smrate,c,ns,H,directory_name,Sensor{FOSi});
    %*Note: File will save as: "[RECORDnumber]_[Sensor].sg2"

end

% -------------------------------------------------------------------
```

155

A.2   ASCIItoSEG2.m.

Synthetic data from the different sensors extracted from the finite element

analysis was stored as CSV data files in ASCII format. These needed to be converted to

the SEG-2 binary format to be able to be imported into SurfSeis®. The following script

shows how this was performed.

```
% -------------------------------------------------------------------------
%
%    Program:       ASCIItoSEG2.m
%    Date created: 2015/02/15
%    Last changed: 2015/07/20
%    Description:   Converts CSV files from synthetic seismograms into
%                      SEG-2 binary format
%    Author:        Gustavo Galan-Comas
%    Dependencies: fn_writeseg2_mod.m
%                      (Modified from fn_writeseg2.m (Lamb, 2011)
%    References:    Lamb, A., 2011, fn_writeseg2.m (Matlab function
%                      developed to write a SEG2 formatted file to read
%                      into rayfract):
%                      (http://rayfract.com/pub/fn_writeseg2.m)
%                   Pullan, S. E., 1990, Recommended standard for
%                      seismic (/radar) files in the personal computer
%                      environment: Geophysics, 55, no. 09, 1260-1271.
%                   SegyMAT code: http://segymat.sourceforge.net/
%
% -------------------------------------------------------------------------

clear all; clc

%% User Input parameters
% ------------------------------------
    c=36; %number of traces
    dx=2; %Sensor Spacing in m
    SourceStation=999.75;
    RECORDnum=1000;


%% Select file to convert
% ------------------------------------
[ file_name, directory_name ] = uigetfile( '*.csv' );
% Get Sensor Name from filename string
Sensor=[file_name(65:end-4),'_SynthSeis'];

%% Read and store data in temp data array
% ------------------------------------
temp= csvread(strcat(directory_name,file_name),6,0);

%% Parse temp data array to get values
% ------------------------------------
    %Time Vector
    t=temp(:,1);

    % Trace Data (% Data = recorded data for each trace in ASCII format)
    Data=temp(:,2:(c+1));
```

156

```
%% Convert CR3 imported data into Seg-2 file
% ------------------------------------
   %% Inputs for SEG2 required
    %Sample rate
        smrate=t(100)-t(99);  %secs
    %Number of channels/traces
        %c=c;
    %Number of samples per trace
        ns= length(t);
    %Trace Data
        %Data=Data;
    %H=SegTraceHeaders structure
        for i=1:c
            field1='DelayRecordingTime';   value1=0;  %No Delay
             offset=1; %starting station of 1st Receiver
             %dx=dx;
            field2='GroupX'; value2=offset+dx*(i-1);  %Receiver Location
            field3='cdp';   value3=1; %Common Depth Point Option(Default)
            field4='cdpTrace';   value4=i; %Channel Number
            field5='EnergySourcePoint'; value5=RECORDnum ;
                    %'Shot number' - Set to Record number, since only
                    %one shot was simulated.
            field6='SourceX';value6=SourceStation; %'Source Station no.'
            field7='FieldRecord'; value7=RECORDnum;  %'Record number'

            H(i)=struct(field1,value1,field2,value2,field3,value3,...
               field4,value4,field5,value5,field6,value6,field7,value7);
        end
   %Path
        %path= directory_name;

   %% Call function 'fn_writeseg2_vFOS.m' to get data into Seg-2 format
    fn_writeseg2_mod(Data,smrate,c,ns,H,directory_name,Sensor);
    %*Note: File will save as: "[RECORDnumber]_[Sensor].sg2"

% -----------------------------------------------------------------------
```

A.3   Function: fn_writeseg2_mod.m

This function was called in the main programs to write data in the standard SEG-2

binary format. The function consisted of minor edits to the original function

fn_writeseg2.m developed by Andrew Lamb (2011).

```
% -----------------------------------------------------------------------
function [] = fn_writeseg2_mod(Data,smrate,c,ns,H,path,Sensor)
% Developed using:
%  fn_writeseg2.m version 1.1 created by Andrew Lamb, BSU, August 2011
%   Edited by: Gustavo Galan-Comas
%   Edits include:
%     Sensor string input for filenaming purposes for the diff sensors
%     tds{13} changed from ['SOURCE VIBROSEIS'] to ['SOURCE HAMMER']
% References:
%   Pullan, S. E., Recommended standard for seismic (/radar) data files
%   in the personal computer environment. Geophysics 55, 1260-1271
%   (1990)
%
```

157

```
%% Function Input Parameters
% Data = recorded data for each trace in the SegyMAT format
% smrate = sample rate
% c = number of channels/traces
% ns = number of samples per trace
% H=SegyTraceHeaders structure created by SegyMAT's ReadSegy command
% path = path to write seg2 file according to definition by Pullan 1990
% Sensor = FOS_0.5m or FOS_1d0m used for output filename
%
%% Function Output
% seg2 file with 'RECORDnumber_Sensor.sg2' as the filename


% ----------------------------------------------------------------------


%% Filename Output
fid=fopen([path,num2str([H(1).EnergySourcePoint]),'_',...
                  num2str(Sensor),'.sg2'],'w');

%% SEG2 file format schematic (example)
% Schematic is based on example using c=48, ns=150
% and strings with * as recommended by Pullan 1990.
% These strings are 'TRACE_SORT AS_ACQUIRED' and 'UNITS METERS' for the
% File Descriptor Block (total 44 bytes) and DELAY, RECEIVER_LOCATION
% and SAMPLE_INTERVAL for the Trace Descriptor Block (total 64 bytes)
% -----------------------------------------
% |*******FILE DESCRIPTOR BLOCK*********|
% |             MAIN HEADERS             |
% |          bytes 1 - 16 (16)           |
% |               RESERVED               |
% |              17 - 32 (16)            |
% |         TRACE POINTER SUB-BLOCK      |
% |              33 - 224 (192)          |
% |    assumes 4 bytes/trace & 48 traces |
% |                STRINGS               |
% |              225 - 268 (44)          |
% |              [TOTAL=268]             |
% -----------------------------------------
% -----------------------------------------
% |******TRACE DESCRIPTOR BLOCK 1*******|
% |             MAIN HEADERS             |
% |          bytes 269 -284 (16)         |
% |               RESERVED               |
% |             285 - 300 (16)           |
% |                STRINGS               |
% |             301 - 364 (64)           |
% |             [SUBTOTAL=96]            |
% -----------------------------------------
% -----------------------------------------
% |************DATA BLOCK 1************|
% |             365 - 964 (600)          |
% |             [SUBTOTAL=600]           |
% -----------------------------------------
% |         [BLOCK 1 TOTAL=696]          |
% |||||||||||||||||||||||||||||||||||||||||
% TRACE DESCRIPTOR AND DATA BLOCKS 2 - 47
% |||||||||||||||||||||||||||||||||||||||||
% -----------------------------------------
% |******TRACE DESCRIPTOR BLOCK 48******|
% |             MAIN HEADERS             |
% |       bytes 32981 - 32996 (16)       |
% |               RESERVED               |
% |            32997 - 33012 (16)        |
```

```
% |              STRINGS            |
% |         33013 - 33076 (64)      |
% |            [SUBTOTAL=96]         |
% ----------------------------------------
% ----------------------------------------
% |***********DATA BLOCK 48***********|
% |         33077 - 33676 (600)     |
% |            [SUBTOTAL=600]        |
% ----------------------------------------
% FILE SIZE = 33,676 bytes (as written to disk)

%% Prepare Strings for File Descriptor Block
fds1='TRACE_SORT AS_ACQUIRED'; %File Descriptor String 1
fds2='UNITS_METERS';          %File Descriptor String 2

%Combined length of strings including the two empty bytes required at
%the end of the string sub-block to mark the end
fdslen=length(fds1)+3+length(fds2)+3+2;

%Checks how many bytes are needed to pad file descriptor block
%to a division of 4
fdspad=4-((fdslen)/4-floor((fdslen)/4))/0.25;
if fdspad==4
    fdspad=0; % no need to pad
end

%% Prepare Strings for Trace Descriptor Block
% This section estimates the lengths of each string in the Trace
% Descriptor Block and assigns an initial value
i=1; %counter
tds{1}=['DELAY ' sprintf('%8.4f',[H(i).DelayRecordingTime])];
tds{2}=['RECEIVER_LOCATION ' sprintf('%15.3f',[H(i).GroupX])];
tds{3}=['SAMPLE_INTERVAL ' sprintf('%0.4f',smrate)];
tds{4}=['CDP_NUMBER ' sprintf('%08d',[H(i).cdp])];
tds{5}=['CDP_TRACE ' sprintf('%08d',[H(i).cdpTrace])];
tds{6}=['RECEIVER_GEOMETRY ' sprintf('%15.3f',[H(i).GroupX])];
tds{7}=['SHOT_SEQUENCE_NUMBER '
sprintf('%08d',[H(i).EnergySourcePoint])];
tds{8}=['SOURCE_LOCATION ' sprintf('%15.3f',[H(i).EnergySourcePoint])];
tds{9}=['SOURCE_GEOMETRY ' sprintf('%15.3f',[H(i).SourceX]*0)];
tds{10}=['SOURCE_STATION_NUMBER ' sprintf('%08d',[H(i).SourceX])];
tds{11}=['CHANNEL_NUMBER ' sprintf('%08d',[H(i).cdpTrace])];
tds{12}=['RAW_RECORD ' sprintf('%08d',[H(i).FieldRecord])];
tds{13}=['SOURCE HAMMER'];

%Combined length of strings including the two %empty bytes required at
%the end of the string sub-block to mark the end
tdslen=sum(cellfun(@length,tds))+3*size(tds,2)+2;

%Checks how many bytes are needed to pad trace descriptor block
%to a division of 4
tdspad=4-((tdslen)/4-floor((tdslen)/4))/0.25;
if tdspad==4
    tdspad=0; % no need to pad
end

%% Write FILE DESCRIPTOR BLOCK
% This section writes the File Descriptor Block using the definitions
%from the SEG2 standard definition (Pullan 1990).
% Write Main Headers
fwrite(fid, hex2dec('3A55'), 'uint16', 0, 'n'); %File descriptor 0-1 55
                                      %1st => PC
```

```
fwrite(fid, 1, 'uint16', 0, 'n'); %Revision number. 2-3 int16
fwrite(fid, c*4, 'uint16', 0, 'n'); %Size of Trace Pointer SubBlock.4-5
fwrite(fid, c, 'uint16', 0, 'n'); %No. of traces in this file 6-7
fwrite(fid, hex2dec('01'), 'uint8', 0, 'n'); %Size of string term. 8
fwrite(fid, 0, 'uint8', 0, 'n'); %Null. 9 int8
fwrite(fid, hex2dec('02'), 'uint8', 1, 'n'); %Size of string term. 11
fwrite(fid, hex2dec('0A'), 'uint8', 0, 'n'); %1st line of terminator
                                                          %(LF). 12
fwrite(fid, hex2dec('0D'), 'uint8', 0, 'n'); %1st line of terminator
                                                          %(CR). 13


%Write trace pointer sub-blocks. These give byte location of trace = i
for i =1:c
    if i==1 % When c==1 the pointer skips over the RESERVED Bytes
        fwrite(fid, 32+(4*(c))+fdslen+fdspad ...
                        +((32+tdslen+tdspad+(ns*4))* ...
                        (i-1)), 'ulong', 18, 'n');
    else  %Writes byte location of remaining trace pointer sub-blocks
        fwrite(fid, 32+(4*(c))+fdslen+fdspad ...
                        +((32+tdslen+tdspad+(ns*4))*...
                        (i-1)), 'ulong', 0, 'n');
    end
end

% Write Strings for File Descriptor block
% Write TRACE_SORT string
fwrite(fid, length(fds1)+3, 'uint16' ,0,'n');
fwrite(fid, fds1,'char',0,'n');
fwrite(fid, 0, 'uint8', 0,'n');
% Write UNITS string
fwrite(fid, length(fds2)+3, 'uint16' ,0,'n');
fwrite(fid, fds2,'char',0,'n');
fwrite(fid, 0, 'uint8', 0,'n');

%% Write TRACE DESCRIPTOR and DATA BLOCK loops
% Write Main Headers
for i=1:c
    % Reassign trace descriptor strings with i value
    tds{1}=['DELAY ' sprintf('%8.4f',[H(i).DelayRecordingTime])];
    tds{2}=['RECEIVER_LOCATION ' sprintf('%15.3f',[H(i).GroupX])];
    tds{3}=['SAMPLE_INTERVAL ' sprintf('%0.4f',smrate)];
    tds{4}=['CDP_NUMBER ' sprintf('%08d',[H(i).cdp])];
    tds{5}=['CDP_TRACE ' sprintf('%08d',[H(i).cdpTrace])];
    tds{6}=['RECEIVER_GEOMETRY ' sprintf('%15.3f',[H(i).GroupX])];
    tds{7}=['SHOT_SEQUENCE_NUMBER '
sprintf('%08d',[H(i).EnergySourcePoint])];
    tds{8}=['SOURCE_LOCATION '
sprintf('%15.3f',[H(i).EnergySourcePoint])];
    tds{9}=['SOURCE_GEOMETRY ' sprintf('%15.3f',[H(i).SourceX]*0)];
    tds{10}=['SOURCE_STATION_NUMBER ' sprintf('%08d',[H(i).SourceX])];
    tds{11}=['CHANNEL_NUMBER ' sprintf('%08d',[H(i).cdpTrace])];
    tds{12}=['RAW_RECORD ' sprintf('%08d',[H(i).FieldRecord])];
    tds{13}=['SOURCE HAMMER'];

    if i==1
        skip=2+fdspad; %Number of bytes to skip to ensure file
                        %descriptor block is a division of 4
    else
        skip=0; %No skipping is required on first byte of Trace
                    %descriptor block has been written
    end
```

160

```matlab
    fwrite(fid, hex2dec('4422'), 'uint16', skip, 'n'); %Trace
                                              %descriptor 0-1
    fwrite(fid, 32+tdslen+tdspad, 'uint16', 0, 'n'); %X=Size of this
                                              %block 2-3
    fwrite(fid, ns*4, 'ulong', 0, 'n'); %Y=Size of data block 4-7
    fwrite(fid, ns, 'ulong', 0, 'n'); %NS=Number of samples in data
                                  %block 8-11
    fwrite(fid, hex2dec('04'), 'uint8', 0, 'n'); %Data format

    %Write Strings for Trace Descriptor block
    for k=1:size(tds,2)
        if k==1
            skip=19; %This skips over the 20 reserve bytes before
                        %writing strings
        else
            skip=0;
        end
        fwrite(fid, length(tds{k})+3, 'uint16' ,skip,'n');%Skip 20
                                              %reserved bytes
        fwrite(fid, tds{k}, 'char',0,'n');
        fwrite(fid, 0, 'uint8', 0,'n');
    end

    % DATA BLOCK loop
    for j=1:ns
        if j==1
            fwrite(fid, Data(j,i), 'float32', 2+tdspad, 'n');
        else
            fwrite(fid, Data(j,i), 'float32', 0, 'n');
        end
    end
end
fclose(fid);

% ----------------------------------------------------------------------
```

APPENDIX B

CONE PENETROMETER TEST (CPT) DATA OBTAINED DURING SEISMIC CONE

PENETROMETER TEST (SCPT)

B.1   Cone Penetrometer Test (CPT) Data Obtained During SCPT Tests

Stops were made during the SCPT test to perform soundings and attach new rods. As the push rod was advanced further with depth, CPT data was collected. The results are shown in Figure B1. Of relevance to this study is the difference in higher tip resistance measured at depths of about 13 to 15 m indicating thin sand layers. Based on the expected geology at these depths, it could have been caused by the Catahoula Formation, which may have existing sandstone layers (Murphy & Albertson, 1996). These will yield higher stiffness and thus higher shear wave velocities, which relate to the variations observed in the SCPT results in Figure 4.25.
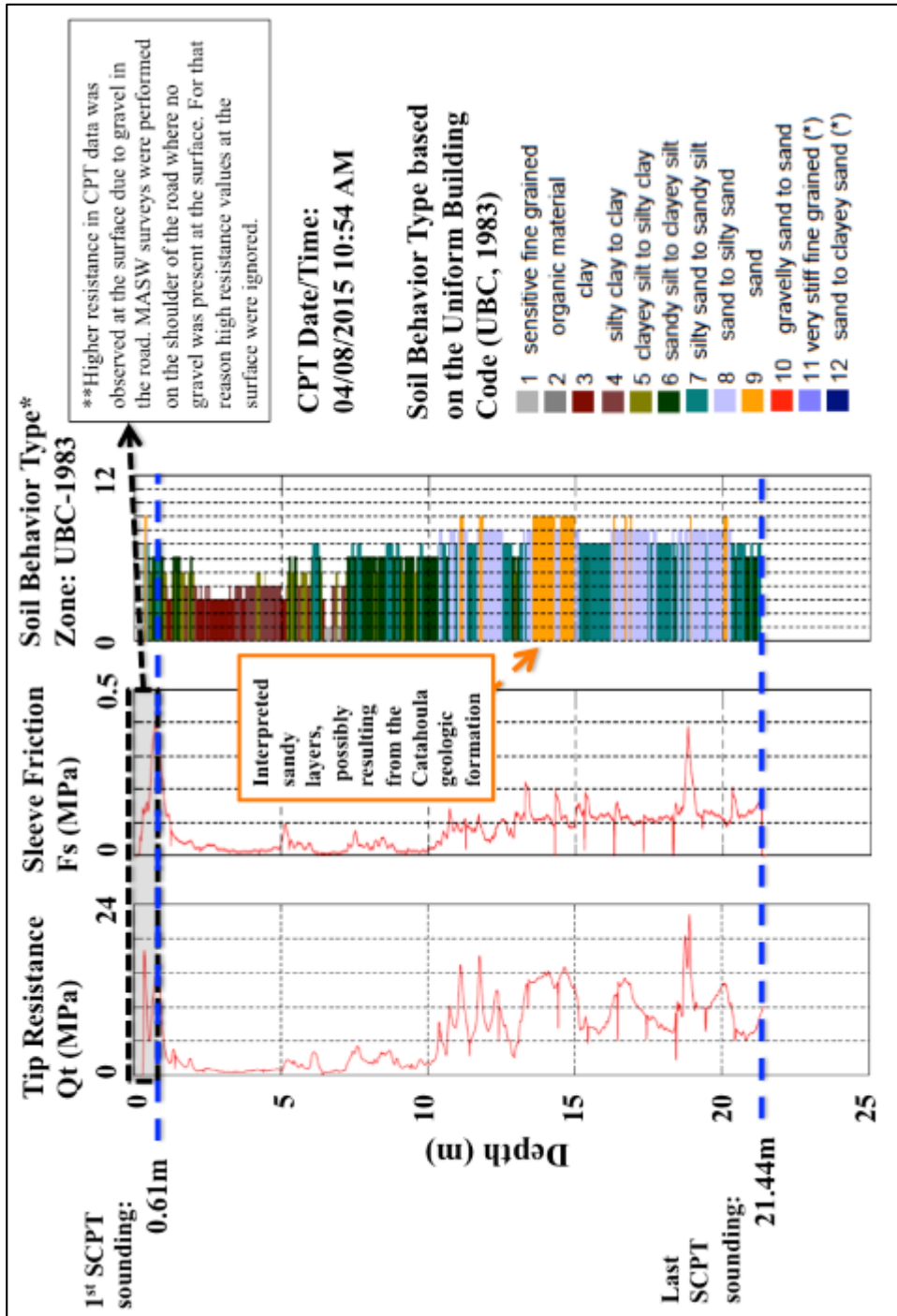
Figure B.1   CPT data obtained during the SCPT test.

164